Echoic Flow for Guidance and Control

Dissertation

Presented in Partial Fulfillment of the Requirements for the Degree Doctor of Philosophy in the Graduate School of The Ohio State University

By

Saif Abdulmohsen S Alsaif

Graduate Program in Electrical and Computer Engineering

The Ohio State University

2019

Dissertation Committee

Dr. Graeme E. Smith, Advisor

Dr. Fernando Teixeira

Dr. Keith Redmill

Abstract

Flow fields naturally measure the time to contact (TTC) between two objects, and are symbolized by the parameter tau. Hence, the term echoic flow (EF) represents the use of flow fields in active sensing systems, like radar and sonar. In this research, I present a key demonstration using echoic flow to guide a robotic vehicle autonomously around an unfamiliar path. Will briefly introduce the main concepts that explains echoic flow and describe how echoic flow can be used as a bio inspired guidance system. Several experiments with a robotic vehicle shown capable of traversing a square corridor with one of the sides containing a series of obstacles.

Echoic flow aided radar will also be shown capable of enabling a robotic vehicle to successfully traverse apertures. The bio inspired radar proposed relies on a perception-action cycle in which echoic flow is the perception, and steering instructions are the actions. A series of experiments using a robotic vehicle equipped with acoustic radar are presented to show that the echoic flow aided radar system is capable of traversing apertures in numerous situations.

Conventional methods for target following and approach involve complicated computing and re-computing of target position with respect to radar and lead to excessive processing. However, echoic flow based radar has been shown capable of achieving guidance and navigation with simple processing in both simulated and experimental

studies. In the presented research, the use of the derivate of the echoic flow parameter “tau-dot” in bio inspired radar for target following and approach control applications will be examined. After a brief introduction of the echoic flow derivative, three target movement scenarios are presented: stationary target; target moving slower than radar platform and target moving faster than radar platform are analyzed using both simulations and experiments. In all scenarios, the radar platform was able to close both range and velocity gaps with respect to the target successfully at the same time, regardless of the small variation in range and velocity measurements. Also, the effect of range and range rate measurement accuracy on echoic flow is discussed and methods to achieve suitable levels of accuracy presented.

Finally, the path traveled by the echoic flow aided acoustic radar testbed when moving in a straight corridor with multiple environmental sets were shown to trail the paths of an echolocating bat. Which largely indicates the connection between echoic flow as a guidance approach and the use of echolocation in bats.

Dedication

I dedicate this dissertation to my amazing wife, May, who has offered constant support and encouragement during the years of my doctoral journey.

To my parents, Abdulmohsen and Nora, and siblings, for always believing in me.

To my uncle, Eissa, who motivated me into loving math and science from an early age.

To my friends …

Acknowledgments

I would like to acknowledge my two advisors: Chris Baker for giving me the chance to work at the Cognitive Sensing Lab, in the ElectroScience Lab; and Graeme Smith, for his expertise, understanding and, generous guidance.

Vita

2004 ……..…… King Saud Educational Complex High School

2009 ……..……. Bachelor of Science in Electrical Engineering,
King Saud University, Riyadh, Saudi Arabia

2012 …….. Master of Science in Electrical and Computer Engineering,
The Ohio State University, Columbus, Ohio

Publications

S. Alsaif, and G. E. Smith, "Echoic Flow Aided Radar for Robotic Guidance and Aperture Traversal", *Robotics and Autonomous Systems,* 2018. *In review.*

S. Alsaif, G. E. Smith, and C. J. Baker, "Echoic flow for Target Following and Approach", *CIE 2016 International Conference on Radar,* 2016.

S. Alsaif, G. E. Smith, and C. J. Baker, "Using Cognitive Radar to Traverse Apertures", *IEEE 2014 International Radar Conference,* pp. 1–6. 2014.

G. E. Smith, S. Alsaif, and C. J. Baker, "Echoic Flow for Cognitive Radar Guidance", in *Proceedings of the 2014 IEEE Radar Conference,* pp. 490 – 495. 2014.

Fields of Study

Major Field: Electrical and Computer Engineering

Studies in:

Radar Signal Processing

Robotics

Control Theory

Table of Contents

List of Tables

List of Figures

Chapter 1: Introduction

This dissertation explores the use of the biologically inspired theory of echoic flow as a guidance method in radar aided platforms. The development of the theory, along with practical applications of the guidance approach is investigated through simulation and experiment. In this chapter, an overview of key elements relating to this dissertation is presented in section 1.1. A summary of the research contributions is located in section 1.2, while a dissertation outline is in section 1.3.

1.1 Overview

Echolocating mammals such as, bats, whales and dolphins are able to observe their environment and build an experiential memory. They constantly change the transmitted signal by varying duration, intensity and frequency to get a sense of the neighboring environment. Bats for example sense the environment by transmitting an acoustic sound that echoes back to both ears, which provides a perceived acoustic picture of the surroundings. This picture enables bats to navigate through complex terrain, avoid collision, feed and socialize [10] and [11].

Related literature suggests that bats use flow fields as a means of measurement to navigate their environment [5] [6] and [7]. Flow was first modelled for optical sensing and showed how flow fields can provide information about relative self-motion from images

[20]. This approach is now called optical flow. Flow fields had not been used in active sensing systems such as radar and sonar until Smith and Baker introduced echoic flow [1] and [2] where simulations using echoic flow (EF) theory showed promising results in the field of guidance and navigation. They show that echoic flow is a natural output of a radar system, trivially simple to compute and has the potential to greatly simplify the problem of autonomous guidance by removing the need to perform complicated kinematic calculations i.e. the guidance function is best framed in terms of echoic flow rather than conventional kinematics.

Flow in general, and specifically echoic flow, deals mainly with applications that require the closing of an action gap, such as the gap between the radar platform and a target or an obstacle. For that, several applications can be performed using echoic flow such as, flight landing on a stationary or moving runway, ship docking, car following and braking, missile interception, etc.

It is also proposed that echoic flow is an inherently adaptive approach [3]. Where an EF aided radar operates using a perception-action cycle. During perception, the radar perceives the environment and extracts information from the received signal like, range, velocity and angle. After perception, the extracted information is compared to a memory which results in a proposed action. Hence, the importance of echoic flow for simplifying sensing comes from its relative nature. A radar generally measures range to an object. However, if that object is in motion, then range alone is not enough input to decide upon an action given that it is a dynamic object. However, echoic flow is an inherently dynamic sensing domain since it includes range and range rate, producing a function of time.

In order to address the validity of echoic flow on radar sensing applications, this research focused on the advancement of the EF theory to accommodate engineering applications and their limitation. Furthermore, the key effort of this research was an experimental validation of EF aided radar, with an emphasis on guidance and control applications.

Therefore, and for a more reliable echoic flow research with respect to radar, a full-scale acoustic radar system was built and developed to measure both range and velocity using two separate pulsed and continues wave schemes. The system was mounted on a robotic vehicle and has the capability of guiding autonomously.

1.2 Contributions

The following areas of research have been contributed to by the dissertation described here.

- A contribution to the radar theory was made by investigating the effect of low speed of propagation when using an acoustic wave in an FMCW radar, especially the effect of transmit and receive waveform overlap. In electromagnetics, the high speed of propagation results in neglecting the effect of overlap between the transmit and receive waveform, while the low speed of propagation of an acoustic wave require the study of the effect when using a sawtooth and Triangular FMCW. In this Dissertation, the effects of signal overlap between transmit and receive waveforms has been addressed for an acoustic wave, especially for range resolution and maximum detectable range.

- Given that acoustic signals have relatively low frequency compared to electromagnetics, the narrow band assumption was tested and shown that using acoustic FMCW with high fractional bandwidth yielded a wideband case. Therefore, the use of the narrow band assumption was dismissed in acoustic FMCW and the Doppler frequency error was calculated with respect to varying center frequency and modulation bandwidth.
- A development of the echoic flow equation with respect to using relative range and Doppler velocity measurements, and the introduction of the concept of gap closing vs gap opening that depends on velocity sign.
- The extended development of the theory of time derivative of the echoic flow, and the introduction of the case when radar platform has a lower speed compared to the target, which yields a gap opening. Also, introducing restrictions to the time derivative of the echoic flow equation to assure gap closer in both range and relative velocity.
- A novel equation for echoic flow precision measurement was developed from using range and Doppler velocity precision equations. The equation showed that the target's range and velocity have an effect on the precision of the echoic flow measurement. Also, a validation to the echoic flow precision equation was applied through simulation for an acoustic triangular FMCW radar, with results coinciding with theory developed.
- A full acoustic radar system that uses both LFM and FMCW waveforms was developed and mounted on a mobile robot. The design, integration,

programming and calibration was solely performed in the lab, and results using the system helped with achieving significant research outcome shown in chapter 6 for a single monostatic radar and chapter 7 and 8 using a dual monostatic radar.

- The use of the time derivative of the echoic flow parameter in simulation and experiment showed an ability to close both range and relative velocity gaps for stationary targets, targets with lower velocity than radar platform and targets with higher velocity than radar platform. The results correspond with developed theory and represent a novel approach when using echoic flow aided radar systems with target following and approach applications.
- Two key guidance experiments were performed when using echoic flow as a guidance method. The first approach was guiding the monostatic acoustic radar testbed thorough a series of square corridors while one side having chicanes. The proposed guidance approach was shown successful in autonomously guiding the platform. The second experimental set was using the same guidance method to guide the platform towards traversing apertures. Multiple environments were tested with success in traversing the aperture for each set.
- The validation of the connection between flying bats and the use of flow theory was performed when using an acoustic radar testbed both in simulation and experiment to study the path behavior when guiding through a straight corridor built with pole side walls. The simulation and experimental outputs agree with the behavior of an echolocating flying bat presented in literature.

1.3 Dissertation Outline

The first chapter in this dissertation provides an introduction to the research by explaining the history behind echoic flow and the validity of using it in active sensing systems. It also provides the contributions of the research and the dissertation outline.

Chapter 2 presents the existing literature behind the flow theory, which is often called tau theory and presents its well known outcome called optical flow. Early studies in Echoic flow, as an echolocation output of flow theory is also explored. Moreover, work applied to bio inspired unmanned aerial vehicles along with aperture traversing robots are presented. Finally, experiments done by studying the path flown by echolocating bats are examined.

In chapter 3, the basic radar theory is introduced with a focus on Frequency Modulated Continuous Wave (FMCW) radars using both sawtooth and triangular waveforms. Also, the use of an acoustic signal when transmitting an FMCW was studied and the effects on range resolution and maximum detectable range was emphasized. While the narrow band assumption when using acoustic vs electromagnetic signal in FMCW radars is also considered.

Chapter 4 introduces the echoic flow theory and shows the development of the theory when using relative range and Doppler shift for velocity measurement. The theory development of the derivative of echoic flow as a controlled braking and following approach was presented and theory constrains were introduced. Furthermore, the precision measurement of range and Doppler velocity in radar was used to develop a formula for the precision of the echoic flow parameter tau when measured using range and Doppler

velocity, and the constrains of using acoustic FMCW is takin into account to develop a special case of the echoic flow precision equation. The equation is tested through simulation and outputs are presented.

For chapter 5, the overall development of the acoustic radar experimental testbed was presented by explaining the robotic platform's specifications, the onboard acoustic radar integration and specifications, the acoustic radar frame, and the overall integration of the acoustic radar on top of the radar platform. Testing results of the acoustic radar in range, Doppler velocity, and the corresponding echoic flow output is also presented.

The use of the developed theory of the derivative of the echoic flow presented in section 4.1.3 is shown in chapter 6. Simulations of an acoustic radar aided robotic platform were shown approaching a stationary target and following a moving target. The same simulations were then tested using the experimental testbed and two robotic platforms to produce similar results.

Chapter 7 presents experimental results of the acoustic radar testbed using dual monostatic radars to guide through complex environments. The same system was then shown capable of navigating through apertures with different environment configurations. Both experimental setups were repeated by using the robotic platform's internal range finders and then the fully developed acoustic radar testbed.

In chapter 8, the dual monostatic acoustic radar testbed was also used to test the followed guidance path through a straight corridor built with evenly spaced pole walls. The paths were first tested through simulation, by having six different environment configurations, and then experimental validation were undertaken with the same six

environment sets. The path followed by the platform is discussed, and conclusions are drawn from simulation and experimental results.

Finally, chapter 9 highlights the conclusions of the dissertation and proposes future work that could be perused when benefiting from the research presented.

Chapter 2: Literature Review

This literature critique will first discuss the general flow theory and its connection to natural sensing systems that navigate through complex environments. It will then present important texts relating to the use of flow theory in active synthetic sensing systems, and hence, the term echoic flow. Other texts related to bio-inspired UAV's that are developed based on Tau theory will be studied. Also, texts related to robotic guidance and environments that require aperture traversing will be presented and reviewed. The guidance of an acoustic flying bat through experimentally manipulated environment will be addressed.

2.1 Flow Theory

Flow theory, often called tau theory, was developed to explain how humans and other mammals like bats, whales and dolphins use their sensory inputs to navigate their complex environments without the use of kinematic calculations. It was first introduced by Gibson [20] [21] and [22] as an optical concept of perception, and how the changing pattern of light at the eye provides knowledge for guiding movement. Then, Lee [5]-[9] developed a mathematical theory of perception and action in the natural world and called it Tau Theory.

Optical flow, which presents flow through a visual sensor, is an estimate of the relative distance to an object or obstacle when moving through a visual environment by inherently measuring the ratio of light intensity to variations in that intensity. Animals who rely on

vision to navigate in natural environments and avoid collision have been shown in research to use optical flow. Honeybees, for instance, use the pattern of image motion perceived through their visual system to navigate, and has been shown to hold constant the rate of change of image perception in the eye when moving through a tunnel [23] [24]. While optical flow provides continuous updates about relative velocity and distance to objects in the environment, experimentally changing the perception of the visual cues of the environment affects the flown trajectory of honeybees [25].

Up to the late 1980s, Lee [7] states that studies only showed tau theory as a visual guidance (Optical Flow). However, questioning if τ is used by all perceptual systems made him interested in echolocation, and later on led to the formulation of General Tau Theory. General Tau Theory, presented in [7], involves in all purposeful movements entails controlling the closer of an action gap. Where an action gap is the separation between the current state an animal is in and the goal state to be achieved by action.

Action gaps are shown to be in different dimensions [7] such as distance, angle, pitch, pressure, etc. Lee postulated that it would be useful if all action gaps were measured the same way. Therefore, he assumes that the only measure used by animals or humans when controlling the closure of an action gap of any kind is the time parameter tau. By converting all sensory measurable parameters to tau, the task of gap closure will be greatly simplified.

In [6], Lee demonstrates the significance of echoic flow for autonomous guidance and control activities. He represents his flow theory form [5] [6] and [7] by mostly focusing on the echolocating bat. An example in which a bat's landing trajectory satisfying the coupled flow concept. Hence, being consistent with Lee's earlier analysis. Additional

evidence for widespread use of flow theory is presented in [26] in which a similar regression approach is used to demonstrate flow theory can describe how humans undertake target interception during a computer based test. Due to the nature of biological research I cannot be certain that the animals are using flow theory, but the evidence does seem convincing.

Though controlling braking for the task of stopping at an obstacle seems to be a complex controlling procedure involving range, range rate and, acceleration, Lee [7] stated that he believes the only information a driver needs to control ongoing breaking is the time derivative of the flow parameter $\dot{\tau}$, which is set to constant during the braking process, resulting in gap closure. A study by Lee following the braking process of drivers stopping at a preassigned point [27] stated that on average they maintained a constant $\dot{\tau} = 0.42$. While, for $\dot{\tau} < 0.5$ a controlled collision [5] can be achieved with an example for the distance gap between an echolocating bat and a narrow aperture to be flown through, a mean of $\dot{\tau} = 0.75$ was recorded.

Lee has introduced the General Tau Theory, and showed that all perceptual movements by humans, birds, bats and other mammals are governed by the flow parameter. However, he only observed the natural world, and did not test his theory on any synthetic system. This is due to his interest in describing how existing, natural systems work, and that he is not concerned with investigating how flow theory might be used in engineering to help with autonomous applications.

2.2 Echoic Flow

Echoic flow is a radar concept defined by Smith and Baker [1] and [2] to be the ratio of a sensor measurable parameter to a change in that parameter over a unit of time. They applied flow fields to radar and sonar calling it echoic flow since these sensors use echolocation. Echoic flow will give a direct measurement of the time for a radar system and an object to collide with each other, satisfying the flow theory term "time to close an action gap".

To demonstrate the potential of echoic flow for control braking, autonomous guidance and collision avoidance, two simulations were developed [2]. The first simulation focuses on the use of the time derivative of echoic flow $\dot{\tau}$ to control braking, where a radar platform is moving horizontally towards an object. For zero velocity at the object, $\dot{\tau} = 0.5$ was maintained. It is clear that the radar platform stopped at the object with it slowing steadily until reaching zero velocity, with the result of this simulation agreeing with flow theory. However, this simulation only examined one $\dot{\tau}$ constant and did not show the effect of changing $\dot{\tau}$ on braking strategy through simulation. Also, no real experimentation work has been performed to validate simulation results.

The second simulation set demonstrated the concept of autonomous guidance by simulating a platform equipped with two monostatic radars having $\pm 45^{o}$ beam angles with respect to the direction of travel. The two beams calculate the echoic flow in each direction and turns away from the smallest echoic flow, or time to collision. Regardless of the simplicity of the rule, the platform succeeded in guiding through narrow corridors with corners and obstacles.

Furthermore, a range case was presented in [3] for a radar platform traveling with a velocity of 1 m/s, 10 meters away from a target to demonstrate the effect of changing the derivative of the echoic flow on the braking behavior, and categorize it as early, late and constant braking strategies, along with accelerating towards the target. However, Smith and Baker [3] argue that the real power of using $\dot{\tau}$ to control braking is evident when the object is in movement rather than stationary. Thus, for a moving object, the range rate measured by the radar will be the relative range rate, which will result in tau estimates and equations of motion that automatically compensate for the object motion.

Finally, Echoic flow was defined and tested. Then shown how it can be applied in bio inspired radar sensing. Also, several simulation work of echoic flow for autonomous guidance and controlled braking was presented in [1] [2] [3] and [4]. However, verification of such techniques is required through experimental work.

2.3 Bio-Inspired UAV's

Two papers, [28] and [29] are based on the ecological tau theory developed by the psychologist David Lee [5] [6] and [7] to help guiding some essential capabilities of Unmanned Aerial Vehicles (UAV's). A primary capability of UAV's is perceiving surfaces or objects in the environment and then guiding their movement for successful contact with these surfaces such as docking and landing, or to avoid contact as obstacle avoidance.

The first paper [28] introduced a new term called "TauPilot". The TauPilot system uses the flow theory in developing a guidance, navigation and control system (GN&C) that has

the capability to move in a 3D environment using only τ as a measurement. TauPilot has been used in two UAV's and tested in more than a thousand successful trials.

Kendoul and Ahmed [28] claim that they have not found a single paper or work on the application of tau theory for the guidance and navigation of UAV's. They also indicate that despite the substantial number of research papers discussing tau theory, none of them have applied tau theory for robot's guidance and navigation. Therefore, they show their work as the first paper that uses tau theory of Time to Contact (TTC) for the guidance and control of UAV's. During the course of this literature search, I have not found any contradiction to their claim. However, compared to conventional guidance and control, TauPilot has some limitations with maneuvers that does not require closing of a gap, such as hovering and long distance flying.

The second paper [29] presents a path planning method for UAV perching, that is based also on tau theory. They have studied two scenarios, one from a flight state and the other from a hovering state. Three strategies are demonstrated for every scenario, the tau in action gap strategy, the tau coupling strategy, and the intrinsic tau gravity strategy. A Quadrotor UAV with perching capability was used for simulation. The simulation results show potential success for a rotary UAV to perch on an object. Similarly, [30] applied tau theory for trajectory generation of multiple UAVs. Finally, the braking and landing of a UAV was achieved using a camera with its output processed using the derivative of tau [31]. However, flow theory has yet to be applied in situations where the target being approached is in motion.

2.4 Aperture Traversing Robots

It may seem that traversing an aperture, is a trivial problem. However, the literature demonstrates achieving a high success rate with computationally simple routines is challenging. Additionally, when facing scenarios where darkness, smoke and dust in the environment are present, will limit the capability of sensors such as optical cameras and lidars.

In general, indoor autonomous guidance is an application of high interest. It has been examined using GPS solutions [32], but GPS signals can be highly unreliable in indoor environments and GPS can only deal with obstacles of already known position. RFIDs and wireless networks have also been used for indoor localization [33], [34]. Not only do these techniques require an existing infrastructure but they also suffer from the problem of not detecting potential obstacles. Laser and passive optical techniques [35], [36] have been used with success for collision avoidance, accurately mapping their local environment. However, they still require good visibility.

Previous attempts to solve the problem of traversing an aperture have relied on deterministic methods. In [37] a generalized control rule is proposed that has unknown constants. Training data is gathered by manually driving the robot platform through an aperture while collecting data with its 180 degree lidar and sonars. The collected data is then used to determine the constants for the control rule. Later experiments have successful performance. However, the independence of the control rule constants from the environment is never proven.

Furthermore, [38] and [39] focus on robots that navigate to find the largest gap in the local environment and then navigate through it. These approaches relay also on deterministic control. While this does not affect the performance, it will be expected to limit the processing flexibility to different platforms and changes of environment.

Additionally, [40] presents a simulated robot equipped with a 3-D scanning lidar that generates a range image of the environment. The image is processed through a recognition system based on support vector machines (SVMs) that identifies possible apertures to be traversed. The robot performance is successful; however, training is required and the use of SVMs involves substantial processing.

2.5 Guidance of Flying Bats

The BatLab at the John Hopkins University [41], is a lab that investigates the mechanism of spatial perception, especially by bats, to navigate in natural environments. The study of the bat's active sensing system as a guidance machine and the actions performed are exploited.

Using the BatLab, a work related to evaluating a bat's flight and echolocation behavior was performed. An experimental setup derived by using the sound emission of echolocating bats flying though a straight corridor, whose walls are built from individually movable poles, to create different flow patterns. And then evaluate the bats deviation in flight path to understand how flow patterns influence the bat's flight and echolocation behavior [42]. The bat that is used in the experiment is a big brown bat called, *Eptesicus Fuscus*, with a flying speed between 2 to 6 m/s [43], and emits a frequency modulated

waveform between 25 kHz and 65 kHz [44]. The bat can vary its call rate, duration of call and, bandwidth to adapt to cluttered environment [45]. Hence, suggests that the big brown bat adjust its velocity and transmit parameters when moving in dense and sparse wall environment.

Consequently, the environment in [42] was set to test two different scenarios. When the pole spacing in the two side walls of the corridor having the same layout, and when they are imbalanced in spatial structure. The output of the experiment yielded that the bat was flying through the centerline of the corridor when both sides of the corridor had the same spacing between poles, while shifting towards the sparse side when the corridor walls are different in pole spacing. However, it is not clear whether the bat is simply doing a calculation of collision avoidance, or it is a more complex perception and processing of the environment. Furthermore, the test was performed in only two stages, and the effect of the amount of deviation from the centerline with respect to the gap size between poles is not tested.

Chapter 3: Radar Theory

This chapter introduces basic radar theory required to understand the use of radar systems in measuring echoic flow. A focus on the Frequency Modulated Continuous Wave radars (FMCW) will be presented due to the use of such system in the simulations and experiments conducted throughout this dissertation.

Furthermore, a detailed explanation of the effects of using an acoustic FMCW radar on both range resolution and maximum detectable range will be presented and simulated. While using the fractional bandwidth to determine the difference in using electromagnetic vs acoustic FMCW radar to determine a wideband and a narrowband effect on the radar system is also presented.

Except when cited otherwise, this section is summarized from *Introduction to Airborne Radar* [12], *Principles of Modern Radar: Basic Principles* [13], and *Principles of Modern Radar: Radar Applications* [59].

3.1 Radar Basics

Radars (**Ra**dio **D**etection **A**nd **R**anging), are range measuring devices, that can detect targets day or night and through all weather conditions. It uses a simple concept of echo-ranging, where range estimation can be performed by measuring the transit time of the

signal's round trip; which is the time the radio waves takes to reach the target and then return as shown in Fig 3.1.

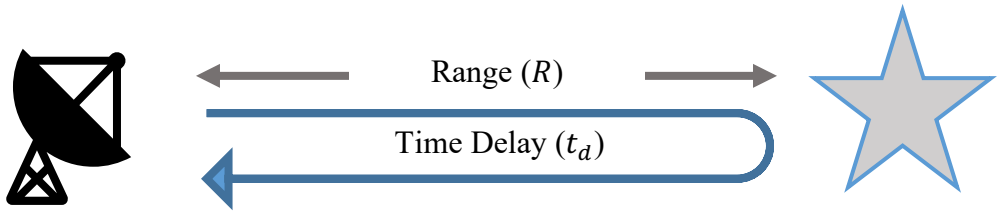

Fig. 3.1: Illustration of the time required to calculate range to a target.

Given that (c) is the speed of propagation, then the range to the target is a function of both signal time delay and speed of propagation:

$$R = \frac{c\ t_d}{2} \tag{3.1}$$

For a pulsed waveform, the maximum unambiguous range is the maximum range that a target can be located at, and guarantee that the received backscatter from that target is received before transmitting the next pulse. It is a function of pulse repetition frequency (PRF), which is inversely proportional to the pulse repetition interval (PRI), that consists of both the pulse width and the time the receiver is listening to the returned signal. The maximum unambiguous range can be calculated using PRF, and is given by

$$R_{max} = \frac{c}{2\ PRF} \tag{3.2}$$

Therefore, the unambiguous range, or in other words, the maximum detectable range for a pulsed waveform is only possible when the round trip time delay t_d is shorter that the PRI.

The other factor concerning maximum detectable range is the signal to noise ratio (SNR). The signal to noise ratio (SNR) is the ratio between the received power and the receivers noise power. Radar detection performance is a function of the strength of the signal reflected from the target, compared to strength of the signals interfering with the target's signal. The Radar Range Equation is the equation that provides expected signal to noise ratio. And from that, a maximum detection range is defined. The received power equation, the receiver noise power and the radar equation are shown in (3.3), (3.4), and (3.5) respectively.

$$P_r = \frac{P_t G_t G_r \lambda^2 \sigma}{(4\pi)^3 \, R^4} \tag{3.3}$$

where P_t is the average value of the transmitted power, G_t and G_r are the transmit and receive antenna gain respectively, λ is the signal wavelength, and σ is the Radar Cross Section (RCS) of the target. R is the range between the target and the radar

$$P_n = kT_0BF \tag{3.4}$$

the receiver's noise power P_n equation in (3.4) has k as Boltzmann's constant, T_0 as the noise reference temperature, 290 k, B the receiver bandwidth and F as the receiver noise figure. Therefore, from (3.3) and (3.4) we get the radar equation as shown in (3.5).

$$SNR = \frac{P_r}{P_n} = \frac{P_t G_t G_r \lambda^2 \sigma L}{(4\pi)^3 \, R^4 \, kT_0 BF} \tag{3.5}$$

where L is a factor that includes the effect of losses such as, atmospheric attenuation, and signal processing losses. The factor L is less than or equal to 1.

The radar equation can be written to determine the maximum detection range for a given target. This is done by providing the minimum signal to noise ratio S/N_{min} as presented in (3.6).

$$R_{max} = \left[\frac{P_t G_t G_r \lambda^2 \sigma L}{(4\pi)^3 \, kT_0 BF \; S/N_{min}}\right]^{\frac{1}{4}} \tag{3.6}$$

The ability to distinguish several targets when more than one target is present is crucial to a radar system. The smallest distance between two targets at which they can be distinguishable as separate targets is called range resolution. The range resolution is calculated by evaluating the minimum separation in time between the returning echoes of the two close targets. The echo returning from the first target must be fully received before the echo returning from the second target is received. For a linearly modulated pulsed radar range resolution is calculated by

$$\Delta R = \frac{c}{2 \, B} \tag{3.7}$$

where *B* is the signal bandwidth, and c is the speed of propagation. Hence, a large signal bandwidth corresponds to a finer range resolution.

For a coherent radar, the ability of extracting information about a target's motion is possible. This is due to the target adding a Doppler shift on the reflected signal. The general term of radar Doppler shift for a point target moving with velocity V is given by

$$f_d = \frac{2Vf_0}{c} \tag{3.8}$$

where f_0 is the center frequency of the transmitted wave, and c is the speed of propagation.

3.2 FMCW Radar Theory

Frequency modulated continuous wave (FMCW) radars continuously transmit a signal that is modulated in frequency while simultaneously receiving the time delayed echo. FMCW radars consists of a transmitter, receiver and a mixer. The frequency modulated transmitted signal is then multiplied in time domain with the received echoe signal, and processed to determine range and Doppler.

In general, FMCW radars use a linearly frequency modulated waveform (LFM), which commonly referred to as a chirp function. Fig. 3.2, shows the LFM sawtooth transmitted and received waveforms of an FMCW radar. The difference between the start and the stop frequency is called modulation bandwidth ΔF, which is the same as the signal bandwidth B in pulsed radars. The time between two modulations is called the modulation period and denoted by T_m.

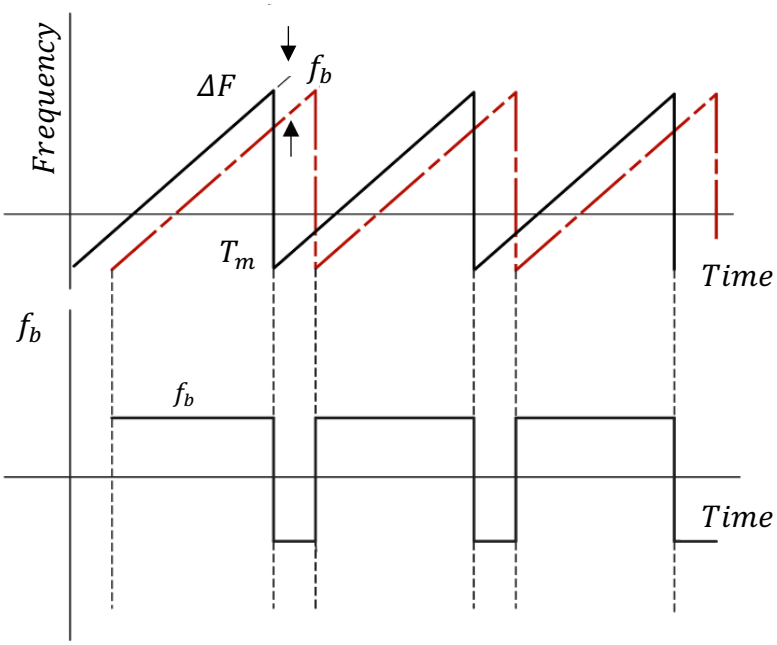

Fig. 3.2: transmitted and received sawtooth FMCW with beat frequency.

The red dotted sawtooth in Fig. 3.2 is the received signal. The received signal is shifted in time by the two way propagation delay that is proportional to the distance to the illuminated object, $t_d = {2R}/{c}$, where R is the object's range, and c is the speed of propagation, see Fig. 3.1 and (3.1). The beat frequency, obtained at the output of the mixer, is the instantaneous difference in frequency between the transmitted and received signals. From the slope of the LFM sawtooth, a relationship between the modulation bandwidth, the modulation period and the two way time delay with beat frequency can be shown in (3.9), where f_b is the beat frequency.

$$\frac{f_b}{\Delta F} = \frac{t_d}{T_m} \tag{3.9}$$

By substituting the equation of two way propagation delay t_d into (3.9), we obtain

$$f_b = \frac{\Delta F}{T_m}\frac{2R}{c} \tag{3.10}$$

Equation (3.10) shows the relationship between the beat frequency and the range to an illuminated object by the FMCW radar. By rearranging (3.10), an estimate of the beat frequency can be converted to an estimate of the target range in (3.11).

$$R = \frac{T_m\, c\, f_b}{2\, \Delta F} \tag{3.11}$$

Furthermore, when mixing the transmitted and received signal, the beat frequency will consist of two components, the positive and negative components as shown in Fig. 3.2. Given that the time delay to the object is relatively small compared to the modulation period, the negative component will have very short duration and can be ignored. However, for longer target delays, the negative beat frequency could be eliminated by only mixing the overlapping part of the transmit and received waveforms. A detailed explanation of the overlap between the transmit and received waveforms is presented in section 3.3.1 and 3.3.2.

For the case where the object is moving, the beat frequency will be affected by the Doppler shift of the object's velocity. When target is in motion, an ambiguity between range and Doppler is present in the beat frequency that is called, Range-Doppler coupling. Which causes a shift in the beat frequency that is relative to the radial velocity of the target.

To resolve both range and Doppler at the same time for a moving target, a triangular LFM is used as shown in Fig. 3.3.

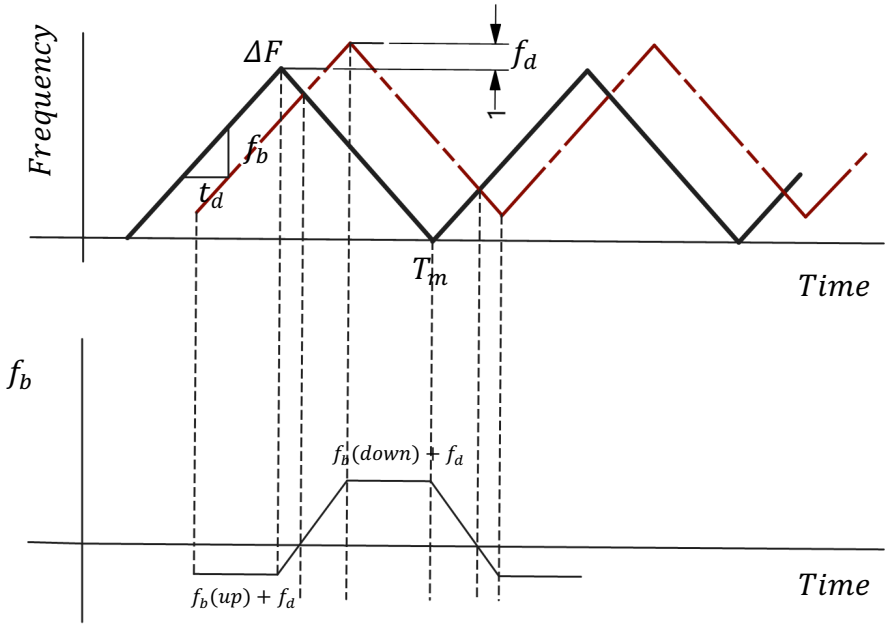

Fig. 3.3: Transmitted and received Triangular FMCW with beat and Doppler frequency.

From Fig. 3.3, when mixing the transmitted and received triangular waveforms, two beat frequencies are present due to the up sweep and down sweep. To get range to the object, the up and down sweep difference will result in the range measurement as shown in the equations below

$$f_b^{\uparrow} = -\frac{\Delta F}{T_m}\frac{4R}{c} + \frac{2Vf_0}{c} \tag{3.12}$$

$$f_b^{\downarrow} = \frac{\Delta F}{T_m}\frac{4R}{c} + \frac{2Vf_0}{c} \tag{3.13}$$

by subtracting and rearranging (3.12) and (3.13) to get range R

$$R = \frac{T_m c}{8\Delta F}\left(f_b^{\downarrow} - f_b^{\uparrow}\right) \tag{3.14}$$

while to extract velocity measurement from the up and down sweep, both beat frequencies will be added as shown in (3.15)

$$V = -\frac{c}{4f_0}\left(f_b^{\downarrow} + f_b^{\uparrow}\right) \tag{3.15}$$

by measuring both up and down beat frequency of the triangular sweep, range and velocity of a moving object is determined.

3.3 Acoustic FMCW Radar

When using an acoustic FMCW radar compared to an electromagnetic FMCW radar, several issues related to range resolution and maximum detectable range will be more persistent. In this section, a detailed explanation of the differences between acoustic vs electromagnetic FMCW radars in regard to two key outputs, range resolution and maximum detectable range are discussed. The effect of the percentage overlap between the transmit and receive waveform in both acoustic and electromagnetic FMCW is presented.

3.3.1 Range Resolution of Acoustic FMCW Radar

Since the speed of sound is 6 orders of magnitude lower than the speed of light, the range resolution ΔR of an acoustic radar system will be significantly different between electromagnetic and acoustic cases. FMCW radars in general can generate very high range resolution which allows fine range accuracy measurements, given that the range resolution of a linearly modulated radar system is inversely proportional to the modulation bandwidth ΔF.

$$\Delta R = \frac{c}{2\Delta F} \tag{3.16}$$

Where ΔR is the FMCW radar range resolution, c is the speed of propagation and ΔF is the bandwidth of the transmitted waveform. When transmitting an electromagnetic FMCW, the speed of propagation is the speed of light equaling to $3 \times 10^8\, m/s$, and therefore, to achieve a 1m range resolution, the modulated bandwidth of the transmitted signal should be 150 MHz.

However, when transmitting an Acoustic FMCW, the speed of propagation will be equal to the speed of sound approximately 340 m/s. This will result in achieving the same 1m range resolution with only 170 Hz of bandwidth. Fig. 3.4 shows range resolution vs modulated bandwidth when using FMCW for both electromagnetic and acoustic waveforms.

From Fig. 3.4, using an acoustic FMCW shifts the bandwidth curve to achieve the same range resolution as an electromagnetic signal by a multiple of 10^{-6}. In other words, reducing the bandwidth of an acoustic FMCW wave by a multiple of the power of 6 will result in the same range resolution. Therefore, from Fig. 3.4, a ΔR in the millimeter range is achieved using a kHz acoustic bandwidth compared to the GHz bandwidth of an electromagnetic signal.

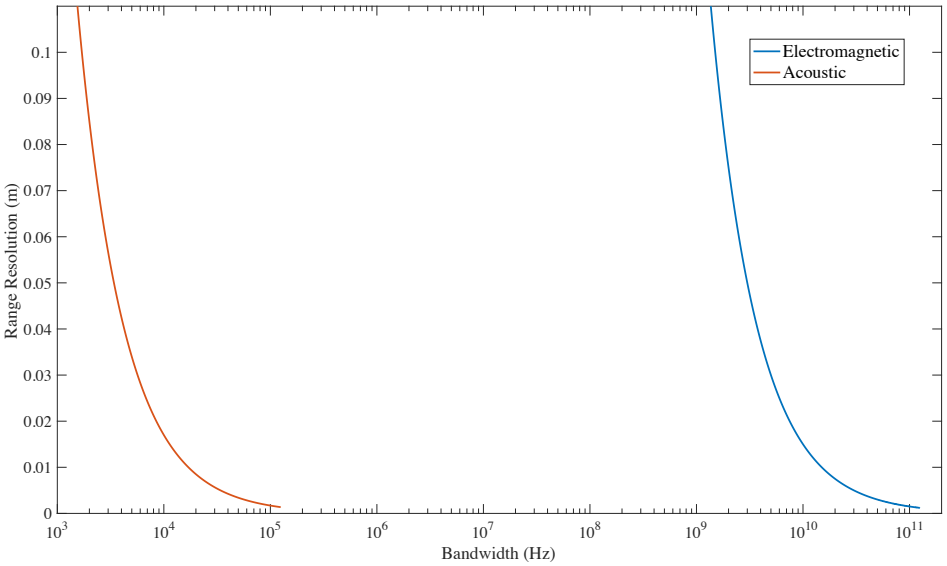

Fig. 3.4: Fine Range resolution for higher FMCW modulated bandwidth.

In FMCW radars, range measurement is a function of beat frequency as shown in (3.11) and (3.14). Therefore, to accurately measure range, an accurate estimation of the beat frequency is required. For this section, two acoustic FMCW radar simulations were developed, sawtooth and triangular FMCW. For the acoustic sawtooth FMCW simulation, the radar transmits a linear FMCW waveform with a 0.1s modulation period. The

bandwidth of the transmit waveform is set to 25 kHz covering the band of (25-50 kHz), with a center frequency of 37.5 kHz.

For such radar parameters, the maximum detectable range and the ideal range resolution are as follows

$$R_{max} = \frac{c}{2f_m} = \frac{340}{2 \times 10} = 17\ m$$

$$\Delta R = \frac{c}{2\Delta F} = \frac{340}{(2 \times 25 \times 10^3)} = 6.8\ mm$$

For a single stationary point target at 1 m away from the radar, the beat frequency is equal to

$$f_b = \frac{2R\ \Delta F}{c\ T_m} = \frac{2 \times 1 \times 25 \times 10^3}{340 \times 0.1} = 1.470\ KHz$$

whereas the equivalent beat frequency of the range resolution can be calculated by using the range resolution ΔR rather than range R when applying (3.10) as shown

$$f_b = \frac{2\Delta R\ \Delta F}{c\ T_m} = \frac{2 \times 0.0068 \times 25 \times 10^3}{340 \times 0.1} = 10\ Hz$$

Fig. 3.5 shows the beat frequency spectrum for a 1 m target. The spectrum spreads from 1.4 kHz to 1.54 kHz. This covers the range profile between (0.95-1.05 m). From Fig. 3.5 the stationary target echo at 1 m results in a beat frequency of 1.47 kHz. The first sidelobes are at approximately -13.3 dB lower than the mainlobe. Furthermore, when measuring the -3.9 dB width of the mainlobe to determine the corresponding range resolution of the FMCW radar from Fig. 3.5, it shows that it is equal to 11 Hz, which is 1 Hz higher than

the Ideal range resolution calculated. The difference is due to the decrease in overlap between the transmitted and received waveforms, which will be discussed in greater detail below.

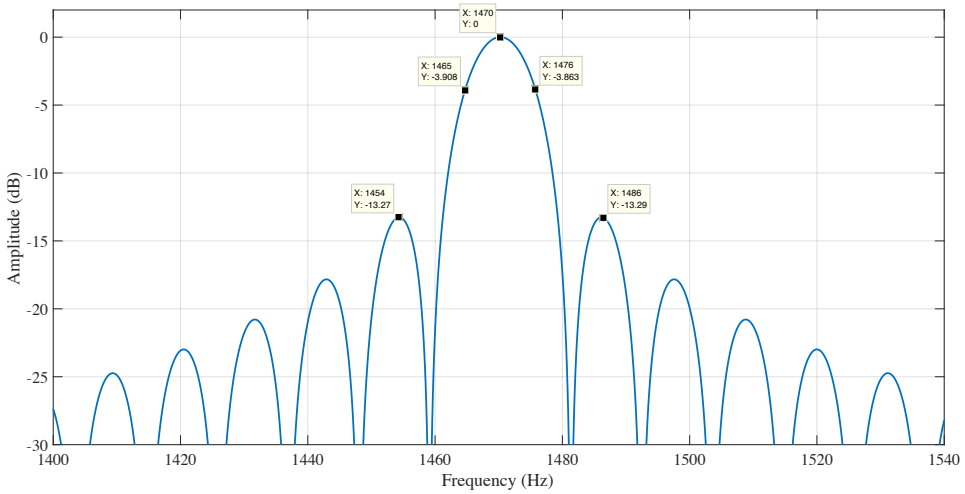

Fig. 3.5: Beat frequency spectrum for a 1 m target.

When using FMCW to detect targets at different ranges, the overlap between the transmit and receive waveforms varies based on the targets range location, this is due to the round trip propagation time delay t_d. For close range targets, the overlap in time between the two waveforms is large, that results in a low frequency separation, which is called the beat frequency. Whereas, for far range targets, the overlap between the transmit and receive waveforms is smaller compared to close range targets and causes a high beat frequency. Also, a partial overlap between the transmit and the received waveforms in the case of far range causes a wider bandwidth of the beat frequency's mainlobe, see Fig. 3.6.

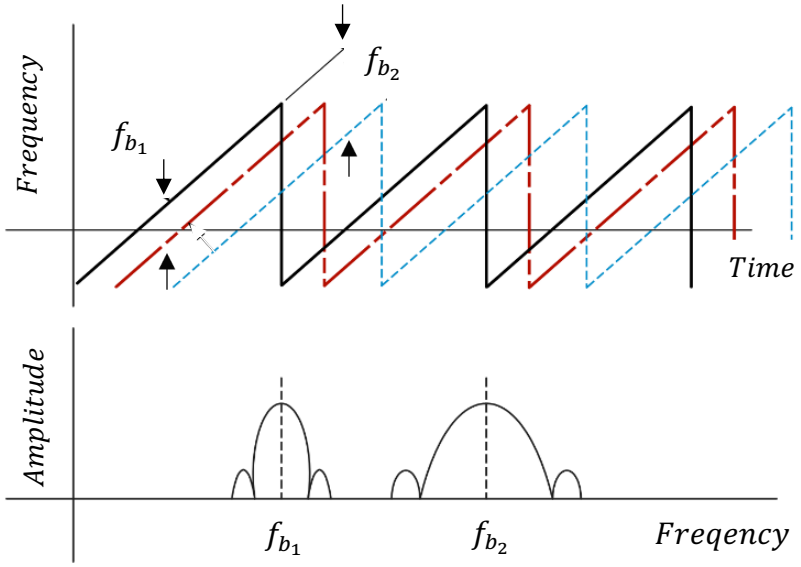

Fig. 3.6: Near and far range target's beat frequency spectrum.

The bandwidth of the beat frequency, and hence, the range resolution is a function of both modulation period and propagation time delay as shown in (3.17).

$$B_b(sawtooth) = \frac{1}{T_m - t_d} \tag{3.17}$$

By calculating the round trip time delay from (3.1) for the 1 m target, and substituting the output into (3.17), the bandwidth of the beat frequency is equal to $B_b = 10.62 \approx 11$ Hz. That matches the -3.9 dB width of the mainlobe in Fig. 3.5.

However, when the target is moved away and located in the far range at 15 m (note $R_{max} = 17\ m$), the bandwidth of the beat frequency's mainlobe becomes much wider as shown in Fig. 3.7.

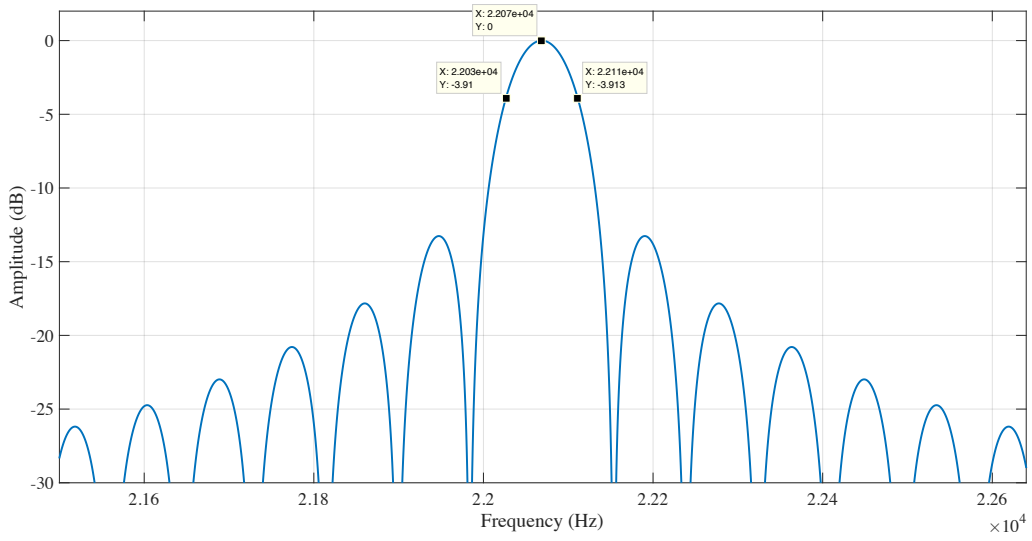

Fig. 3.7: Beat frequency spectrum for a 15 m target.

By measuring the beat frequency's mainlobe bandwidth, an increase in the -3.9 dB bandwidth from the ideal 10 Hz to 85 Hz. Here, the target's range resolution broadens by more than eight times the ideal range resolution. This is due to the change in overlap of the transmit and receive waveform from %94 when the target is at 1 m, to only %12 for the 15 m range target. The 85 Hz beat frequency bandwidth corresponds to a range resolution $\Delta R = 57.8\, mm$ compared to the ideal case of 6.8 mm.

3.3.2 Maximum Detectable Range of Acoustic FMCW Radar

When using an acoustic FMCW signal, the speed of sound will also affect the maximum unambiguous range, due to the longer time it takes for the transmitted signal to echo back from an object to the radar. The time delay between the transmitted and received

echo signal is proportional to the distance to that object, and is shown in (3.1), where t_d is the round trip propagation time delay, $2R$ is the two way range from the radar to the object and c is the speed of sound. Given that the relationship between the time delay and the range to an object is proportional, a limit to the maximum detectable range is governed by the signal's modulation period T_m.

For a FMCW radar, the modulation period is the inverse to the modulation frequency f_m, and equals to

$$T_m = \frac{1}{f_m} \tag{3.18}$$

the round trip time delay t_d cannot exceed the modulation period T_m for the signal to avoid ambiguous ranges, and half the modulation period for the triangular FMCW case, since the modulation period consists of up and down frequency slopes.

$$t_d < \begin{cases} T_m & For\ Sawtooth\ Waveform \\ \dfrac{T_m}{2} & For\ Triangular\ Waveform \end{cases} \tag{3.19}$$

Substituting equation (3.18) and (3.19) into equation (3.20) results in the maximum range detected by a FMCW radar for both sawtooth and triangular waves with respect to modulation time shown in equation (3.20)

$$R_{max} = \begin{cases} \dfrac{T_m c}{2} = \dfrac{c}{2f_m} & For\ Sawtooth\ Waveform \\ \dfrac{T_m c}{4} = \dfrac{c}{4f_m} & For\ Triangular\ Waveform \end{cases} \tag{3.20}$$

Form (3.20) the relationship between the maximum detectable range and the modulation frequency is inversely proportional, and therefore, the modulation frequency should be set based on the maximum range required for the radar.

However, since R_{max} is a function of propagation velocity, then transmitting an acoustic wave will be more limited in setting the maximum modulation frequency. For example, to detect a target that is 10 m away from the radar, when transmitting an electromagnetic FMCW, the modulation frequency could be set up to 15 MHz for a sawtooth wave and 7.5 MHz when transmitting a triangular wave. Whereas, detecting the same target at 10 m in range using an acoustic FMCW will require maximum modulation frequency of 17 Hz for sawtooth wave, and 8.5 Hz for a triangular wave. The difference between electromagnetic and acoustic FMCW with respect to maximum range and modulation frequency is shown in Fig. 3.8.

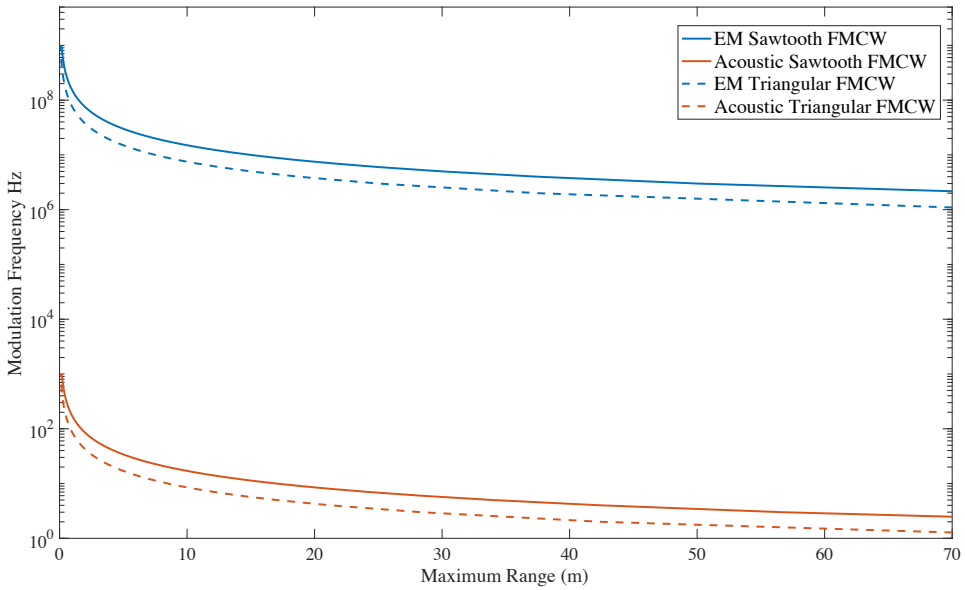

Fig. 3.8: Maximum detectable range vs maximum modulation frequency for Sawtooth and Triangular FMCW.

Fig. 3.8 indicates that using an acoustic FMCW will reduce the maximum detectable range when increasing the modulation frequency. Therefore, for applications that require detection of far range targets, an electromagnetic FMCW is required due to the high propagation velocity. Furthermore, when using a triangular FMCW, the maximum detectable range is divided by two when setting the same modulation frequency for both electromagnetics and acoustics.

In the other hand, the overlap between the transmit and receive waveform has an effect on the maximum detectable range. When using an electromagnetic FMCW, the maximum detectable range will be much higher than an acoustic FMCW. For example, for a modulation frequency of 1KHz, the maximum detectable range will be

$$R_{max} = \frac{c}{2f_m} = \frac{3 \times 10^8}{2 \times 1 \times 10^3} = 150\ Km$$

by only taking a minimum %90 overlap between the transmitter and the receiver, the maximum detectable range will be reduced to 15 Km, and the beat frequency bandwidth, of the range resolution, will broaden by only %11 as shown below

The beat frequency bandwidth with no delay:

$$B_b = \frac{1}{T_m - 0} = \frac{1}{T_m}$$

The beat frequency bandwidth with %10 delay:

$$B_b = \frac{1}{T_m - 0.1 \times T_m} = \frac{1}{0.9 \times T_m}$$

The beat percentage of broadening in beat frequency bandwidth with %10 delay or %90 overlap:

$$\left(\left(\frac{1}{0.9 \times T_m} - \frac{1}{T_m}\right) \Big/ \frac{1}{T_m}\right) * 100 = \%11$$

It is apparent that when using acoustic FMCW compared to electromagnetic FMCW, the maximum detectable range will be significantly decreased, and the far range target detection will also be affected due to decreased range resolution, and hence range measurement accuracy.

Since the modulation period of the triangular waveform consists of an up and down sweep, the maximum detectable range is divided in half (3.20), where the maximum round trip propagation time delay is half compared to the sawtooth waveform. This will increase the percentage of the broadening of the target's beat frequency bandwidth (3.21).

$$B_b(triangle) = \frac{1}{\frac{T_m}{2} - t_d} \tag{3.21}$$

For the case where the target is located 1 m away from the acoustic FMCW radar, the calculated bandwidth of the beat frequency is equal to $B_b(triangle) = 22.66 \approx 23$ Hz. Since the beat frequency of a triangular FMCW is twice that of a sawtooth FMCW (3.14), $B_b(triangle\ to\ sawtooth) \approx 23/2 = 12$ Hz, shows an increase in the target's beat frequency bandwidth by 2 Hz, that is twice the increase in the $B_b(sawtooth) = 11$ Hz case. In short, the broadening of the triangular FMCW beat frequency bandwidth will

double for the case of partial overlap between the transmit and receive waveforms compared to sawtooth FMCW. Fig. 3.9 shows the beat frequency spectrum from -4 KHz to 4 KHz of the 1 m stationary point target when transmitting a triangular FMCW waveform.

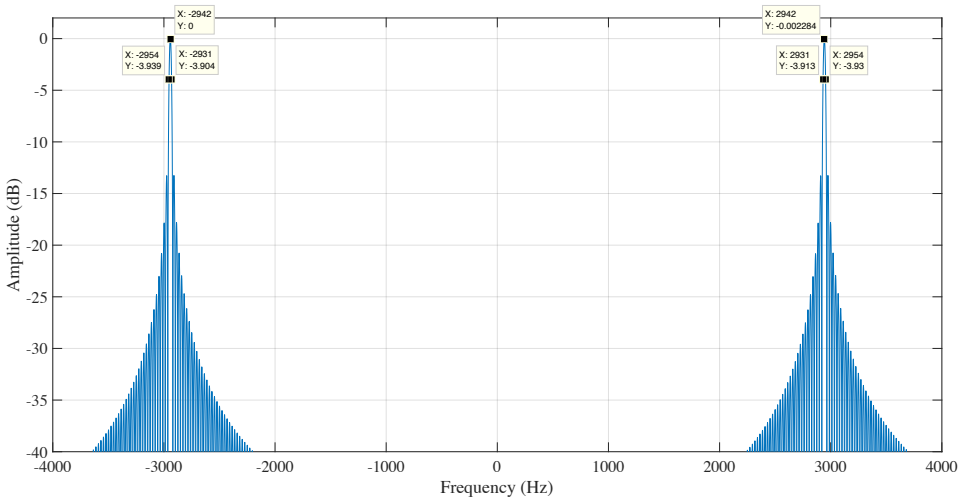

Fig. 3.9: Triangular FMCW beat frequency spectrum for a 1 m target.

The two sinc function response of Fig. 3.9 corresponds to the down and up chirp beat frequency of a single point target at 1 m away from the radar. Both beat frequencies are at -2942 Hz and 2942 Hz respectively. By equation (3.14) this equals to a target at 1 m in range. Furthermore, the -3.9 dB bandwidth of both beat frequency's is equal to 23 Hz. Which is consistent with the calculated bandwidth of the beat frequency (3.21). Besides, to match the sawtooth case regarding maximum detectable range and beat frequency bandwidth, the triangular FMCW modulation period should be doubled.

Finally, acoustic FMCW radar has a very fine range resolution and accuracy due to the low speed of propagation that could be measured in millimeters. However, and also due to

the low speed of propagation, acoustic FMCW radars are limited in range and could only detect close range targets unambiguously. Furthermore, when measuring far range target's that are less than the maximum detectable range, a widening in the beat frequency mainlobe bandwidth is present resulting in a degradation in range resolution due to the overlap between the transmitted and received waveforms being smaller than the electromagnetic case. Therefore, acoustic FMCW is suitable for high accuracy short range applications.

3.4 Narrowband and Wideband FMCW

Transmitted signals in general are categorized to three main categories based on their bandwidths. Narrowband, Wideband, and Ultra-wideband. For the -10 dB power spectral density of the transmitted frequency bandwidth, a narrowband signal has a fractional bandwidth that is less or equal to 0.01. Whereas, a wideband signal has between 0.01 and 0.25 fractional bandwidth. However, an Ultra-wideband signal has a fractional bandwidth that is greater than 0.25 [46]. The transmitted signal's fractional bandwidth can be calculated using (3.22)

$$Fractional\ Bandwidth = \frac{2(f_h - f_l)}{(f_h + f_l)} = \frac{\Delta F}{f_0} \tag{3.22}$$

where f_l and f_h are the low and high of the frequency sweep of the transmitted signal. This could be also written as the bandwidth of the transmitted signal ΔF over the center frequency f_0.

For a FMCW radar system, the signal is a linearly modulated chirp with a start and end frequency that covers the chirp bandwidth. In most electromagnetic FMCW radars, however, the narrowband assumption is made due to the relatively small fractional bandwidth. Whereas when using an acoustic FMCW, and due to the low speed of propagation, the fractional bandwidth could be greater than 0.25, and thus, considered an ultra-wideband case. Therefore, for a wider bandwidth, the FMCW radar system will be capable of higher range resolution and range measurement accuracy. However, the effect on Doppler measurement is yet to be addressed.

When transmitting a triangular FMCW, both range and Doppler measurements are obtained at the same time from the difference in the up and down sweep of the beat frequencies (3.14) and (3.15). By taking the sum of the difference of the two beat frequencies, velocity is then a function of Doppler shift, speed of propagation and radar center frequency. The general term of radar Doppler shift for a point target moving with velocity V is shown in (3.8).

For the narrowband case, the Doppler shift is a function of the center frequency since the fractional bandwidth is less than or equal to 0.01, which indicates that the deviation between the center frequency and the low and high frequency components of the transmitted signal is negligible, and therefore, the difference between the Doppler measurement at f_l and f_h is less than 1%.

To calculate the Doppler shift variation over the transmitted frequency interval for a given target moving with the velocity V

$$\Delta f_d = \frac{2V\Delta f_0}{c} \tag{3.23}$$

where Δf_d is the variation of the Doppler shift, and Δf_0 is the interval between the start and end frequency of the transmitted signal. Fig. 3.10 shows the difference between assumed vs actual Doppler shift of an electromagnetic FMCW radar that operates at a frequency of 10 GHz, and transmits a 100 MHz chirp waveform. Which yields a fractional bandwidth equals to 0.01, satisfying the narrowband assumption. The target is assumed to be traveling at 100 m/s.

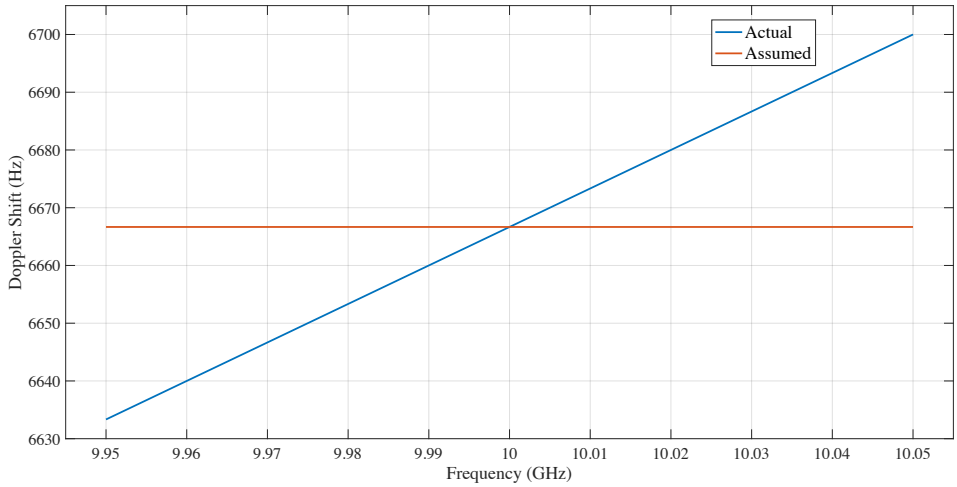

Fig. 3.10: Assumed vs actual Doppler shift of an electromagnetic FMCW with 100 m/s velocity.

The difference between the assumed and the actual Doppler shift resulting from 100 m/s moving point target is shown to be 34 Hz or less from the center frequency Fig. 3.10. When taking the percentage of the error in Doppler between the assumed and actual measurements, a maximum of 0.5% is observed between the two values, and a 1%

difference is shown when comparing the lower and upper Doppler shift bounds as shown in fig. 3.11. This will correspond to a maximum error of 1 m/s when measuring the 100 m/s moving point target.

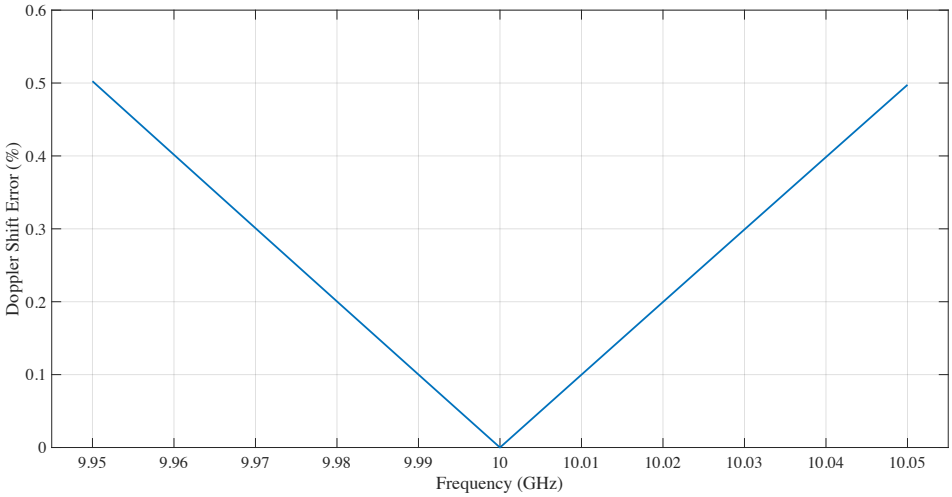

Fig. 3.11: Change in Doppler shift compared to the center frequency for an electromagnetic FMCW.

By analyzing both Fig. 3.10 and 3.11, it is apparent that an error of less or equal to 1% in the Doppler shift resulting from using the narrowband assumption of equation (3.22) is negligible. However, when using the acoustic radar system with a transmit waveform bandwidth set to 25 kHz, covering the band of (25-50 kHz), and a center frequency at 37.5 kHz. This will result in a system fractional bandwidth of 0.66. Fig. 3.12 shows the Doppler shift of a point target moving with a 0.1 m/s velocity.

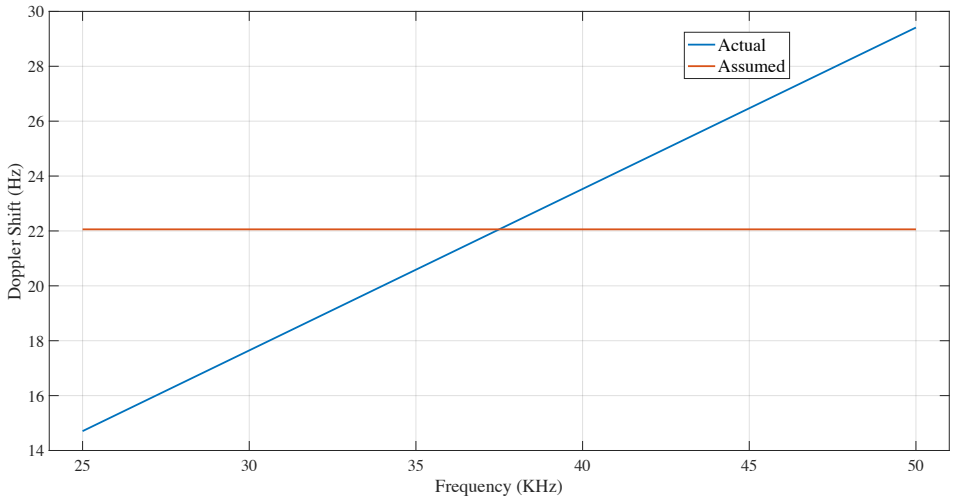

Fig. 3.12: Assumed vs actual Doppler shift of an acoustic FMCW with 0.1 m/s velocity.

Here, the acoustic radar 25 kHz bandwidth, results in a maximum 7 Hz difference of Doppler shift between the actual and the corresponding center frequency Doppler. This difference in Doppler measurement is shown as an error percentage in Fig. 3.13.

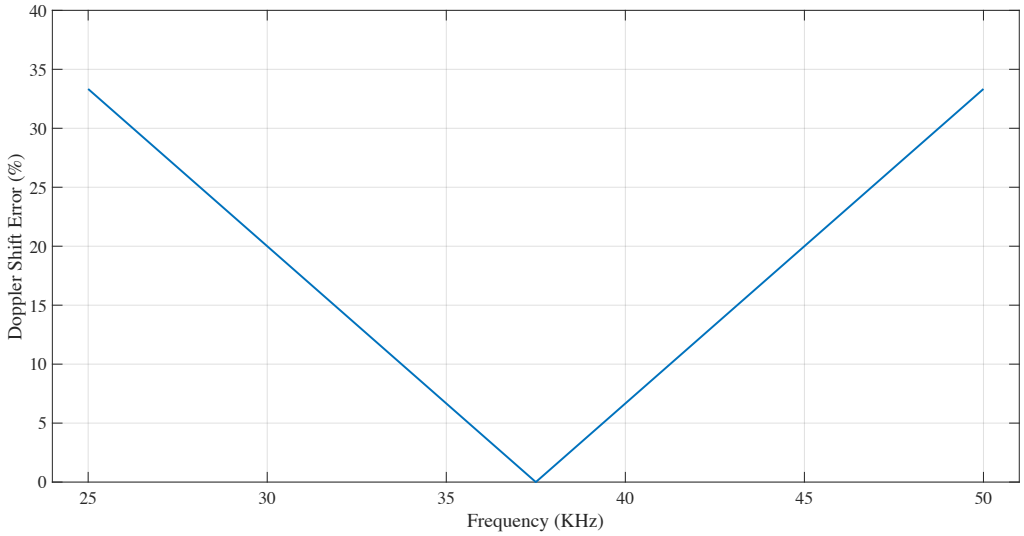

Fig. 3.13: Change in Doppler shift compared to the center frequency for an acoustic FMCW.

Figure. 3.13 clearly indicates a larger error percentage when comparing the Doppler shift across the entire frequency sweep of the returned waveform. A 33% maximum error is present when measuring Doppler frequency for an acoustic FMCW, this indicates a possible variation of one third of the true velocity return when estimating a moving target under this fractional bandwidth. Therefore, the relative error in the measurement of the velocity is proportional to the error of the Doppler frequency, and inversely proportional to the radar transmit frequency. Table. 3.1 shows the Doppler shift at several transmitted center frequencies, and the relative Doppler error with a 25 kHz bandwidth for a single point target moving at 0.1 m/s, when transmitting an acoustic FMCW.

Table 3.1: Transmitted frequency vs maximum relative velocity error for a fixed bandwidth.

Transmitted Center Frequency (kHz)	**Doppler Shift (Hz)**	**Maximum Relative Error (%)**
25	14.71	50
50	29.41	25
100	58.82	12.5
150	88.24	8.33
200	117.6	6.25

Table. 3.2 shows the maximum Doppler shift error from the center frequency in Hz, for different bandwidths, for a 0.1 m/s moving point target, and are independent of frequency.

Table 3.2: Bandwidth vs Doppler shift error independent of frequency.

Bandwidth (kHz)	**Doppler Shift Error (Hz)**
1	0.29
5	1.47
10	2.94
25	7.35
50	14.7

Both Table 3.1 and 3.2 represent the effect of bandwidth and center frequency on the Doppler shift error, which results in a deviation of the velocity measurement regarding a moving target. Therefore, the fractional bandwidth value for the acoustic transmitted waveform provides a demonstration of the possible velocity measurement error for various target velocities.

In summary, since the frequency of acoustic FMCW radars is low compared to electromagnetics, it is more likely to have high fractional bandwidth. Therefore, it was shown that for acoustic FMCW radars with high fractional bandwidths, the response of the target is no longer the response of only the center frequency, and therefore, the narrowband assumption is not possible to maintain. For that, when using triangular FMCW radars, it is

desired to have a small fractional bandwidth in order for the velocity of the target to be accurately determined.

Chapter 4: Echoic Flow Theory

In this chapter we introduce the echoic flow theory development based on using both relative range and Doppler velocity to calculate the echoic flow parameter tau (τ), and then move towards the advancement of using the range rate sign convention in the derivative of the echoic flow parameter tau dot ($\dot{\tau}$) which results in different guidance scenarios. In addition, a detailed derivation of the proposed precision of the echoic flow measurement when using range and Doppler, with an emphasis on using a triangular FMCW acoustic radar to extract range and Doppler for each individual pulse.

4.1 Echoic Flow Development

Flow theory in general, and specifically echoic flow measures the time for two objects to come into contact with each other [1] [2] and [7]. The time it takes an object to close the gap with another object is called the Time to Contact (TTC) and is noted by the parameter τ. Therefore, tau in general is a measurement of any sensory parameter over the rate of change of that parameter in time. The time it takes two objects to collide with each other is governed by equation (4.1) as follows

$$\tau_x = \frac{x}{\dot{x}} \tag{4.1}$$

where x is the measurable sensory parameter, and $\dot{x}$ is the rate of change of that parameter over time [5]. Tau has units of time since any measurable parameter divided by its rate of change will result in a time value. For echoic flow, the sensory parameter is usually the radial range since radars mainly measure range to an object. Echoic flow could also refer to the azimuth or elevation angle measurement of a radar system given that the radar system is able to measure its azimuth or elevation angle to the target.

Therefore, echoic flow can be computed from measurements of radial range, as might be measured by a radar or active sonar and is given by:

$$\tau_r(t) = \frac{r(t)}{\dot{r}(t)} \tag{4.2}$$

Where $r(t)$ is the current range to a detected object and $\dot{r}(t)$ is the rate of change of range, or instantaneous velocity. Thus, $\tau_r(t)$ is a direct measure of the time to contact (TTC) and hence has units of time. For example, if a radar sensor platform moving towards a stationary object with a velocity of 2 m/s and the object is 10 m away, then the time to collision $\tau_r(t) = 5$ s.

In this section I will briefly explain the echoic flow theory for the parameters τ and the time derivative of tau ($\dot{\tau}$) and how they can be calculated from the radar's radial range measurement. The theory will include consideration of the cases when both the radar platform and target are moving.

The radar target geometry is shown in Fig. 4.1, where the radar platform is at a location r_R moving with velocity $\dot{r}_R$ and acceleration $\ddot{r}_R$ towards a target at location $r_T$with

velocity $\dot{r}_T$ and acceleration $\ddot{r}_T$. This results in a relative velocity between the radar platform and the target $= \dot{r}_T - \dot{r}_R$, whereas the gap $r(t)$ is the target's relative range measured by the radar and equals $r_T - r_R$.

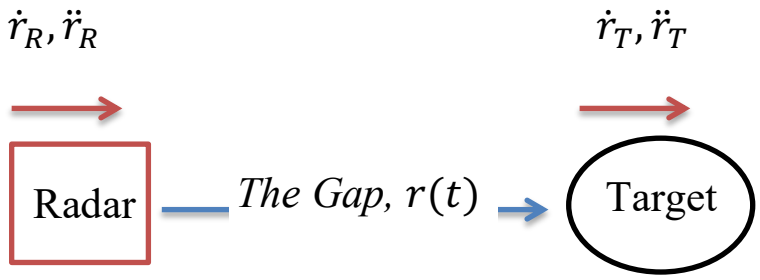

Fig. 4.1: Radar with velocity $\dot{r}_R$ and acceleration $\ddot{r}_R$ approaching a target r m away with velocity $\dot{r}_T$ and acceleration $\ddot{r}_T$.

In general, to measure the relative velocity between a target and the radar, two methods can be used. Either the range of two consecutive pulses can be subtracted from one and other and divided by the time interval or, if a coherent radar is employed, Doppler processing can be used.

4.1.1 Echoic Flow Using Relative Range Velocity

The two pulse method for velocity estimation is described mathematically by (4.3), where $r[n]$ is the range measured with pulse n at time $t[n]$, and $r[n-1]$ is the previous range at time $t[n-1]$.

$$\tau_r[n] = \frac{r[n]}{r[n] - r[n-1] \Big/ t[n] - t[n-1]} \tag{4.3}$$

Using (4.3) introduces a sign convention to differentiate a gap that is closing and a gap that is opening. Assuming that range is always a positive value, then when the current measured range is smaller than the previous measured range the sign of τ_r will be negative indicating that the gap between the radar and the target is closing. Conversely, if the second measured range is greater than the previous measured range, then the sign of τ_r is positive and the gap is opening. This sign convention would also be valid when using Doppler to estimate velocity, section 4.1.2.

$$sign(\tau_r) = \begin{cases} -\text{ve} & \text{if } r[n] < r[n-1] \text{ (Gap closing)} \\ +\text{ve} & \text{if } r[n] > r[n-1] \text{ (Gap opening)} \end{cases} \tag{4.4}$$

In flow theory literature, the gap x is assumed to be negative [5] in order for the flow parameter τ_x to have a negative value, which assures a consistent gap closer. This assumption is not valid when the gap is opening. However, by assuming that range is always a positive value in (4.3) a differentiation between a gap that is opening and a gap that is closing is possible. The effect of gap opening vs gap closing will be presented in section 4.1.3.

4.1.2 Echoic Flow Using Doppler Velocity

When using a coherent radar, both range to the target and its Doppler velocity can be extracted. Here echoic flow can be instantaneously calculated for each pulse as shown in equation (4.5).

$$\tau_r[n] = -\frac{r[n]}{\dot{r}[n]} \tag{4.5}$$

where $r[n]$ is the range measured with observation n, and $\dot{r}[n]$ is the Doppler velocity to the target at observation n. By assuming the range to the target is always positive, Doppler velocity also presents a sign change between opening and closing a gap. When a target is moving towards the radar, hence gap is closing, the Doppler shift is positive, while if the target is pulling away from the radar, hence the gap is opening, the Doppler shift is negative [13]. This is the opposite of the sign convention presented in (4.4). Therefore, when using Doppler velocity to calculate echoic flow parameter τ_r, a negative sign is added to reverse the Doppler shift sign, equation (4.5), which results in a negative echoic flow when gap is closing and a positive echoic flow when gap is opening. This will match the relative range velocity case in (4.4).

4.1.3 The Derivative of Echoic Flow

For better understanding of the derivative of the echoic flow parameter, we will derive the second order flow equation and solve it to show the motion equations. Therefore, here

we will assume x in (4.1) to be any sensory parameter and derive the motion equations based on that assumption.

From (4.1) we can take the time derivative of τ to get an equation that involves $x, \dot{x}\ and, \ddot{x}$. By using the Quotient rule

$$\dot{\tau} = \frac{\dot{x}\,\dot{x} - x\,\ddot{x}}{\dot{x}^2} = 1 - \frac{x\,\ddot{x}}{\dot{x}^2} \tag{4.6}$$

Equation (4.6) shows $\dot{\tau}$ as a dimensionless quantity and is a second order differential equation. This equation can be solved if $\dot{\tau}$ is assumed to be constant. Therefore, solving the second order differential equation yield the solution

$$x = x_0 \left(\frac{x_0}{\dot{x}_0}\right)^{-\frac{1}{\dot{\tau}}} \left(\frac{x_0}{\dot{x}_0} + \dot{\tau}\ t\right)^{\frac{1}{\dot{\tau}}} \tag{4.7}$$

by rearranging the equation and using the exponential and the natural logarithm functions

$$x = x_0\ e^{\frac{1}{\dot{\tau}}\ln\left(\frac{x_0}{\dot{x}_0} + \dot{\tau}\ t\right)}\ e^{-\frac{1}{\dot{\tau}}\ln\left(\frac{x_0}{\dot{x}_0}\right)} \tag{4.8}$$

$$x = x_0\ e^{\frac{1}{\dot{\tau}}\ln\left(\frac{\dot{\tau}\ t\ \dot{x}_0 + x_0}{x_0}\right)} \tag{4.9}$$

by taking the exponential and the natural logarithm functions out of the equation

$$x = x_0 \left(\frac{\dot{\tau}\ t\ \dot{x}_0 + x_0}{x_0}\right)^{\frac{1}{\dot{\tau}}} \tag{4.10}$$

therefore, rearranging the equation and substituting with $\tau = {}^{x}/_{\dot{x}}$.

$$x = x_0 \left(1 + \frac{\dot{\tau}\, t}{\tau_0}\right)^{\frac{1}{\dot{\tau}}} \tag{4.11}$$

To drive the time derivative of x, the Chain rule is used

$$\dot{x} = x_0 \frac{1}{\dot{\tau}} \left(1 + \frac{\dot{\tau}\, t}{\tau_0}\right)^{\left(\frac{1}{\dot{\tau}}\right)-1} \left(\frac{\dot{\tau}}{\tau_0}\right) \tag{4.12}$$

substituting (4.1) into (4.12)

$$\dot{x} = x_0 \frac{1}{\dot{\tau}} \left(\frac{\dot{\tau}\, \dot{x}_0}{x_0}\right) \left(1 + \frac{\dot{\tau}\, t}{\tau_0}\right)^{\left(\frac{1}{\dot{\tau}}\right)-1} \tag{4.13}$$

$$\dot{x} = \dot{x}_0 \left(1 + \frac{\dot{\tau}\, t}{\tau_0}\right)^{\left(\frac{1}{\dot{\tau}}\right)-1} \tag{4.14}$$

equation (4.14) represents the rate of change of x. To get the second order derivative of x, the Chain rule is used again as follows

$$\ddot{x} = \dot{x}_0 \left(\frac{1}{\dot{\tau}} - 1\right) \left(1 + \frac{\dot{\tau}\, t}{\tau_0}\right)^{\left(\frac{1}{\dot{\tau}}\right)-2} \left(\frac{\dot{\tau}}{\tau_0}\right) \tag{4.15}$$

$$\ddot{x} = \dot{x}_0 \left(\frac{\dot{\tau}}{\dot{\tau}\, \tau_0} - \frac{\dot{\tau}}{\tau_0}\right) \left(1 + \frac{\dot{\tau}\, t}{\tau_0}\right)^{\left(\frac{1}{\dot{\tau}}\right)-2} \tag{4.16}$$

rearranging equation (4.16)

$$\ddot{x} = \frac{\dot{x}_0}{\tau_0} (1 - \dot{\tau}) \left(1 + \frac{\dot{\tau}\, t}{\tau_0}\right)^{\left(\frac{1}{\dot{\tau}}\right)-2} \tag{4.17}$$

The equation of motion for $x, \dot{x}\ and\ \ddot{x}$ are given in (4.11), (4.14) and (4.17). The 0 denotes the initial condition at time $t = 0$. By setting $\dot{\tau}$ to a constant value, the motion curves of gap closing will change.

Here a plot of the motion curves of flow theory, made by plotting the motion equation curves of (4.11), (4.14) and (4.17), while setting all initial conditions to unity. Fig. 4.2 shows the flow theory motion curves.

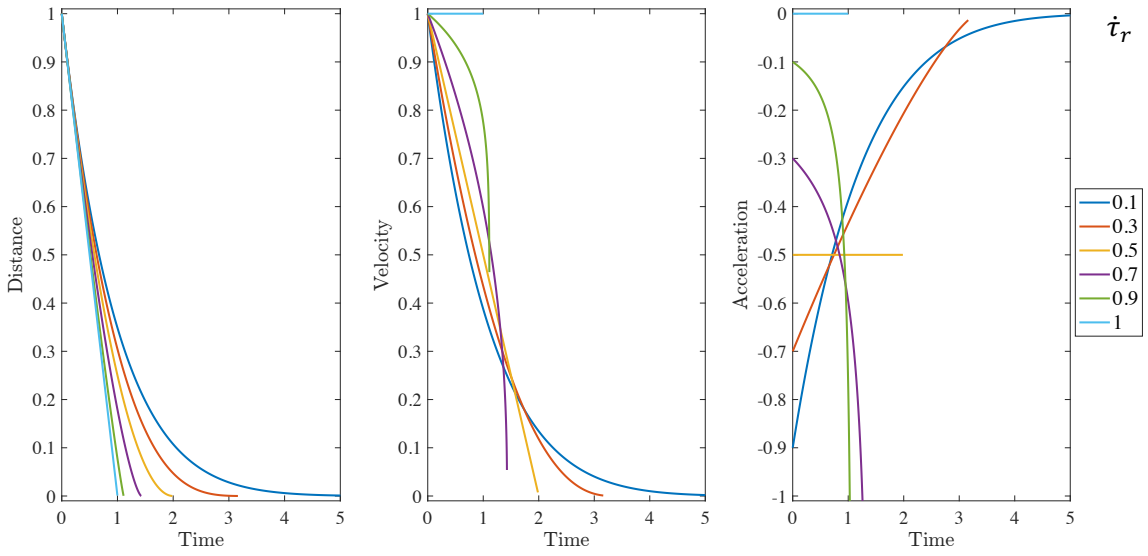

Fig. 4.2: Motion curves of gap x, velocity $\dot{x}$ and acceleration $\ddot{x}$ with time.

Furthermore, by focusing on the case of radial range in equation (4.2), the time derivative of τ_r is a second order differential equation with terms for range, velocity and acceleration, where (4.6) can be expressed as

$$\dot{\tau}_r = \frac{\mathrm{d}\tau_r}{\mathrm{d}t} = 1 - \frac{r[n]\,\ddot{r}[n]}{\dot{r}^2[n]} = 1 - \frac{\tau_r[n]\,\ddot{r}[n]}{\dot{r}[n]} \tag{4.18}$$

by rearranging (4.18) an expression for acceleration, $\ddot{r}[n]$, can be obtained

$$\ddot{r}[n] = \frac{|\dot{r}[n]|(1 - \dot{\tau}_r\,)}{\tau_r[n]} \tag{4.19}$$

The absolute symbol $|\cdot|$ is introduced in (4.19) to ensure that the behavior of $\ddot{r}[n]$ is governed by the sign of $\tau_r[n]$ presented in (4.4). Therefore, when following the convention $\dot{\tau}_r > 0$ [5], three motion scenarios can be defined based on the movement between the radar and the target.

For stationary targets, the radar is taken to be moving towards the target, Fig. 4.1, and hence the gap between the radar and the target is closing, which leads the sign of τ_r being negative. Based on the $\dot{\tau}_r$ value we have five conditions for approaching a stationary target, and follows the same curves of Fig 4.2.

When setting $\dot{\tau}_r = 1$, colored in light blue, then no braking is applied and therefore a collision will occur. The second condition is setting $\dot{\tau}_r = 0.5$, yellow curve, which applies a linear braking force to the radar platform velocity and the platform comes to rest at the target location. In echoic flow literature it is said that the gaps in both range and velocity close at the same time. Furthermore, for $0 < \dot{\tau}_r < 0.5$, blue and red curves, an early braking strategy is applied, where the radar platform starts with a strong braking force, that decreases while approaching the target. Again, the platform comes to rest at the target location now with a gentle braking strategy. However, if $\dot{\tau}_r$ is set to $0.5 < \dot{\tau}_r < 1$, shown

in purple and green, a late braking strategy is applied by the radar platform, resulting in a small braking force that increases rapidly as the target is approached. Now the final braking force is, potentially, infinite and it is common the approach ends in a soft collision [7]. Finally, if $\dot{\tau}_r > 1$, the radar platform will accelerate towards the target and collides with a high velocity.

Furthermore, when the radar is approaching a moving target that has a velocity less than the radar's velocity $\dot{r}_T < \dot{r}_R$, it is clear that the relative velocity still has a negative value. This results in a negative τ_r and hence, a behavior similar to that of a stationary target except that it takes more time to close the range gap due to the movement of the target. It is important to note, however, that now when the gap is closed, the speed of the radar is matched to the target's speed if $0 < \dot{\tau}_r < 1$ rather than coming to rest, i.e. the relative, not absolute, velocity is zero. We may think of this as the velocity gap being closed. If $\dot{\tau}_r \geq 1$ the platform controlled by the radar will collide with the target and the relative velocity will be greater than zero.

However, if the target is pulling away from the radar, the gap between the radar platform and target will initially be opening, resulting in a positive velocity, and a positive τ value (4.4). By applying (4.19) for $0 < \dot{\tau}_r < 1$, the radar platform will accelerate until the speed of the radar is matched with the speed of the target, which results in a zero relative velocity and an infinity τ value. However, unlike the previous two cases, the range gap is not closed when the velocities match. This is undesirable for target approach applications.

To ensure the radar platform completes its approach to the target, and closes the range gap, the following restrictions are applied to (4.19)

$$\tau_r[n] = \begin{cases} \dfrac{r[n]}{\dot{r}[n]} & \text{when} \quad |\tau_r[n]| < \tau_{r\,max} \\ \tau_{r\,max} & \text{when} \quad |\tau_r[n]| \geq \tau_{r\,max} \end{cases} \tag{4.20}$$

$$\dot{r}[n] = \begin{cases} \dot{r}[n] & \text{when} \quad \dot{r}[n] > \dot{r}_{min} \\ \dot{r}_{min} & \text{when} \quad \dot{r}[n] \leq \dot{r}_{min} \end{cases} \tag{4.21}$$

Equation (4.20) will restrict the value of τ_r to a positive maximum value that is a function of kinematic parameters of the radar platform and the time required to close the gap. Also, the minimum relative velocity applied by the radar platform is limited, (4.21), to eliminate the effect of a zero relative velocity.

These modifications to the EF theory result in the radar platform accelerating until the speed of the platform is greater than the target's speed and the value of τ_r is less than $\tau_{r\,max}$. Now the situation has been converted to the case where the target has a lower velocity than the radar and the range gap will close and the radar platform velocity matching the target's velocity.

4.2 Precision of Echoic Flow Measurements

Precision for radar systems describes how well a radar measurement can be repeated for the same quantity. In other words, precision is represented by the standard deviation of the measured parameter. From [13] and [47], the square root of the Cramer-Rao lower bound (CRLB) is stated to be the lowest possible precision of a measurement.

While the square root of the CRLB is considered to be the lowest possible precision measurement, a derivation in [13] and [47] shows that both range and Doppler velocity precision are a function of resolution and signal to noise ratio as shown below.

$$\sigma_R = \frac{\Delta \mathrm{R}}{\sqrt{SNR}} \tag{4.22}$$

$$\sigma_V = \frac{\Delta \mathrm{V}}{\sqrt{SNR}} \tag{4.23}$$

Where ΔR is the radar's range resolution which is inversely proportional to the transmitted waveform's bandwidth, $\Delta R = c/2\ B$, and ΔV is the radar's velocity resolution which is inversely proportional to the dwell time, $\Delta V = c/(2\ T\ f_o)$, equation (4.24) and (4.25) respectively shows both range and Doppler velocity precision.

$$\sigma_R = \frac{c}{2\ B\ \sqrt{SNR}} \tag{4.24}$$

$$\sigma_V = \frac{c}{2\ T\ f_o\ \sqrt{SNR}} \tag{4.25}$$

where B is the transmitted waveform bandwidth, f_0 is the center frequency of the transmitted waveform, T is the dwell time, and c is the speed of propagation.

Since the echoic flow parameter is a function of both range and range rate, then a formula is examined to accommodate both range and range rate precisions into account. From [48], if $z = f(x, y)$, where $f(x, y)$ explains the relation between the estimated parameter z and the measurements x and y, then

$$\sigma_z = \sqrt{\left(\frac{\delta z}{\delta x}\,\sigma_x\right)^2 + \left(\frac{\delta z}{\delta y}\,\sigma_y\right)^2} \tag{4.26}$$

this equation (4.26) can be written as a function of both range and Doppler velocity since they are both part of the echoic flow equation as follows

$$\sigma_\tau = \sqrt{\left(\frac{\delta \tau}{\delta R}\,\sigma_R\right)^2 + \left(\frac{\delta \tau}{\delta V}\,\sigma_V\right)^2} \tag{4.27}$$

By taking the partial derivative of τ with respect to range, given that $\tau = R/V$

$$\frac{\delta \tau}{\delta R} = \frac{1}{V} \tag{4.28}$$

and the partial derivative of τ with respect to velocity

$$\frac{\delta \tau}{\delta V} = \frac{-R}{V^2} \tag{4.29}$$

and by substituting the partial derivative of both (4.28) and (4.29) into (4.27)

$$\sigma_\tau = \sqrt{\left(\frac{\sigma_R}{V}\right)^2 + \left(\frac{-R\,\sigma_V}{V^2}\right)^2} \tag{4.30}$$

From substituting both (4.24) and (4.25), (4.30) can be written as

$$\sigma_\tau = \sqrt{\left(\frac{c}{2\,B\,V\,\sqrt{SNR}}\right)^2 + \left(\frac{-R\,c}{2\,T\,f_o\,V^2\,\sqrt{SNR}}\right)^2} \tag{4.31}$$

$$\sigma_\tau = \sqrt{\frac{4\,c^2\,V^2\,SNR\left(R^2\,B^2 + V^2\,T^{\,2}{f_o}^{\,2}\right)}{16\,B^2\,V^6\,T^{\,2}{f_o}^{\,2}\,SNR^2}} \tag{4.32}$$

$$\sigma_\tau = \frac{c\sqrt{\left(R^2\,B^2 + V^2\,T^{\,2}{f_o}^{\,2}\right)}}{2\,B\,V^2\,T\,f_o\,\sqrt{SNR}} \tag{4.33}$$

Equation (4.33) represents the precision of echoic flow, where it contains the speed of propagation c, the transmitted wave's bandwidth B, the center frequency f_o, the dwell time T and the signal to noise ratio SNR. All the previous parameters are part of the range and velocity precision shown in (4.24) and (4.25). However, the (4.33) also is a function of range R and velocity V. This indicates that the echoic flow precision measurement to a target is also dependent on the target's measured range and velocity. Given that the range R is in the numerator, then a far range target will have a negative precision effect on the echoic flow measurement. While, since the velocity V in the denominator is squared, a high velocity target will result in a finer echoic flow precision.

Furthermore, when using a triangular FMCW radar to measure both range and Doppler, an overlap factor between the transmitter and the receiver will affect the precision of both

range and Doppler measurement, which will have an effect on the echoic flow precision. See section 3.3.

Therefore, the overlap of the transmit and receive waveform is a function of modulation period and propagation time delay. When the overlap is decreased a broadening in the beat frequency's main lobe affects the range resolution as shown in (3.19). Hence, when setting a minimum overlap to a percentage, the equation could be written as

$$\frac{1}{OL} = \frac{{T_m}/_2}{{T_m}/_2 - t_{d\ max}} \tag{4.34}$$

Where OL is the overlap fraction that ranges from 0 when no overlap is present, and 1 with %100 overlap. We can substitute the maximum time delay with maximum range where $t_{d\ max} = {2\ R_{max}}/_c$, presented in (4.35).

$$\frac{1}{OL} = \frac{T_m}{T_m - \frac{4\ R_{max}}{c}} \tag{4.35}$$

By taking into account the overlap effect on both range and Doppler precision measurement, the precision equation of τ when using a triangular FMCW can be rewritten as a function of maximum detectable range, which is a factor of the percentage overlap.

$$\sigma_\tau = \frac{c^2 \sqrt{\left(4\ R^2\ \Delta F^2 + V^2\ {T_m}^2 {f_o}^2\right)}}{2\ \Delta F\ V^2\ f_o \sqrt{SNR}\ (c\ T_m - 4\ R_{max})} \tag{4.36}$$

From equation (4.36) it is apparent that both range and velocity measurement have an effect on the standard deviation of the output τ. Here, two ways of measuring the precision of tau are presented and compared. A theoretical model using (4.36) and an acoustic triangular FMCW radar simulation was performed. For the first set, the velocity measurement was set to a constant $v = 0.1\ m/s$ and R_{max} is calculated using (4.35), while the radar parameters are set as follows in Table 4.1.

Table 4.1: Acoustic Triangular FMCW Radar Parameters

Parameter	**Value**
Modulation Bandwidth (ΔF)	25 KHz
Modulation Period (T_m)	0.2 s
Center Frequency (f_o)	100 KHz
Speed of Propagation (c)	340 m/s
Signal to Noise Ratio (SNR)	20 dB

Fig. 4.3 shows the curves of both theoretical and simulated tau precision when having an overlap that ranges from %50 to %90. Here, the blue lines indicate the simulated precision using an acoustic triangular FMCW radar, and the red lines represents the theoretical τ precision calculated through equation (4.36).

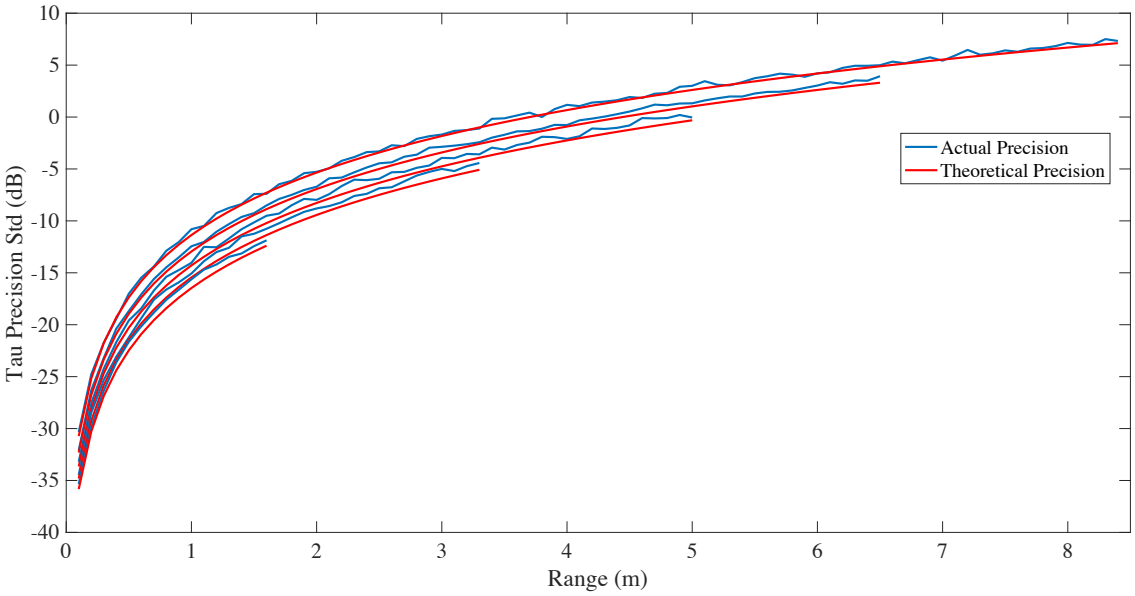

Fig. 4.3: Tau Precision curves vs range.

From Fig. 4.3, five sets are presented. The first set shows the theoretical and the actual precision of a %90 maximum overlap between the transmit and received triangular waveforms. The maximum detectable range for a %90 overlap is 1.7 m, please refer to section 3.3.2 for more information about the maximum detectable range of an acoustic FMCW radar. It is apparent that for a %90 overlap, the tau precision is the finest and the actual precision is laying on top of the theoretical precision, which coincides with the theory that the square root of CRLB is the lowest possible precision that can be achieved.

Furthermore, the other four sets, %80, %70, %60 and %50 overlaps are presented in Fig. 4.3, with maximum detectable ranges of 3.4, 5.1, 6.8, and 8.5 m respectively. All curves shown follow the theory of having the simulated radar precision resting over the

theoretical lower bound tau precision calculated using (4.36). In addition, the increase in target range has a negative effect on echoic flow precision, while the increase in transmit and receive signal overlap has a positive effect on the echoic flow precision measurement.

For the second set, the range measurement was fixed to a constant equaling the maximum detectable range for each transmit and receive waveform overlap, while velocity measurement is arranged to vary from zero to maximum detectable velocity, and the remaining radar parameters are set based on Table 4.1.

To calculate the maximum detectable velocity V_{max}, an equation was driven from the beat frequency of a triangular FMCW radar as shown below. Please refer to section 3.2 for more information about calculating the beat frequency of an acoustical FMCW radar.

From the up and down beat frequency (3.10) and (3.11) there are two frequency shifts that corresponds to both range and Doppler frequency shift

$$f_b = f_R + f_D = \frac{\Delta F}{T_m}\frac{4R}{c} + \frac{2Vf_0}{c} \tag{4.37}$$

however, the Doppler shift must not exceed the range shift in order for the Doppler shift to be valid, therefore, $f_R \geq f_D$

$$\frac{\Delta F}{T_m}\frac{4R}{c} \geq \frac{2Vf_0}{c} \tag{4.38}$$

here, we can rearrange (4.38) and write the equation in terms of R_{max} and V_{max} as shown below

$$\frac{\Delta F}{T_m}\frac{4R_{max}}{c} = \frac{2\,V_{max}\;f_0}{c} \tag{4.39}$$

therefore, by rearranging (4.39) V_{max} is a function of R_{max}, frequency deviation ΔF, modulation period T_m, and center frequency f_0 presented in (4.40).

$$V_{max} = \frac{2\,\Delta F\;R_{max}}{T_m\;f_o} \tag{4.40}$$

Considering the previous range and velocity limitations, we can show the link between the percentage overlap of transmit and receive waveforms with the maximum range and velocity measurements possible, along with echoic flow precision measurement. Fig. 4.4 determines the echoic flow precision measurement when varying Doppler velocity for an acoustic triangular FMCW radar along with the theoretical precision's lower bound calculated using (4.36). While limiting V_{max} as a function of R_{max} by using (4.40) and setting the target's range to R_{max} for each individual percentage overlap.

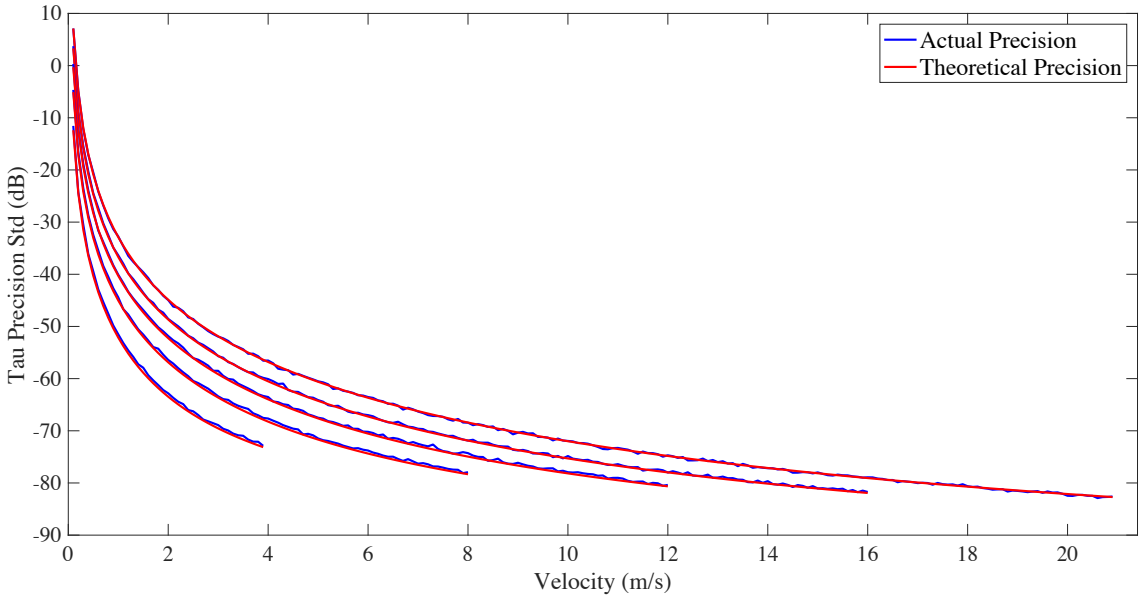

Fig. 4.4: Tau Precision curves vs velocity.

From Fig. 4.4, five different percentage overlaps were used as in Fig. 4.3. For the %90 overlap, the EF precision is the smallest of all cases presented, which is what is expected for a high percentage overlap. However, and on the contrary to varying range, by increasing the target's velocity, the echoic flow measurement becomes more precise, which indicates a positive effect on the measurement. This effect can be shown in (4.36) by having the squared velocity parameter in the denominator, compared to the range being in the numerator.

Furthermore, by decreasing the percentage overlap as shown for the four remaining sets, it is apparent that while the maximum velocity can be increased due to the maximum range increase, the tau precision is affected negatively compared with the same velocity.

In conclusion, echoic flow precession measurement is shown to be a function of radar waveform parameters along with both range and Doppler velocity measurement. Additionally, for the same signal to noise ratio, when the range measurement to a target increases, the echoic flow measurement becomes less precise, while if the target's velocity increases, the echoic flow measurement becomes more precise. Though, if using an FMCW radar to measure echoic flow by extracting both range and Doppler velocity, the maximum allowable percentage overlap between the transmitted and received waveform has a noticeable effect on the EF precision, which was shown in both theory and simulation.

4.3 Conclusions

In this chapter, I have introduced the echoic flow theory, originally developed from the general flow theory. The echoic flow parameter τ was shown to be feasible to extract using the output of a radar system, like range, relative velocity and Doppler velocity for coherent radars. Additionally, the derivative of the echoic flow parameter $\dot{\tau}$ was introduced, and the motion equations that resulted from solving the $\dot{\tau}$ second order differential equation were simulated. The cases of both stationary and moving targets were presented and restrictions were introduced to ensure gap closer when the target is moving away.

Finally, the precision of the echoic flow output τ was calculated by establishing a relationship between the square root of the CRLB of range and velocity measurements in a radar system, and a confirmation through simulation of the theoretical tau precision equation when using a Triangular FMCW radar was presented.

Chapter 5: Development of The Experimental Testbed

An acoustic radar system is developed and mounted on a robotic platform for bio inspired guidance and control applications using echoic flow. The system consists of ultrasound microphones and loudspeakers as the radar sensors. Embedded real time processor, FPGA board and, input/output modules, along with a Windows operating system laptop and power batteries. Furthermore, two robotic platforms with built in ultrasonic sensors that measure range were purchased. An in-depth explanation of the experimental testbed is in the following sections of this chapter.

5.1 Mobile Robot

Two individual mobile robots were purchased to carry a radar system for the purpose of testing the echoic flow concept in various scenarios. The two robotic platforms with built in ultrasonic sensors that measure range were purchased from Adept MobileRobots Inc. Pioneer 3-DX shown in Fig. 5.1, has a maximum speed of 1.7 m/s and a 360° of rotational movement freedom. The robotic platform can be controlled via a joystick or by using a laptop that can be mounted on top.

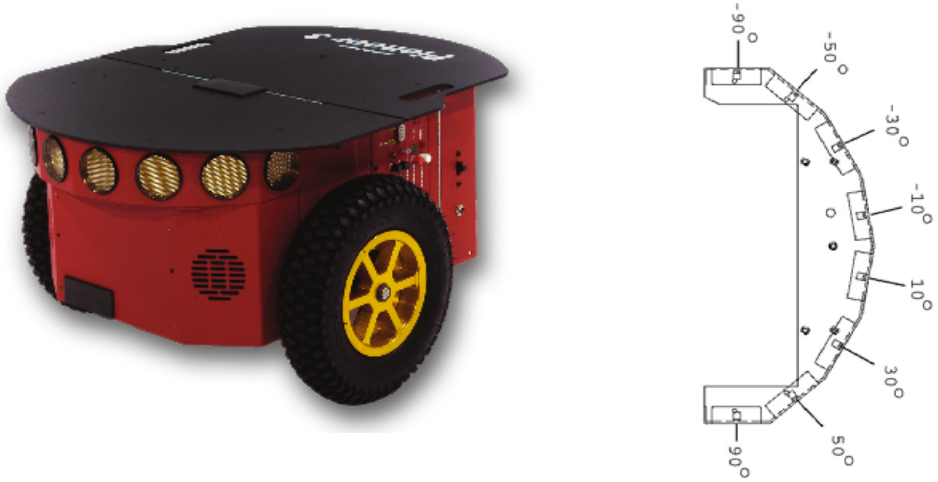

Fig. 5.1: P3-DX robotic platform with eight ultrasonic transducers (180° coverage).

Furthermore, the eight ultrasonic sensors are implemented to cover 180-degree with a 15-degree individual beamwidth [49]. The ultrasonic sensor generates a waveform that has a fixed frequency of 50 kHz and a pulse reputation frequency (PRF) of 3 Hz. This results in a built-in limit for minimum detectable range of 15 cm and a maximum detectable range of 5 m. Using the ultrasonic sensors with minimal capabilities will limit the understanding of echoic flow and its applications in research. Therefore, an acoustic radar is developed, in section 5.2, to provide more freedom and reliability in generating an acoustic waveform.

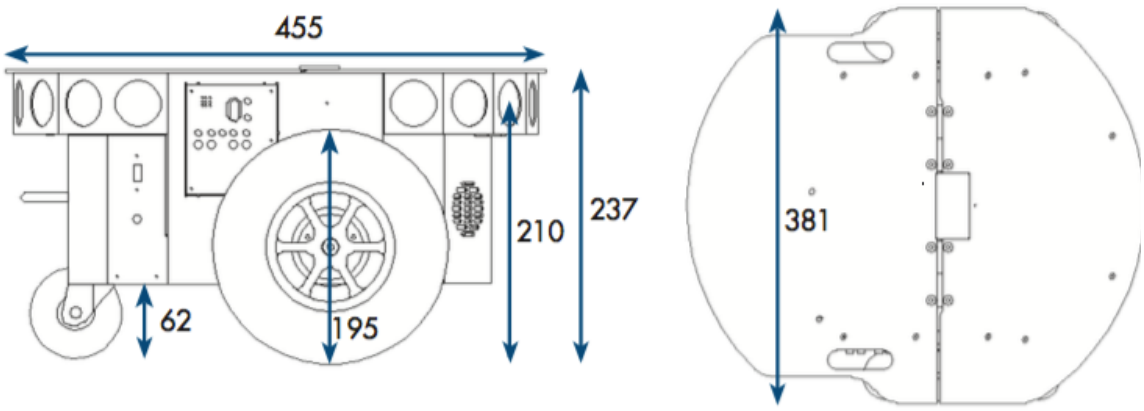

Fig. 5.2: Physical dimensions of a P3-DX robot in mm.

Fig. 5.2 illustrates the physical dimensions of the robot and deck. The robotic platform has a length of 455 mm, and a full width of 381 mm. The height of the robot's deck is 237 mm from the ground, while the lower side is only 62 mm from ground. These dimensions are sufficient for lab environment use and can be shown sufficient to carry an acoustic radar in section 5.2.2.

5.2 Acoustic Radar

A complete real time acoustic radar system has been developed and integrated to purposely use as a perception end of the echoic flow application experiments. In this section, a detailed explanation of the specifications, integration and, design of the acoustic radar is presented.

5.2.1 Acoustic Radar Integration and Specifications

To develop an acoustic radar, four ultrasound microphones and four ultrasound speakers were purchased through Avisoft Bioacoustics [50]. Each microphone comes with an individual amplifier; and one four-channel amplifier for the speakers. The microphone (receiver) has a frequency range of 10 kHz - 200 kHz, and a maximum amplification of 24 dB. Furthermore, the speakers (transmitter) have a frequency range of 25 kHz – 200 kHz. Also, the four-channel amplifier operates at a frequency range of 1 kHz – 180 kHz and provides volume control and overload indicators.

To generate a waveform through the sensors, we used National Instruments Compact Rio imbedded system [51]. The cRIO, as it is usually called, is a compact system that has a real time processor and an FPGA board. The FPGA board connects the real time processor to the input/output modules. First, a digital to analog converter (DAC) that connects the FPGA board to the ultrasound speakers through the power amplifier. The DAC has four analog output channels with a maximum sampling frequency of 100 kHz when using all channels; and can go up to 333 kHz if only one channel is in use. It also has a 16-bit resolution with a $\pm 10\ v$ voltage range. The second module is an analog to digital converter (ADC) that connects the received ultrasound microphone signal to the FPGA. It also has four analog input channels and a maximum sampling frequency of 500 kHz regardless of the number of channels used. This module provides 16-bit resolution with a $\pm 10\ v$ voltage range.

To program the system, NI LabView software is used due to its compatibility with cRIO. Three individual programs were developed with the use of, LabView, LabView Real Time and LabView FPGA to program in the operating system, the real time processor and the FPGA board. Generating a waveform is done in the real time processor, where we could choose from different waveform types such as sine, square, triangle, saw or, chirp. Also, it provides the ability to change frequency, bandwidth, pulse width, PRF and sampling frequency of each waveform. Additionally, for power consumption, the entire acoustic radar is powered by using a 24v SLA battery.

Table 5.1 shows the components of the acoustic radar system, while Table 5.2 shows the power supply and consumption required to power the acoustic radar. However, Table 5.3 indicates the components required to power the acoustic radar.

Table 5.1: Acoustic Radar Components

Component	**Provider**
Compact RIO: Including Real-Time processor, FPGA board and ADC/DCA modules.	National Instruments
Ultrasound power amplifier	Avisoft
Ultrasound loudspeaker	Avisoft
Ultrasound microphone	Avisoft
Windows operated laptop	Dell

Table 5.2: Power Supply and Consumption of the Acoustic Radar

Component	**Power source**	**Power Consumption**
Compact RIO	Connects directly to a battery via wire cable	Has a maximum power of 75 w at 9 - 30 v
Real-Time processor **FPGA board** **ADC/DCA modules**	all powered through cRIO	-
Ultrasound Power Amplifier	Connects to a battery via wire cable with a “NC4FX 4 pole female cable connector”	Has a maximum power of 72 w at 36 v when using all four channels
Ultrasound Loudspeaker	Powered via the Ultrasound power amplifier	-
Ultrasound Microphone	powered via a 5 v USB connector USB connector is connected to the cRIO	-
Microphone Preamplifier and Anti-aliasing Filter.	All powered through Ultrasound Microphone	-
Windows operated laptop	Has a rechargeable battery	run time of 5-7 hours

Therefore, a battery of 147 w or higher is sufficient to power the Acoustic Radar. Also, an NC4FX 4 pole female cable connector is used to connect the power amplifier to the battery.

Table 5.3: Components required to Power the Acoustic Radar

Component	**Description**	**Name**	**Provider**
24 v Battery	One (SLA) 24 v battery with 240 w power	Powerizer LiFePO4 Battery: 24V 10Ah	BatterySpace
Battery Charger For 24 v	An AC power charger to charge the 24 v SLA battery	Smart Charger (6.0A) for 25.6V LiFePO4 Battery Pack	BatterySpace
SLR connector	A power connector that connects the Amplifier to the power supply battery	NC4FX 4-Pole Female Cable Connector with Nickel Housing and Silver Contacts	Amazon

The entire components of the acoustic radar are then connected and mounted on top of the robotic platform by designing and building a frame presented in the next section.

5.2.2 Acoustic Radar Frame

In order to mount the acoustic radar on top of the robotic vehicle resulting in a portable acoustic radar testbed, a frame structure had to be designed and built. Therefore, the size and weight characteristics of the testbed components had to be considered before designing the frame. Below are the size and weight characteristics of the experimental testbed components.

Table 5.4: Size and Weight Characteristics of Experimental Testbed

Component	**Aspect**	**Value**
Compact RIO	Length	403.7 mm
	Width	87.1 mm
	Height	121.9 mm
	Weight	3.1 kilogram
Ultrasound Power Amplifier	Length	200 mm
	Width	176 mm
	Height	55 mm
	Weight	1.3 kilogram
Ultrasound Loudspeaker	Diameter	36 mm
	Length	60 mm
	Weight	65 grams
Ultrasound Microphone	Diameter	36 mm
	Length	60 mm
	Weight	150 grams

Windows Operated Laptop	Length	350.8 mm
	Width	261.9 mm
	Height	36.5 mm
	Weight	2.51 kilogram
P3-DX Robotic Platform	Length	445 mm
	Width	393 mm
	Height	237 mm
	Weight	9 kilograms
24 v Battery	Length	166 mm
	Width	76 mm
	Height	181 mm
	Weight	2.59 kilogram

The Acoustic Radar components that I mounted on the robotic platform are: cRIO, Amplifier, Loudspeaker, Microphone, Laptop and battery. For one 24 v battery, total weight of Acoustic Radar:

$$3.1 + 1.3 + 0.065 + 0.150 + 2.51 + 2.59 = 9.815 \text{ Kg}$$

According to the robotic platform manual [52], The P3-DX can hold between 17 and 25 Kg of equipment on top of its deck. To ensure that the existing robotic platform can function properly while carrying more than 10 Kg of equipment prior to mounting the acoustic radar components and frame, a test was made with a 17 Kg plywood cargo that is placed on top of the robot's deck to mimic the acoustic radar equipment, and the robot moved normally with no effect on speed or rotation.

To mount the acoustic radar on top of the P3-DX, a design was made by considering the size and weight of each radar component to achieve balance and stability, and to

minimize the possibility of equipment damage. Refer back to Fig. 5.2 for the physical dimensions of the robot and deck.

The portable acoustic radar design consists of a two level structure. The first level holds the compact RIO, power amplifier, battery, loudspeaker and microphone as shown in Fig. 5.3. While the second level holds the windows operated laptop.

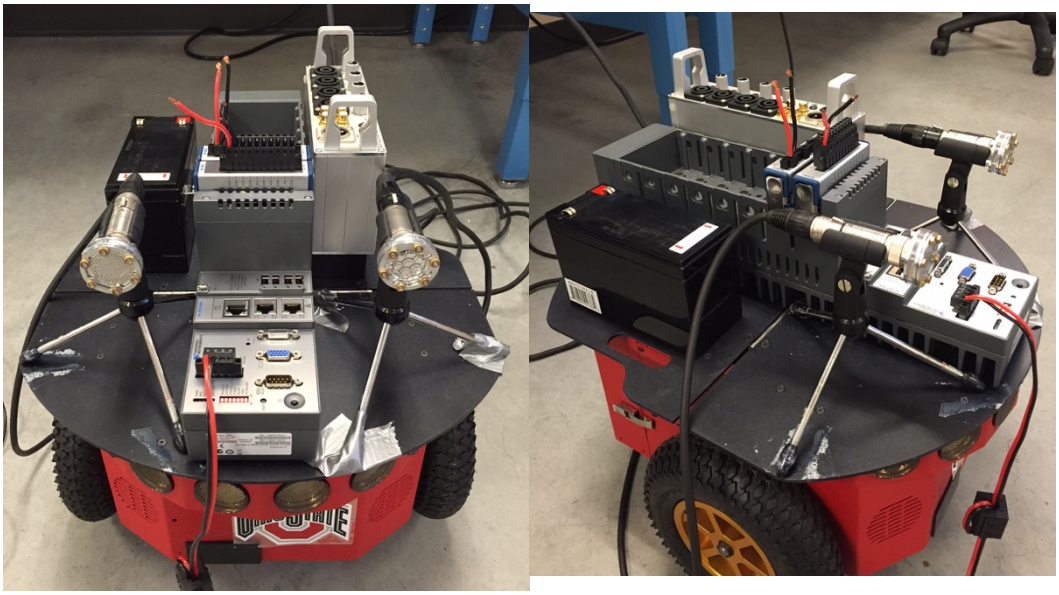

Fig. 5.3: First level of portable acoustic radar equipment setup.

The setup in Fig. 5.3 was arranged to help equalize the weight of the acoustic radar components on the robotic platform deck. Also, locating the amplifier, the battery and most of the cRIO's body in the center and back section of the deck supports the weight on the back and side wheels, and minimizes clutter when operating the acoustic radar.

The first level top and front view is shown in Fig. 5.4. For the front view, three sections are designed to hold, from left to right, the battery, cRIO and amplifier. The height of the section barrier was set to 15 cm, to allow wiring and to help with ventilation. While, the backside of the design is left open to allow equipment placing.

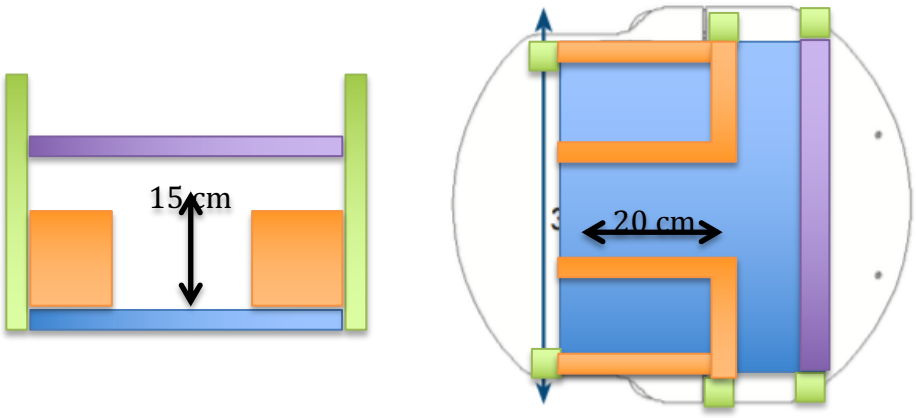

Fig. 5.4: Front view and first level top view of portable acoustic radar frame.

The blue panel is a Clear Polycarbonate panel that has the dimensions of 28 cm by 33 cm and has three evenly spaced units. Each unit is 20 cm in depth and 15 cm high (Orange). The blue panel is held by four T-slot bars and the horizontal bars are connected to the robot through the two holes shown in Fig. 5.2. The green shapes represent the T-slot bars that hold the second level and the purple T-slot bar. All green bars are 30 cm in length.

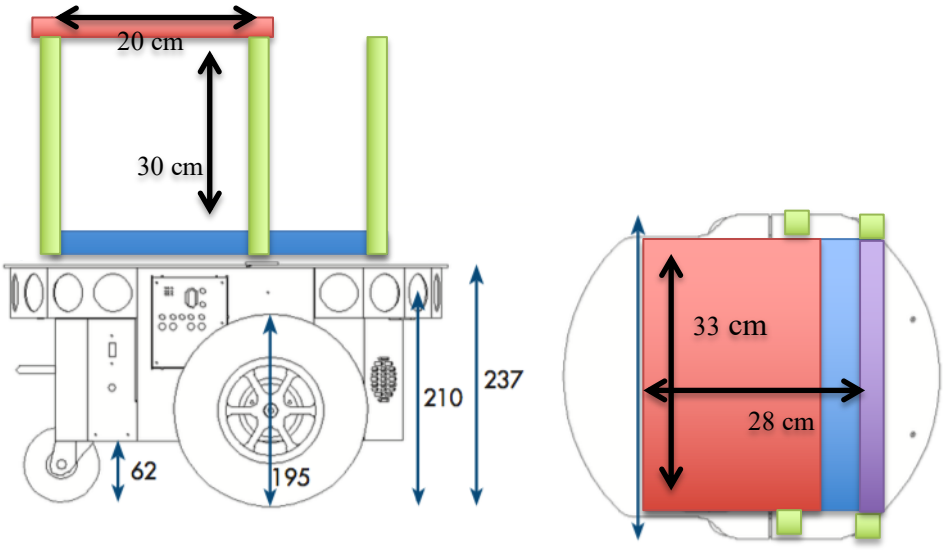

Fig. 5.5: Side view and second level top view of portable acoustic radar frame.

Fig. 5.5 shows the side and top view of the two level set. The second level (red) is also made of Clear Polycarbonate panel and has the dimensions of 20 cm by 33 cm. It is also held by four T-slot bars that connects to the green bars. Furthermore, the purple bar is a T-bar that can be moved up and down along the green T-bars and it will hold the sensors. Therefore, the sensors will be mounted on the T-bar and move freely across it when in need to change their location.

The acoustic radar frame was manufactured using 80/20 parts bought through Voelker Controls Company [53]. 80/20 is mainly a T-slot aluminum building system that consists of different series based on shape, size and functionality. The T-slot aluminum profiles are easy to assemble and reassemble to help with different designs. Also, aluminum is strong, resilient and lightweight, which provides a high strength to weight ratio.

For the acoustic radar platform design using 80/20, three major factors are taking into place, lightweight, small size and high durability. Therefore, a 25 mm or 1inch (0.002 lbs./mm) T-slot bar size is chosen to build the frame. Furthermore, Polycarbonate plate with 6 mm thickness is selected for withstanding the equipment. There are three main plastic panel materials that vary in strength, durability, weight and, thickness. Alumalite is the most lightweight (0.625 lbs./SQFT), however, it is less durable. Acrylic, on the other hand, is twice the Alumalite weight (1.45 Ibs/SQFT), yet more durable. Finally, Polycarbonate has almost the same weight as Acrylic (1.5 lbs./SQFT) but is two hundred times stronger than glass and thirty times stronger than acrylic [53]. Both Anchor and Standard End Fasteners are included in the design to allow fixed and moving T-slot bars. Fig. 5.6 represents the final three dimensional design proposed.

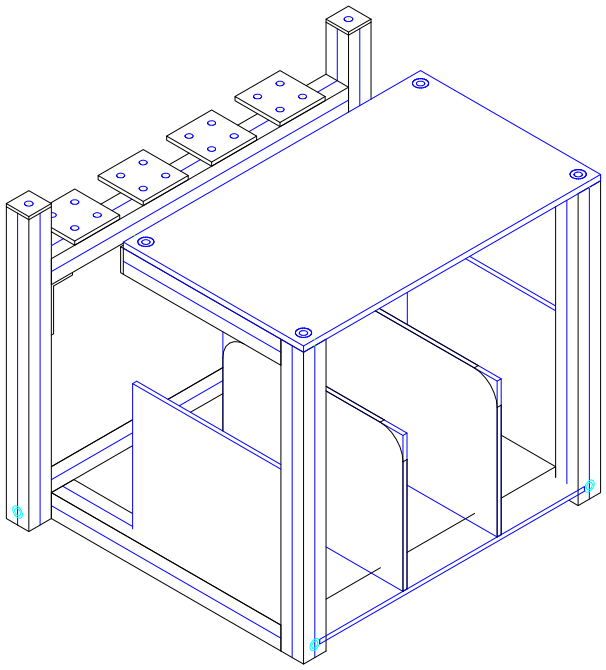

Fig. 5.6: Thee Dimensional view of the acoustic radar final frame design.

Figure 5.7 illustrates a top view of the exact acoustic radar frame design with both lower and top levels present. Note that all measurements are in millimeters.

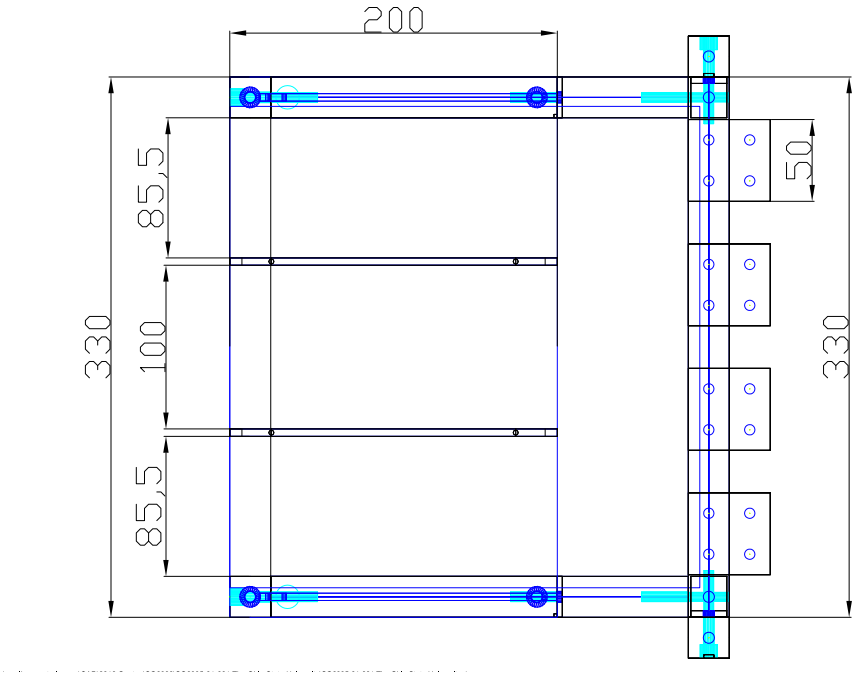

Fig. 5.7: Top view of the acoustic radar final frame design.

This design will contain a 25 mm T-slot bar containing four vertical bars of length 28 cm, one horizontal bar of length 28 cm, three horizontal bars of length 25 cm and two horizontal bars of length 20 cm. This will accumulate to a length of

$$28 \times 5 + 25 \times 3 + 20 \times 2 = 255 \text{ cm}$$

which weighs 5.1 lbs. For the plates, we have one lower level plate, one upper level plate and four side plates

$$28 \times 33 + 20 \times 33 \ + (4 \times 20 \times 15) = 2784 \text{ cm}^2$$

resulting in the plates weighing a sum of 3 lbs. Therefore, the final platform design is weighting about 8.1 lbs. or 3.675 Kg. Along with the acoustic radar weight of 9.815 Kg, calculated in the previous section, the full weight of the acoustic radar and frame mounted on top of the robotic platform equals 13.49 Kg, which is lower than the 17 Kg lower limit that the robotic platform could hold [52].

Finally, by having the acoustic radar portable and connected to a controllable robotic platform, several experimental setups can be performed, and the system can be tested in different environments. This design helped expand the research to cover new areas of interest.

5.3 Experimental Testbed Integration

The experimental testbed consists of the robotic platform presented in section 5.1 and the acoustic radar presented in section 5.2 combined. The acoustic radar is considered to be the perception side of the testbed, while the robotic platform is the motor action end. Therefore, an integration between the acoustic radar and the robotic platform will be explained.

The block diagram of the acoustic radar experimental testbed is shown in Fig. 5.8.b. The robot's deck holds the acoustic radar, which consists of the NI compact RIO, transmitter, receiver, input amplifier, output amplifier, power battery, and laptop. The system was integrated such that the real time controller of the cRIO processes in real time a transmitted waveform. The waveform is then sent to the programmable FPGA board which is responsible for synchronizing the transmit signal with the DAC that hands the

signal to the transmitter. The signal is then amplified and transmitted through an ultrasound loudspeaker.

After the signal is reflected back to the radar, the microphone receives the echoed signal which is then amplified before being converted to a digital signal through the DAC. The received signal is then synchronized through the FPGA clock and sent in real time to the real-time controller for processing. Both range and Doppler, along with the corresponding echoic flow for each target is then determined and sent from the cRIO's real-time processor using real-time LabView software to the Windows LabView software through Ethernet.

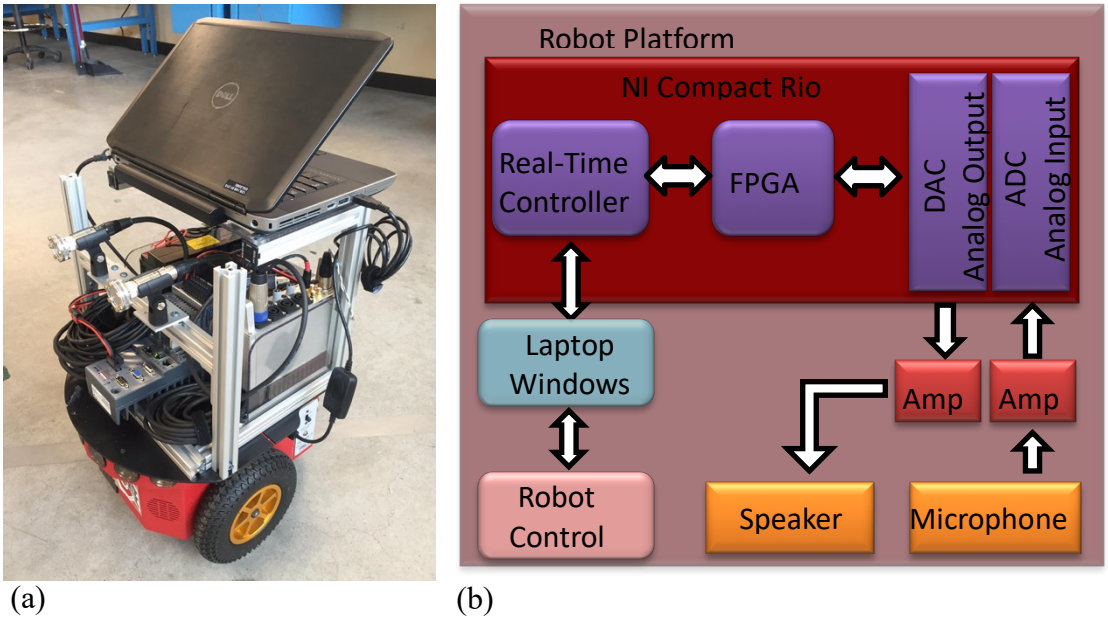

(a) (b)

Fig. 5.8: (a) Experimental Acoustic Radar Platform and (b) Block Diagram.

The Windows LabView software serves as a medium to transfer data between the real-time processor and the MATLAB robot controlling software. Therefore, the output of the Windows LabView is transferred through a TCP/IP (Transmission Control

Protocol/Internet Protocol) interface. This interface allows a real-time transfer of data between LabView and MATLAB. When echoic flow data along with time stamps and other related data is received in MATLAB, the information is then used to process the echoic flow guidance approach and determine a control decision output.

The output of MATLAB, processed in real-time, to the robotic platform are movement instructions. The instructions contain two outputs, a forward velocity request and a rotational velocity request. Both values are carried through a USB to serial adapter that connects the Windows Laptop to the robot's controller. The entire process is repeated in real time every pulse repetition interval (PRI), which represents a full perception action cycle.

5.4 Acoustic Radar Testing

The testing of the acoustic radar was performed to indicate the performance of the measurements determined by the system when engaging in experimental applications, especially when determining the echoic flow output. In this section, a series of tests are performed to understand the acoustic radar output.

5.4.1 Range Testing

For range testing, three main characteristics were taken into account. The range measurement's accuracy, precision and resolution. For accuracy, we measure how far is the measured range from the actual target location. Therefore, and to determine the accuracy of the range measured, a no target scenario was assumed. Here, the output of the

acoustic radar system is connected directly to the input of the radar system. The output signal is an LFM waveform with 5 kHz bandwidth. In an Ideal situation, the range profile should yield a sinc function with the mainlobe around zero range, due to connecting the input to the output.

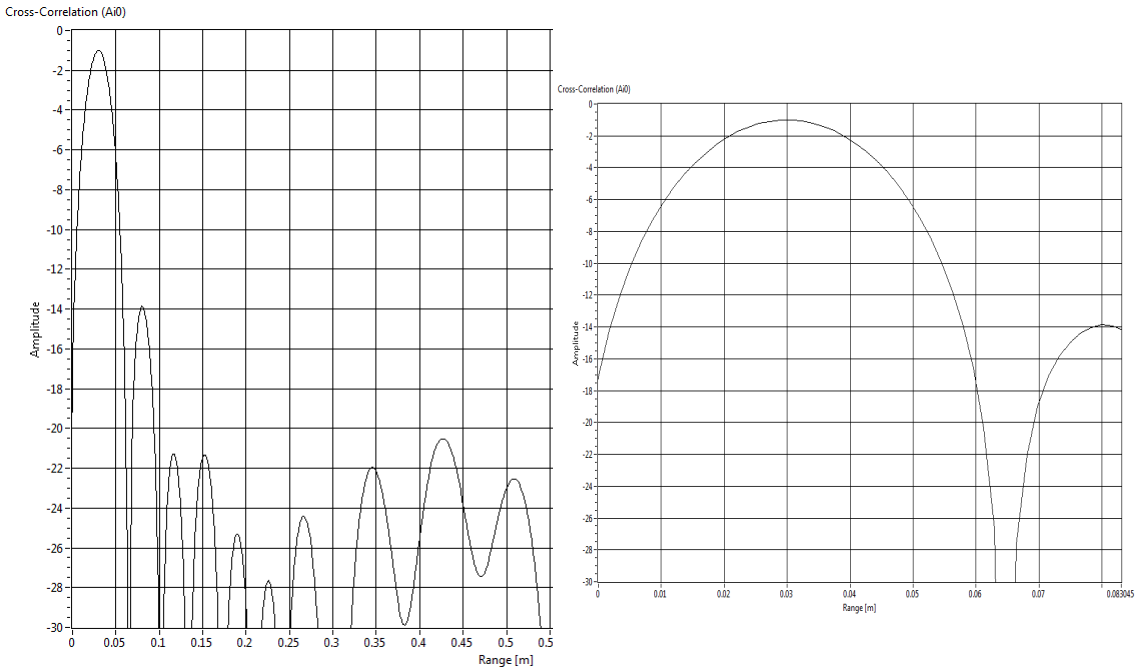

Fig. 5.9: Range Profile of the input connected to the output of the acoustic radar.

However, from Fig. 5.9, the mainlobe is shown to be shifted 3 cm in range, with the sidelobes being 13 dB lower than the mainlobe. The 3 cm constant shift across any range measurement is caused by the internal system's signal delay, and therefore, any range output will be subtracted 3 cm. Hence, the range accuracy is fixed by a 3 cm shift.

While, for examining the range resolution of the acoustic radar, a single target was placed 1.02 m away from the radar. The bandwidth of the LFM was set at 5 kHz, which

from (3.7) yields a range resolution, or a minimum distance required to distinguish between two targets at $\Delta R = 0.034\ m$. The range profile in Fig. 5.10.a shows a mainlobe at 1.02 m, and the side lobes are 14 dB lower than the mainlobe. The 3.9 dB beamwidth of the mainlobe is measured to be about 0.035 m. Which is very close to the theoretical calculated of 0.034 m.

(a)

(b)

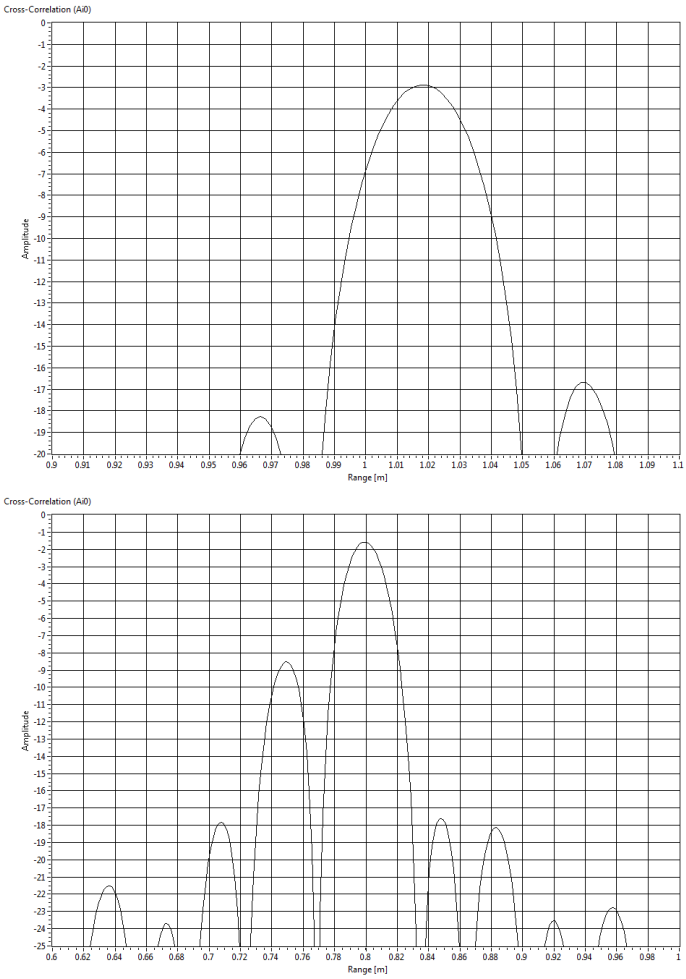

Fig. 5.10: (a) Range Profile of single target at 1.02 m. (b) Range profile of two targets at 0.75 m and 0.8 m.

Furthermore, two targets were placed at 0.75 m and 0.8 m away from the radar. Fig. 5.10.b shows the range profile of the output of the acoustic radar. It is apparent that two distinguishable targets are presented in the range profile at 0.75 m and at 0.8 m, which indicates that the acoustic radar system was able to resolve two adjacent targets who are only 5 cm apart.

While, when using two transmitters and two loudspeakers to work as two independent monostatic radar systems for the sake of undertaking the guidance experiments in both chapter 7 and chapter 8, a test was made to determine the steadiness of the range output from each sensor at different range steps. Here the output of the radar system is a frequency modulated continuous wave with a bandwidth of 23 kHz and a 5 Hz modulation frequency.

Two one-meter width targets were placed in front of the left and right sensor. The left and right sensors are rotated 45^{o} to the left and to the right with respect to the robot's forward direction respectively. Each sensor is measuring the range to the target for one minute, with an update every second. The ranges from 300 mm to 1000 mm with an increment of 100 mm are shown in Fig. 5.11.

(a)

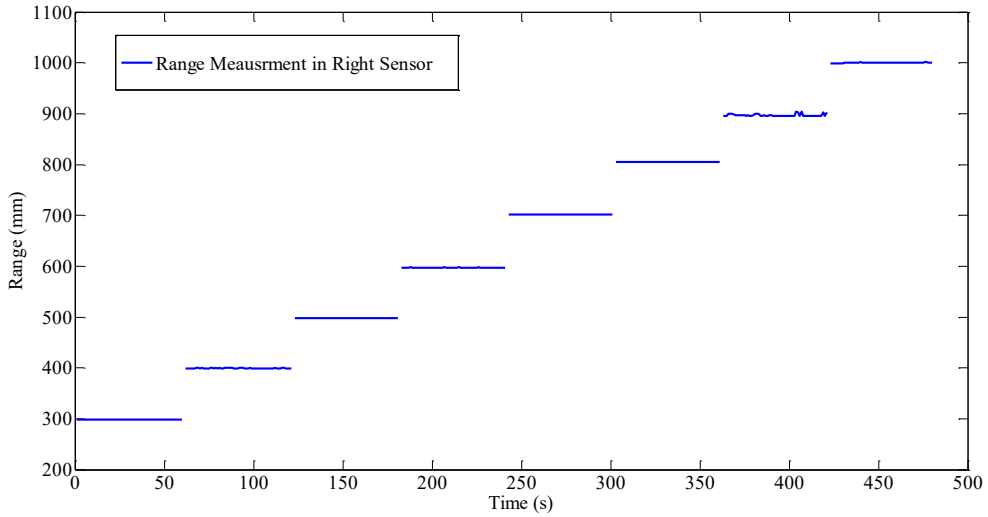

(b)

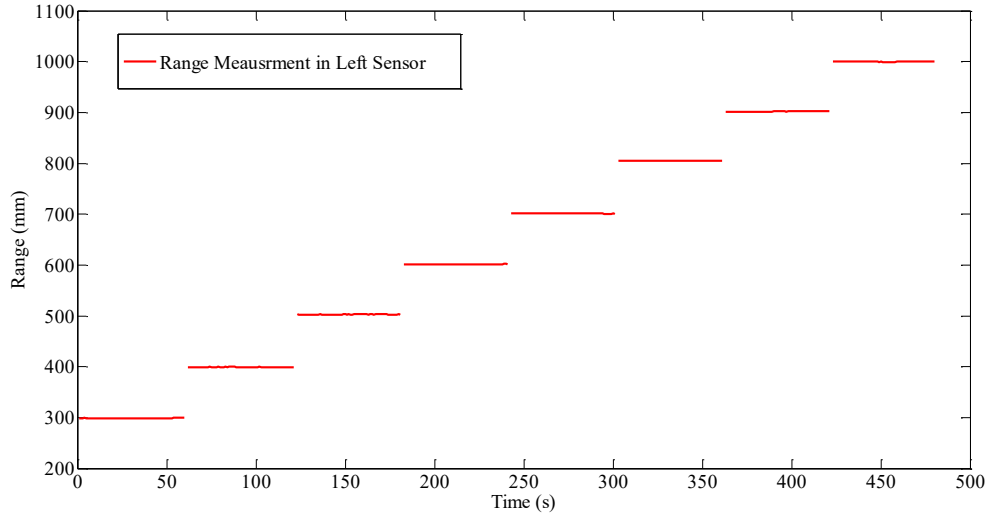

Fig. 5.11: (a) Range measurement from right side sensor. (b) Range measurement from left side sensor.

The output from both Fig. 5.11.a and Fig 5.11.b displays the range measured to a target that was placed in eight different locations. Starting from the closest location 0.3 m away from the radar, to one meter away from the radar. Given that the two sensors were active

at the same time, it is presented that there was no interference between the two sensors when perceiving two individual targets independently. This is very crucial in using the same system when guiding the acoustic radar platform through different environments presented in chapter 7 and chapter 8. Also, the precision of the acoustic radar was tested, and the output yielded a very precise range measurement across the eight different locations and only minimal variation in the right side sensor when measuring a target that is 0.9 m away. Although, the remainder of the experimental test has a fine range precision measurement that is less than 1 mm. For a better quantification of the results, Table 5.5 shows the standard deviation of each individual range step, where every step is measured 60 times.

Table 5.5: Standard deviation of range measurement to target

Range	**Left Sensor Standard Deviation**	**Right Sensor Standard Deviation**
300 mm	0.1371 mm	0.0724 mm
400 mm	0.1371 mm	0.2532 mm
500 mm	0.2199 mm	0 mm
600 mm	0.0548 mm	0.1014 mm
700 mm	0.4570 mm	0.1513 mm
800 mm	0.2145 mm	0.1130 mm
900 mm	0.8341 mm	2.3034 mm
1000 mm	0.4498 mm	0.3336 mm

To test the range measurement for far range targets, the previous test was replicated to cover the range from 0.5 m to 3.5 m from the radar, with a half a meter increment. The output of the right sensor is shown in Fig. 5.12, and the results corresponds with a high precision radar measurement across the span of three meters, and show that the acoustic radar is capable of measuring targets that are 3.5 m away with high precision.

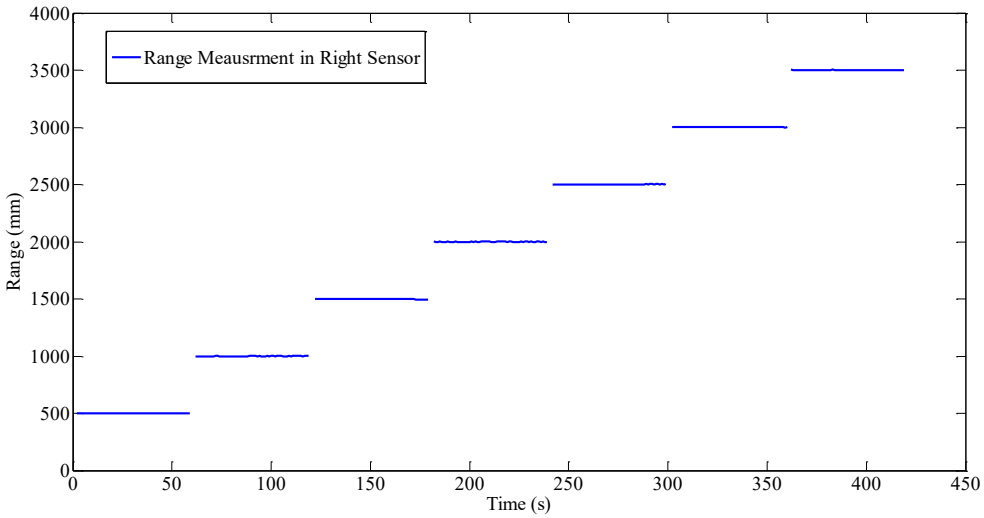

Fig. 5.12: Range measurement from right side sensor for far range.

Table 5.6 shows the standard deviation of each individual range step, where every step is measured 60 times.

Table 5.6: Standard deviation of range measurement to target

Range	**Right Sensor** **Standard Deviation**
0.5 m	0.1674 mm

1 m	0.7807 mm
1.5 m	0.6279 mm
2 m	0.3230 mm
2.5 m	0.9025 mm
3 m	0.9942 mm
3.5 m	1.1140 mm

The output of Table 5.6 agrees with the observation that even for far range targets, the range measurement is considered with high precision.

5.4.2 Echoic Flow Testing

The use of a triangular FMCW waveform provides both range and Doppler velocity from the radar output, and hence, echoic flow. Here the radar Doppler measurement and the echoic flow associated with range and Doppler velocity measurements will be tested and presented.

To analyze the Doppler velocity, a stationary 1 m width panel target was placed at the maximum range of 3.4 m away from the target. The maximum range is based on the equation of (3.18) for a triangular FMCW, and a minimum overlap of %80 between the transmit and receive waveforms. Here, the acoustic radar testbed traveled towards the target with a 100 mm/s preset constant velocity. Fig 5.13 shows the Doppler velocity measurement across the time stamp of each pulse. Note that the modulation period is set to 0.2 s, resulting in five updates per second.

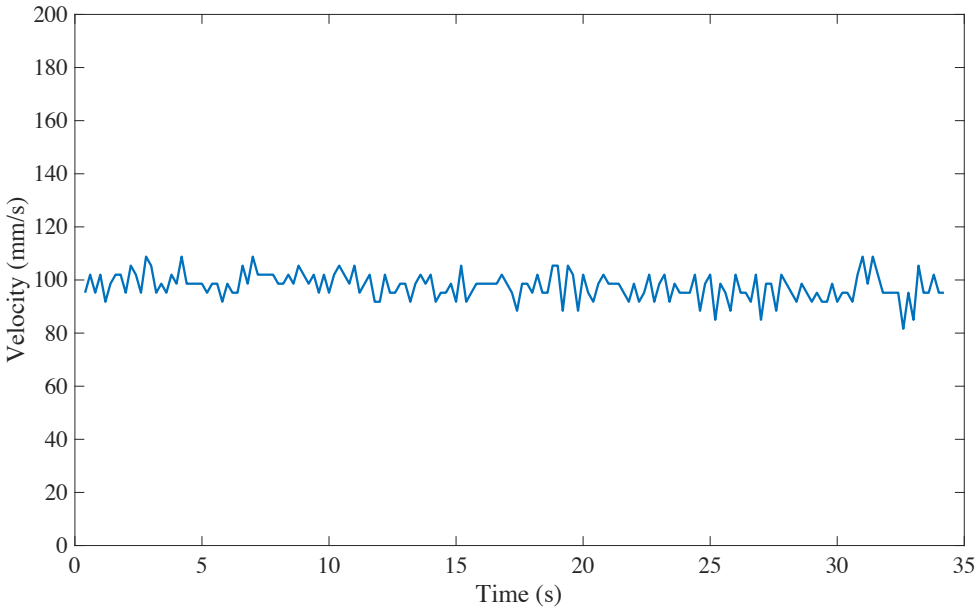

Fig. 5.13: Velocity measurement of the platform moving at 100 mm/s.

The velocity measurement of the acoustic radar testbed shown in Fig. 5.13 fluctuates around the 100 mm/s set velocity. The histogram of the test is shown in Fig. 5.14, with the mean and standard deviation presented.

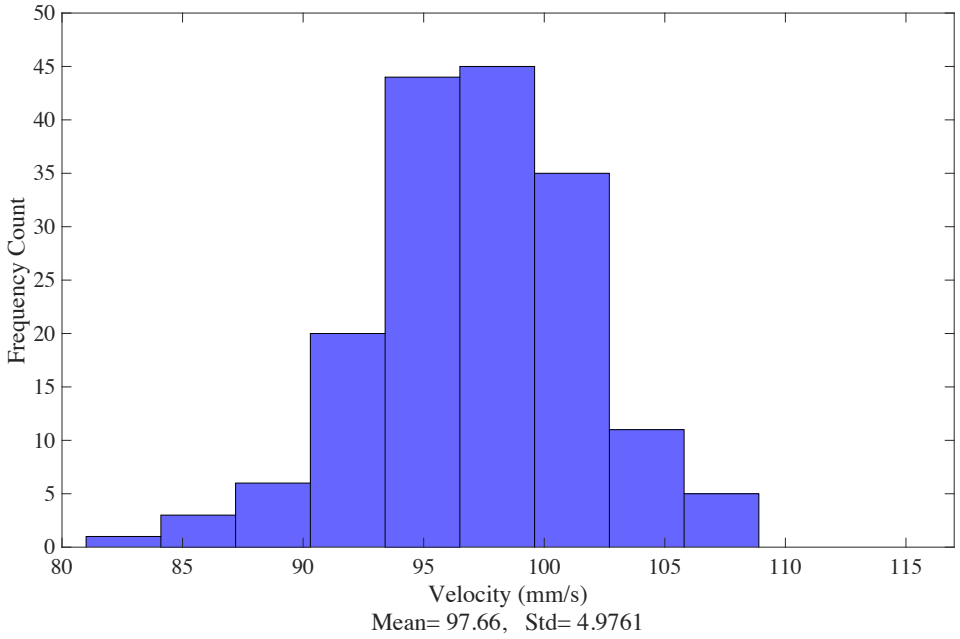

Fig. 5.14: Histogram of the velocity measurement when moving at 100 mm/s.

From the histogram of Fig. 5.14, the mean of the Doppler velocity is equal to 97.66 mm/s which is about 2 mm/s below the actual velocity of the platform, while the standard deviation, or the precision of the Doppler velocity is less than 5 mm/s. Regardless of the signal's low frequency, the Doppler velocity had a good precision and accuracy measurement across the entire test.

However, when the target is parallel to the direction of the testbed's movement, which resembles the experiment work done in chapter 7 and chapter 8 when the radar sensor is set to be $\pm 45°$ from the forward direction, the range and velocity measurements are now a function of the angle to the target θ, and hence, the echoic flow will also vary through the experiment. Since the echoic flow parameter is a function of range over Doppler velocity (4.2), we can rewrite the equation as a function or projected velocity as shown.

$$\tau_r(t) = -\frac{r(t)}{v(t)\ \cos(\theta)} \tag{5.1}$$

where v is the forward velocity, and θ is the angle between the testbed's forward velocity and the target. Also, the projection of the distance between the acoustic radar testbed and the parallel target onto the $x\ axis$ can be determined as $x = r(t)\ \sin(\theta)$. Hence, substituting in (5.1)

$$\tau_r(t) = -\frac{x}{v(t)\ \cos(\theta)\ \sin(\theta)} \tag{5.2}$$

while $\cos(\theta)\ \sin(\theta) = {}^{1}/_{2}\ \sin(2\theta)$, Echoic flow estimate can be written as a function of forward velocity v, perpendicular distance to the target x, and, projection angle θ.

$$\tau_r(t) = -\frac{2x}{v(t)\ \sin(2\theta)} \tag{5.3}$$

Assuming a varying projection angle $\theta = (0° - 90°)$ setting the perpendicular distance to the target $x = 1\ m$, and the forward velocity $v = 0.1\ m$. Fig 5. 15 Shows the echoic flow curve vs angle to parallel target when using Doppler velocity.

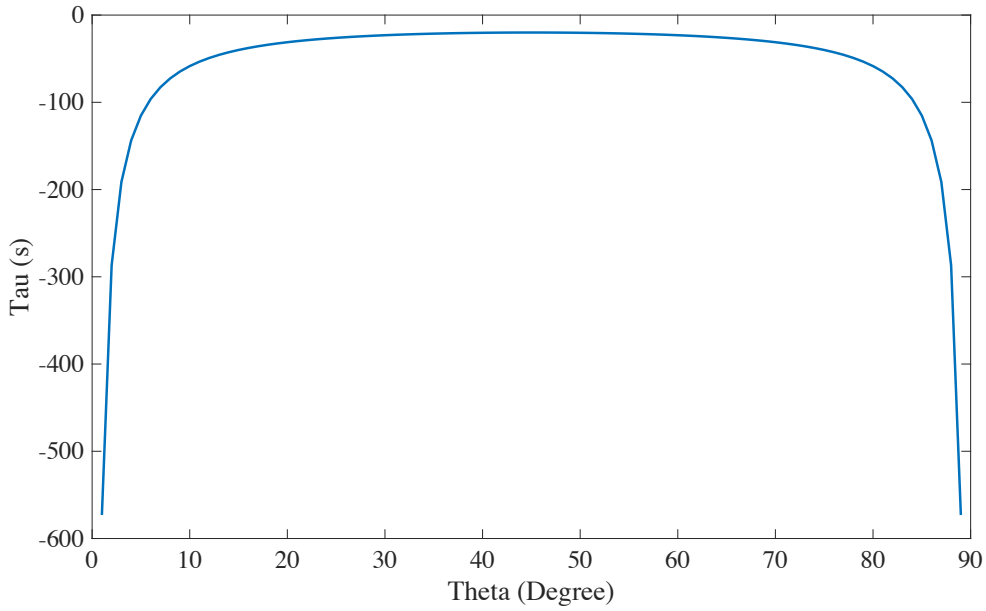

Fig. 5.15: Echoic flow estimate of a parallel target vs angle to the target.

From Fig 5.15, when the target is far away, thus the angle to the target is near zero, then range is near infinity while Doppler is near maximum Doppler, resulting in infinite tau. By moving towards the parallel target, the angle to the target increases, this will decrease the range measurement and decrease the Doppler velocity which will decrease time to contact. Minimum time to contact is presented at angle 45^{o}. Where after that, range to target is decreasing and Doppler velocity also is decreasing, which outcomes in a minimum range at 90^{o} and zero Doppler, resulting in infinite echoic flow, and hence passing the parallel target.

Therefore, an experiment is done by moving the radar testbed across a straight corridor with vertical poles set to the side. The poles are set to be 20 cm away from each other,

while the radar testbed is placed one meter away from the parallel pole wall. Both Range and Doppler velocity return from each illuminated pole is measured as shown in Fig 5.16.

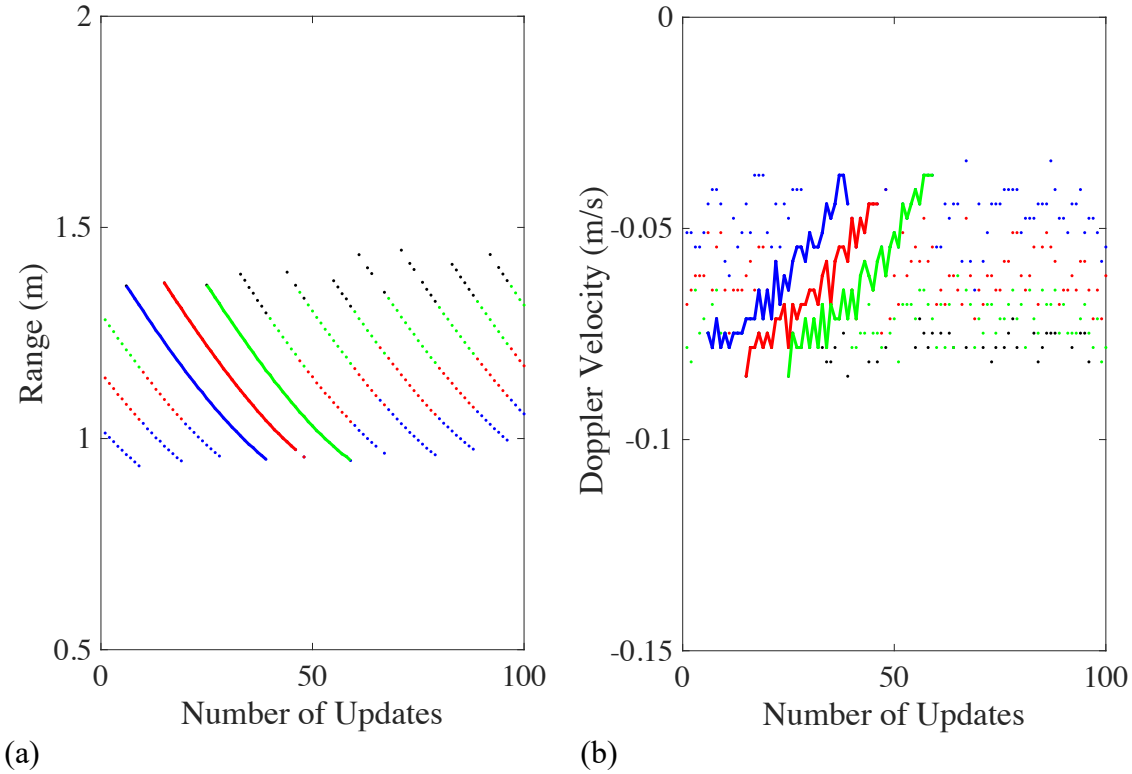

Fig. 5.16: (a) Range and (b) Velocity measurements of a parallel wall pole target.

In Fig 5.16, the colored points represent range and Doppler velocity measurements from each individual illuminated pole. By focusing on the range measurements in Fig. 5.16.a, the acoustic radar measures between three and four targets in each update. Where, the blue points represent the closest pole to the radar, then red is the second measured pole, while the green is the third measured pole, and the furthest measured pole is the black colored. When connecting the colored points, a representation of each individual measured pole can be viewed. The Radar perceives the first pole, colored in solid blue, at 1.36 m

away and continues the perception until the pole is less than 1 m away, where it is no longer in the radar's beam. The solid blue, green and red lines represents three individual poles.

The same concept is shown with Doppler velocity in Fig. 5.16.b. Where it is obvious that the furthest pole has the highest Doppler velocity return, due to the small projection angle. When the radar first perceives the pole, the Doppler velocity measurement is a little short of 80 mm/s. By moving forward, the angle to the target increases; hence, the Doppler velocity decreases until it reaches around 35 mm. Whilst, by taking each range measurement and dividing it by the corresponding Doppler velocity measurement, echoic flow is determined for each individual pole as shown in Fig. 5.17.

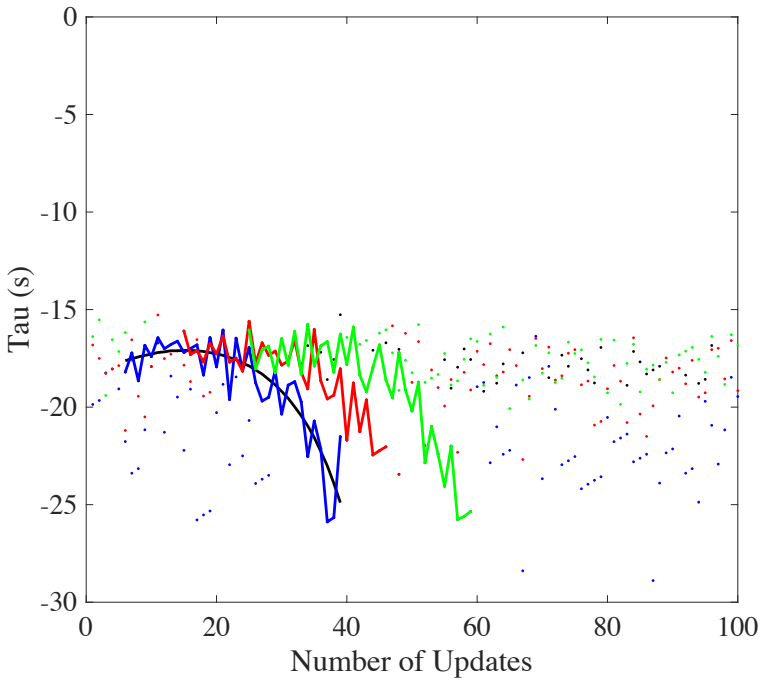

Fig. 5.17: Echoic flow measurements of a parallel wall pole target.

The equivalent tau output from moving parallel to the pole wall is presented in Fig. 5.17. When following the blue solid line, the furthest pole is perceived with a time to contact equaling $\tau = -18.2\, s$. By moving forward, the range and Doppler velocity decreases. Therefore, the echoic flow decreases until the angle to the pole reaches 45^{o}, resulting in the minimum time to contact at $\tau = -16\, s$. After that, while the angle to the pole target increases, the echoic flow also increases, resulting in a maximum echoic flow output of $\tau = -25.88\, s$. The black solid line, however, is a fitted line to the oscillatory blue echoic flow curve. And it can be shown following the theoretical curve of Fig. 5.15. Therefore, in both experiments of chapter 7 and chapter 8, the pole with the minimum echoic flow will be used in determining the minimum time to contact from each sensor, regardless of the closest distance or the highest Doppler velocity pole.

Chapter 6: Target Following and Approach

In this chapter, the use of the time derivative of the echoic flow, $\dot{\tau}$, will be examined in both simulation and experiment to guide a radar platform towards approaching and then following a target. That Target can be stationary or in motion. The guidance rule proposed will help close both range and range rate gaps at the same time.

6.1 Target Following and Approach Simulation

In this section, the use of the derivative of the echoic flow, $\dot{\tau}$, is used through simulation to test the ability of controlled braking and following a target in motion. The simulation presented will test a radar platform moving towards a target. The target can be stationary or in motion. The simulation is based on the theory presented in section 4.1.3.

The radar was assumed to be a pulsed, acoustic system with a LFM waveform that travels with the speed of sound. The low speed of propagation for acoustic waves leads to fine range resolution. The radar parameters are presented in Table 6.1, where the target range is measured by match filtering a time delayed echo of the transmitted chirp. The time delay corresponds to the target's location by using (3.1). The bandwidth of the acoustic radar was taken to be 23 kHz giving a 7.4 mm range resolution (3.7), the pulse width was

set to 24 ms, while the pulse repetition frequency (PRF) was set to 10 Hz and the noise level was set such that the SNR was 22 dB.

Table 6.1: Acoustic Radar Parameters

Parameter	**Value**
Bandwidth (B)	23 kHz
Pulse Width (τ)	24 ms
Pulse Repetition Frequency (PRF)	10 Hz
Speed of Propagation (c)	340 m/s
Signal to Noise Ratio (SNR)	22 dB

After detecting the range to the target, the relative velocity to the target will be determined by subtracting two consecutive pulses over time. Which provides the echoic flow measurement to the target using (4.3).

By obtaining relative velocity and echoic flow, the velocity of the radar testbed is updated by using the acceleration equation of (4.19). Note that, (4.19) requires a preset value of the echoic flow derivative $\dot{\tau}$ based on the braking strategy desired.

Based on the target's velocity, three motion scenarios are present. Stationary target, target velocity lower than radar velocity, and target velocity greater than radar velocity. Across all three scenarios, the radar platform is assumed in motion. Initial radar platform and target velocity and range locations are presented in Table 6.2.

Table 6.2: Initial range and velocity of radar platform and target

Simulation Scenario	**Initial Radar platform**		**Initial Target**		**Initial Relative**	
	Range	**Velocity**	**Range**	**Velocity**	**Range**	**Velocity**
(1) Stationary Target	0 m	2 m/s	3 m	0 m/s	3 m	2 m/s
(2) Target velocity lower than radar platform	0 m	5 m/s	3 m	3 m/s	3 m	2 m/s
(3) Target velocity greater than radar platform	0 m	5 m/s	3 m	6 m/s	3 m	1 m/s

For the first simulation set, the target was assumed stationary. The radar platform had an initial velocity of 2 m/s, and was 3 m away from the target. Nine different trials were conducted based on setting tau dot. Where, early, linear, and late braking strategies were conducted.

To illustrate the movement of the radar platform and the target in the simulation, an update of the location of the radar platform is presented when having $\dot{\tau}$ set to the early braking strategy of $\dot{\tau} = 0.3$, presented in Fig. 6.1.

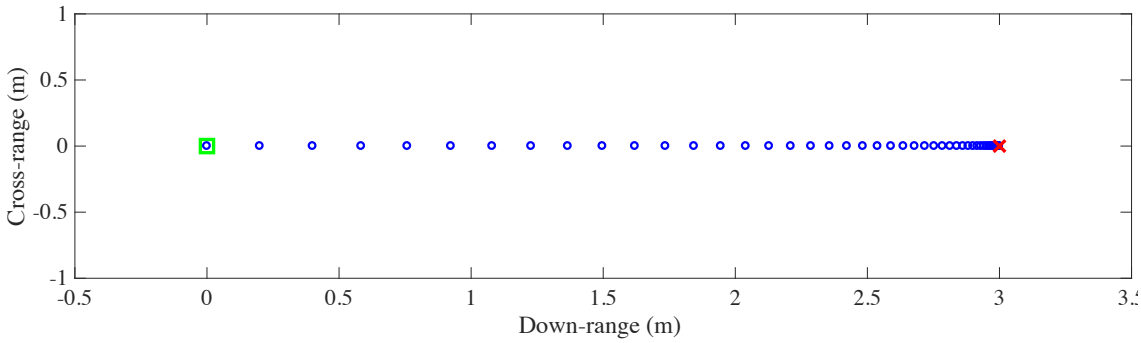

Fig. 6.1: A simulated radar platform moving towards a stationary target.

From Fig. 6.1, the radar platform started at point (0,0), illustrated as a green square, and moved towards the stationary target, represented by a red cross. The blue circles denote the movement of the radar platform towards the target. Each individual circle shows the location of the radar platform for each PRF update. Given that the PRF is set to 10 Hz, and the initial velocity of the radar platform is 2 m/s, the second radar platform location was at 0.2 m down-range. After that, the platform velocity decreases until it reaches zero velocity at the target. Closing both range and velocity gaps at the same time.

Range, velocity and, acceleration curves for the stationary case are presented in Fig 6.2. The three braking scenarios, explained in section 4.1.3, are simulated. It is apparent that the curves of Fig 6.2 are similar to the plots of the progression of range, velocity and, acceleration presented in Fig. 4.2, made by plotting the motion equation curves of (4.11), (4.14) and, (4.17). However, the curves exploited through simulation are varying, especially acceleration curves, due to the nature of the variation in range and velocity measurements of the acoustic radar.

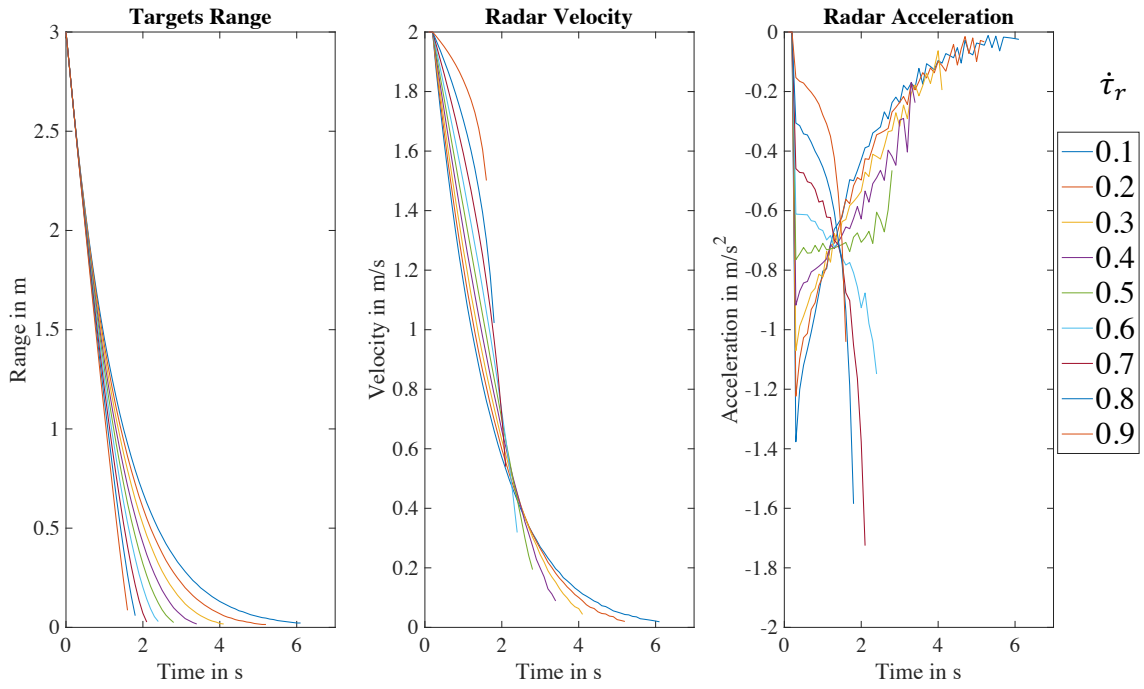

Fig. 6.2: Motion curves for simulation of radar reaching a stationary target.

When the target is moving, the range rate, $\dot{r}[n]$, estimated by the radar represents the relative velocity between the radar platform and the target. As a result, the echoic flow process will now be acting to close the relative range and velocity gaps between platform and target, i.e. the end conditions are when the radar platform has the same position and velocity as the target.

Fig. 6.3 shows how the platform's range, velocity and acceleration changed over time as it approached a slow moving target. The target velocity was fixed at 3 m/s while the radar platform had an initial 5 m/s velocity, and started 3 m behind the target.

The shapes of the curves, presented in Fig. 6.3, are the same as the case when the target is stationary, Fig. 6.2. Now however, the final velocity is the same as the target velocity. Hence, the relative, not absolute velocity is equal to zero, and the following approach is possible.

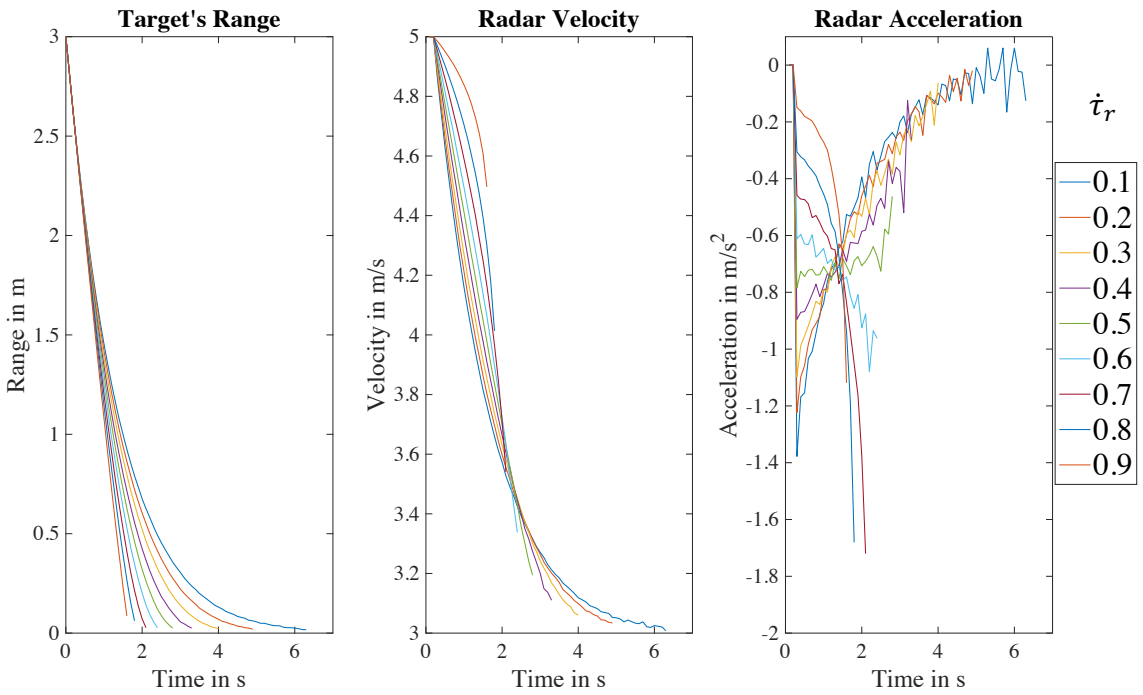

Fig. 6.3: Motion curves for simulation of radar reaching a slow moving target.

In the next set of simulations, the target moved with velocity of 6 m/s while the initial radar platform velocity was 5 m/s. The initial range between radar platform and target was set to 3 m. Furthermore, since the target velocity is greater than the radar velocity, the gap between the radar platform and the target will be opening. Hence, the echoic flow output will be positive. To ensure gap closer regardless of whether the gap is opening or closing,

the restrictions presented in (4.20) and (4.21) on echoic flow and velocity measurements will be enforced respectively. In this simulation, $\tau_{r\,max}$ was set to 3 s and $\dot{r}_{min}$ was set to 0.2 m/s.

Fig. 6.4 shows the curves for the progression of range, velocity and acceleration over time. Initially, the radar platform velocity increased exponentially when $|\tau_r| < \tau_{r\,max}$, then, when $|\tau_r| \geq \tau_{r\,max}$ it followed a linear tend, since $\tau_r = \tau_{r\,max}$ until the radar platform velocity exceeded the target's velocity, and the echoic flow measured is less than the maximum set, $|\tau_r| < \tau_{r\,max}$. Here, the scenario became then the same as when target velocity was less than radar velocity, and thus the range gap is closed, and platform velocity is matched with target velocity through the EF processing.

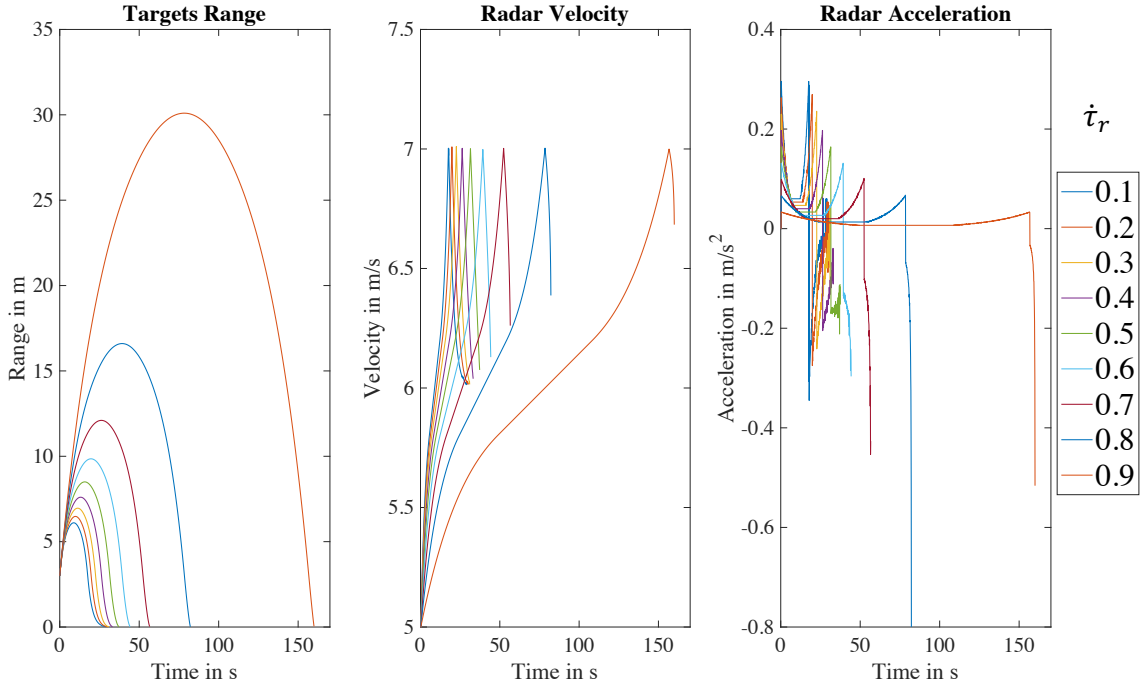

Fig. 6.4: Motion curves for simulation of radar reaching a fast moving target.

When $0 < \dot{\tau}_r < 0.5$ an early acceleration is followed by an early braking which results in a faster closer of the range and relative velocity gaps. However, when $0.5 < \dot{\tau}_r < 1$, a late acceleration is flowed by a late braking, and the gap closer time is increased.

In these simulations, degrading the range and range rate accuracy by having a low SNR also degraded the echoic flow measurement and resulted in variation of the acceleration curves. The degradation of τ_r was pronounced when the relative range rate was small. Methods to improve the range and range rate estimate accuracy, leading to a more accurate τ_r, are presented in section 6.2 that describes the experimental results.

6.2 Experimental Results

For the experimental tests, the acoustic radar system mounted on the Pioneer 3-DX robot was used. The output of the radar was a velocity request, calculated using the echoic flow theory described in section 4.1, that was given to the robot. Two acoustic radar processing methods were used to conduct the same set of experiments, a Linear Frequency Modulated pulse (LFM) waveform and a Triangular Frequency Modulated Continuous Waveform (FMCW). After the target was detected, the range and range rate were estimated, and the echoic flow calculated by using (4.3) for the pulsed radar and (4.5) for continuous wave radar. Equation (4.19) was used to calculate the required velocity for the robot.

6.2.1 Using Pulsed Radar

For the first set of experiments, A 1-by-0.5 m panel was set 3.5 m away from the robot platform, as shown in Fig. 6.5, to act as a target. The robot had an initial velocity of 0.15 m/s moving towards the target. Note that the radar platform was set to stop 15 cm before reaching the target, to eliminate the chance of collision.

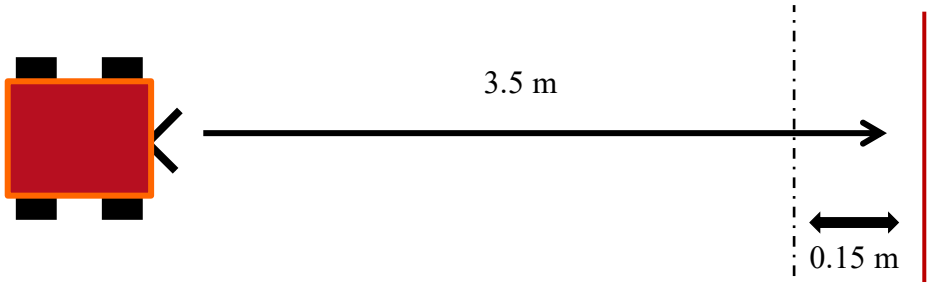

Fig. 6.5: A radar platform moving towards a stationary target.

Two trials were undertaken when setting $\dot{\tau}_r$ to 0.3. For the first trial, the radar generated an LFM waveform 40k-45kHz resulting in a 5KHz bandwidth, a 24 ms pulse width and a PRF of 10Hz. Table 6.3 presents the radar parameter of the two trials.

Table 6.3: Pulsed acoustic radar parameters

Parameter	**First Trial**	**Second Trial**
Bandwidth (B)	5 kHz	23 kHz
Center Frequency (f_o)	42.5 kHz	36.5 kHz
Pulse Width (τ)	24 ms	24 ms

Pulse Repetition Frequency (PRF)	10 Hz	10 Hz

An $\alpha\ \beta$ tracking filter is then applied in real time to smooth the range measurements. α was set to 0.1 to decrease range variation. β is then optimized by using (6.1) [54].

$$\beta = \frac{\alpha^2}{2 - \alpha} \tag{6.1}$$

Fig. 6.6.a shows two curves, the blue is the sequence of range measurements and red the smoothed range estimate obtained using the $\alpha\ \beta$ filter. The variation in the actual range measurements while the robot was moving towards the stationary target is apparent. Due to the motion of the platform, measured range shows variation of approximately 3 cm around the smoothed tracking filter estimate, which converged after five second in the experiment. The high range value present at 34 s was a result of a misdetection and its impact on the tracker is clear. However, the system recovered quickly

Both smoothed and actual range measurements had an effect on the echoic flow curves shown in Fig 6.6.b. Even though the $\alpha\ \beta$ tracker shows significant improvement in range measurement, the small variation in range caused a strong variation in τ_r due to using consecutive pulses to calculate range rate in (4.3).

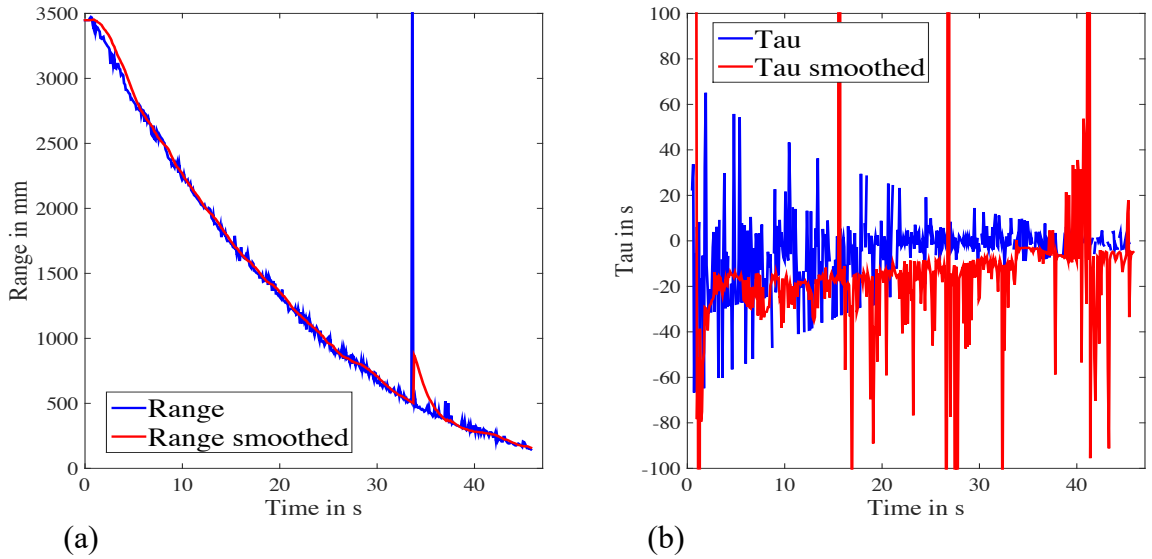

Fig. 6.6: (a) Range and filtered range curves of radar reaching stationary target. (b) EF and filtered EF curves of radar reaching stationary target.

For the second trial, two methods were applied to achieve an accurate τ_r estimate. First, improving the accuracy of the range measurement by increasing the bandwidth to reach the acoustic radar system limit at B = 23 kHz, which results in a range resolution of 7.4 mm. Second, increasing the time interval between pulses for range rate measurements i.e. calculating range rate by taking the previous N^{th} pulse instead of the first previous pulse. Here I call N the PRF factor, and it was set to 10 pulses. See Fig. 6.7.

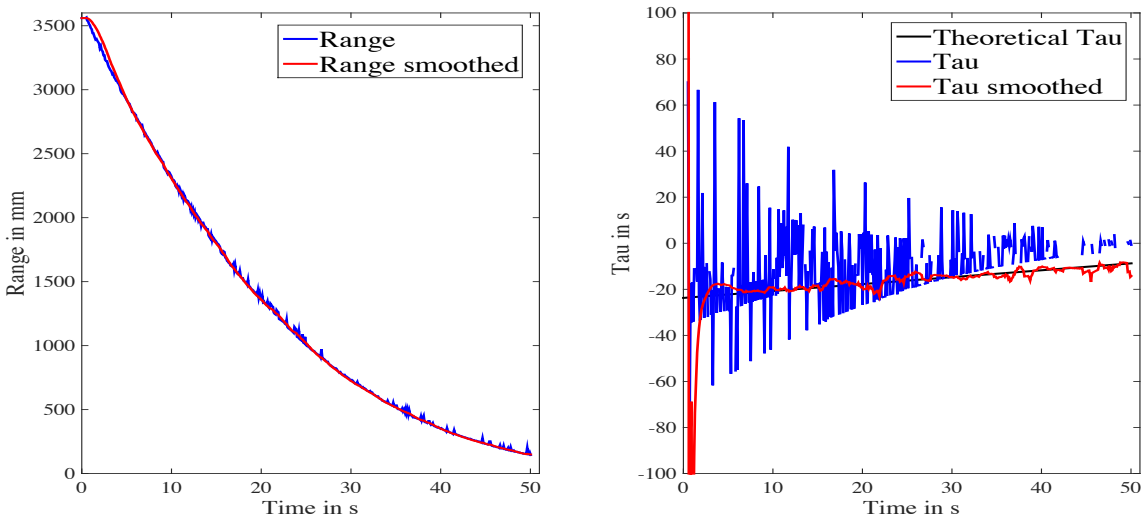

(a) (b)

Fig. 6.7: (a) High accuracy range curves of radar reaching stationary target. (b) High accuracy EF curves of radar reaching stationary target.

From Fig. 6.7.a, it is apparent that increasing the bandwidth of the transmitted signal significantly improved the range estimation accuracy such that the fluctuation around the smoothed estimate tracker was approximately 1 cm. Moreover, echoic flow after filtering and using PRF factor to measure range rate successfully converged around the theoretical echoic flow although still with some variation. Nevertheless, it shows an improvement in the estimation of EF due to the higher bandwidth and PRF factor.

For moving target experiments, a 0.5-by-0.5 m panel target was mounted on a second Pioneer 3-DX robot that moves at a constant speed $\dot{r}_T$, away from the acoustic radar testbed. Fig. 6.8 illustrates the acoustic radar testbed, colored in red, moving with velocity $\dot{r}_R$ towards a moving target, colored in blue.

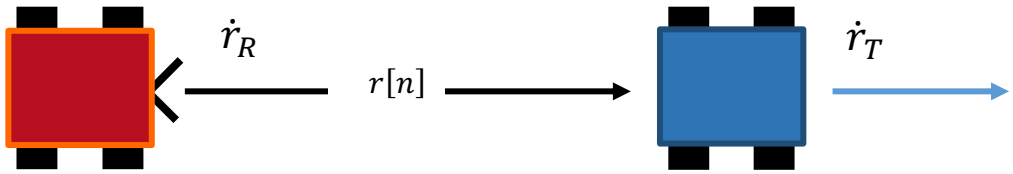

Fig. 6.8: A radar platform moving towards a target in motion.

Two moving scenarios were examined, target moving slower than the acoustic radar testbed, and target moving faster than the acoustic radar testbed. For each scenario, five trials were conducted to represent both early ($\dot{\tau}_r$= 0.1, 0.3) and late ($\dot{\tau}_r$= 0.7, 0.9) braking strategies, along with a linear braking strategy at $\dot{\tau}_r$= 0.5. Initial radar testbed and target velocity and range locations are presented in Table 6.4.

Table 6.4: Initial range and velocity of radar platform and target

Simulation Scenario	**Initial Radar Testbed**		**Initial Target**		**Initial Relative**	
	Range	**Velocity**	**Range**	**Velocity**	**Range**	**Velocity**
(1) Target velocity lower than radar platform	0 m	0.4 m/s	3 m	0.1 m/s	3 m	0.3 m/s
(2) Target velocity greater than radar platform	0 m	0.1 m/s	2 m	0.2 m/s	2 m	0.1 m/s

Fig. 6.9 shows the motion curves of the robotic platform moving with an initial velocity of 0.4 m/s heading towards a moving target with a constant velocity of 0.1 m/s, and a 3 m initial gap between the robotic platform and the target. The robotic platform motion curves took the same path as in the simulation presented in Fig. 6.3, with both range and relative velocity gaps closed. Note that for the late braking strategy case ($\dot{\tau}_r$= 0.7, 0.9), the radar platform had a slightly higher final velocity compared to the target, which results in a soft collision.

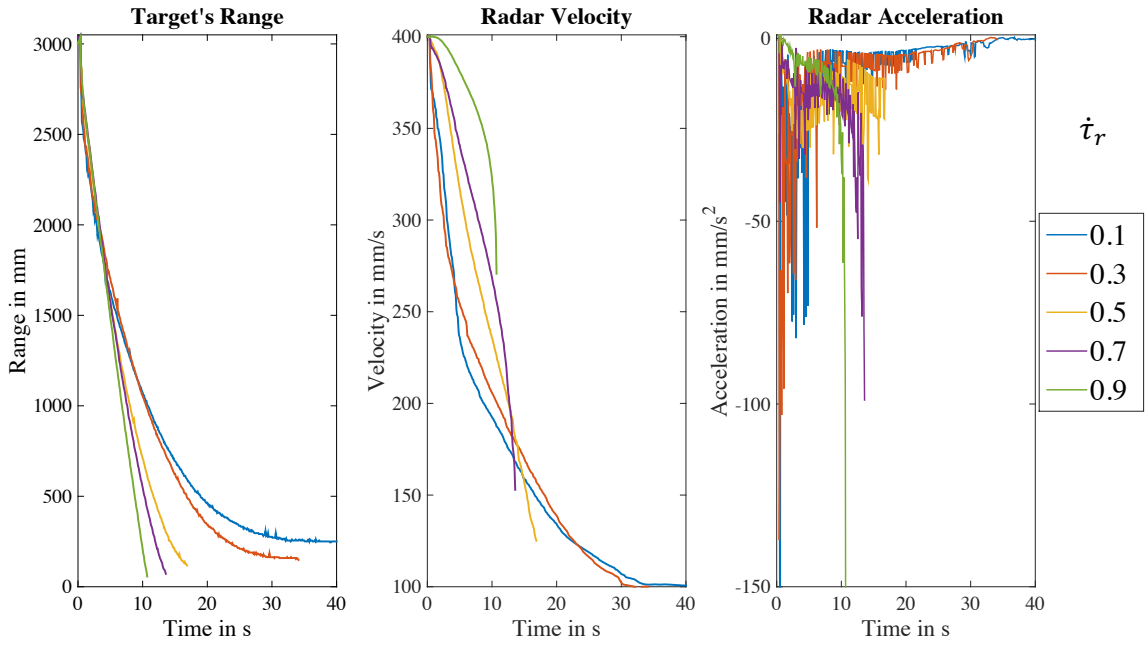

Fig. 6.9: Motion curves of the radar platform approaching a slow moving target.

In the second scenario, the target was set to move with a constant velocity of 0.2 m/s, whereas the robotic platform had an initial velocity of 0.1 m/s. Here the velocity of the target is higher than the initial velocity of the robotic platform. The starting gap was set to

2 m, while the maximum EF value is set to $\tau_{r\,max}$ = 5 s and the minimum relative velocity is set to $\dot{r}_{min}$ = 0.05 m/s. Range and velocity curves, Fig. 6.10, converged by following the same motion shown in the simulation set of Fig. 6.4 to close range and relative velocity gaps.

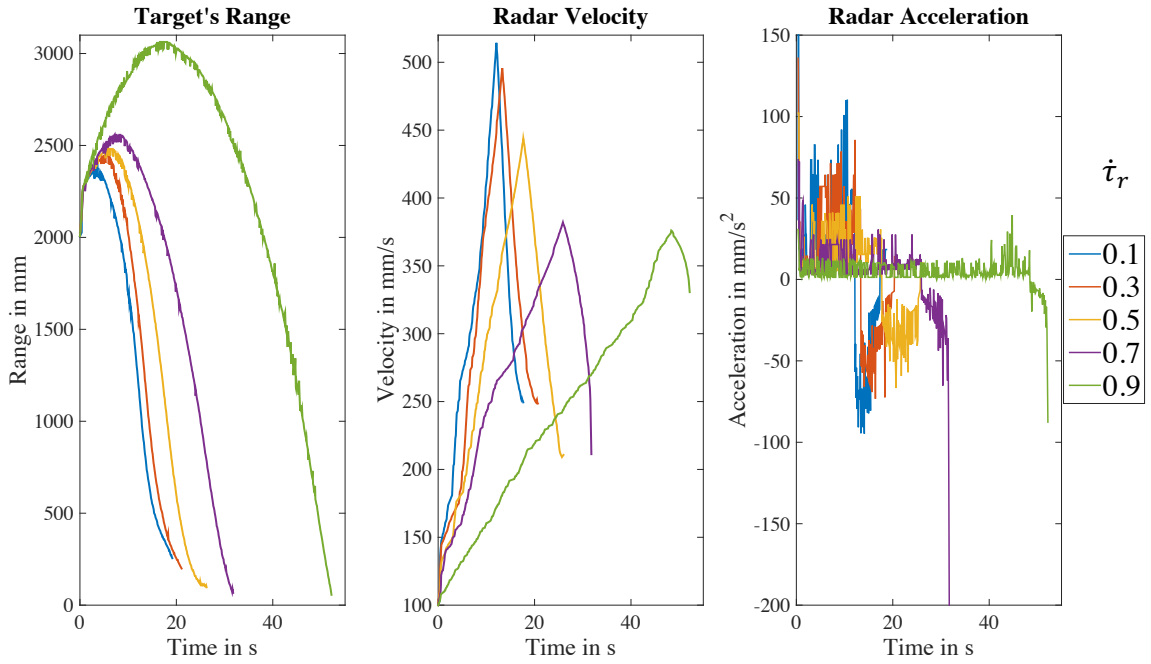

Fig. 6.10: Motion curves of the radar platform approaching a fast moving target.

By using a pulsed LFM acoustic radar, following and approach of a moving target was achievable. The strong variation in range, and hence, echoic flow measurement was overcome by increasing the signal bandwidth and by applying a smoothing filter. Range rate measurements were improved by increasing the time intervals between pulses.

However, the acoustic radar testbed's potential was obtainable by using a Triangular FMCW to measure both range and Doppler velocity presented in the next section, where the echoic flow can be directly measured for each update.

6.2.2 Using FMCW Radar

For the second part of the experimental set, a triangular FMCW radar was used. The nature of the triangular FMCW radar allows to measure both range and Doppler to the target for each modulation period T_m, which helps accommodate the low modulation frequency f_m (Similar to PRF in pulsed radars) of the Acoustic Radar. Here, f_m was set to 5 Hz and the modulation bandwidth ΔF was set to 23 kHz (25 kHz-48 kHz), Table 6.5. Please refer back to section 3.2 and 3.3 for more about acoustic FMCW radar.

Table 6.5: Acoustic Triangular FMCW Radar Parameters

Parameter	**Value**
Modulation Bandwidth (ΔF)	23 kHz
Modulation Period (T_m)	0.2 s
modulation frequency (f_m)	5 Hz
Center Frequency (f_o)	36.5 kHz
Minimum Signal Overlap	%80

The ability to measure Doppler velocity to the target will allow an independent velocity measurement from range measurement, and hence, avoid strong variation in τ_r due to using consecutive pulses to calculate range rate, and will eliminate the need to use a smoothing filter compared to using the LFM pulsed radar.

For the first experiment, a 0.5-by-0.5 m panel target was stationed three meters in front of the acoustic radar testbed. The testbed had an initial velocity of the 300 mm/s. By examining the case when tau dot is set to 0.3, both range and tau measurements are shown in Fig. 6.11. The improvement in both range and tau measurements when using an acoustic FMCW compared to a pulsed radar is apparent.

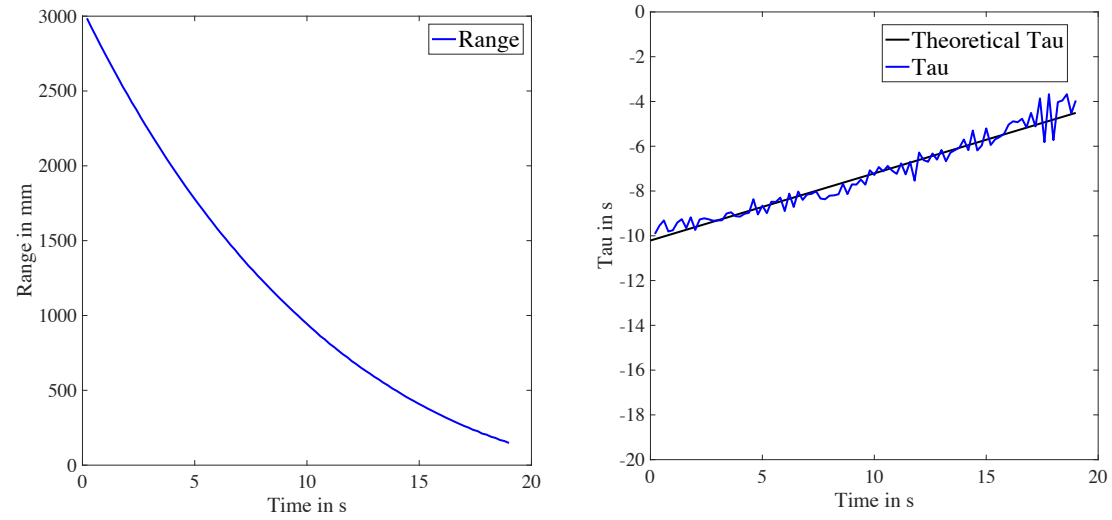

(a) (b)

Fig. 6.11: (a) Range curve of radar reaching stationary target using FMCW. (b) EF curves of radar reaching stationary target using FMCW.

Furthermore, two extra experiments were conducted when the target is in motion. The target is similar to the LFM case, where a 0.5 by 0.5 m panel was mounted on a second robotic vehicle, Fig. 6.8. The starting conditions are left the same as shown in Table 6.4, with the radar testbed moving with an initial velocity of 0.4 m/s towards a target that had a constant velocity of 0.1 m/s. The initial gap between the radar testbed and the target is kept at 3 m.

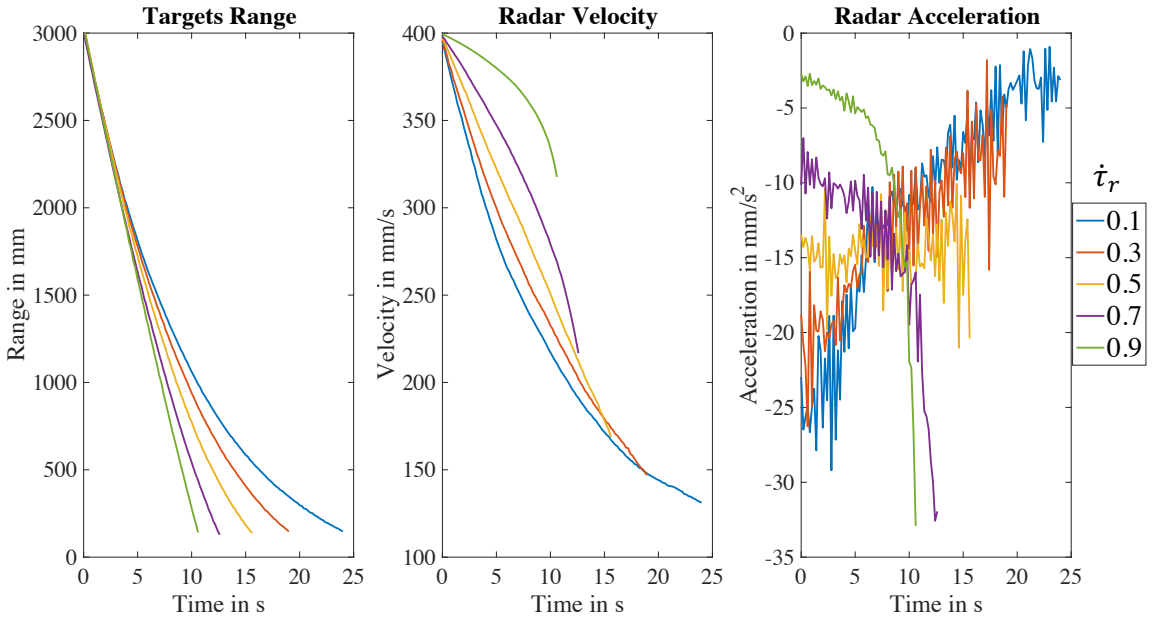

Fig. 6.12: Motion curves of the radar platform approaching a slow moving target.

Comparing Fig. 6.12 with Fig. 6.9, the range, velocity and acceleration curves are smoother, and have less variation. This is especially present when focusing on the radar testbed's acceleration throughout the experiment. Also, the three braking scenarios are present and can be shown based on early ($\dot{\tau}_r$= 0.1, 0.3), late ($\dot{\tau}_r$= 0.7, 0.9) and, linear braking strategy at $\dot{\tau}_r$= 0.5.

It should be also noted that when using the FMCW radar, the measurement updates are half, at five per second, compared to LFM, at ten per second. The decrease in measurement update did not affect the path followed by the acoustic radar testbed, and shows that it can be sufficient for such radar platform velocity.

While, for the last experiment, the target is moving away from the testbed with a constant velocity exceeding the testbed's initial velocity, at 0.2 m/s and 0.1 m/s respectively. The initial distance between the platform and the target was set to be 2 m. Here, and based on the boundaries introduced in (4.20) and (4.21), maximum echoic flow value and minimum relative velocity are set to $\tau_{r\,max} = 5$ s and $\dot{r}_{min} = 0.05$ m/s respectively. This is a confirmation that all experimental setup initial conditions are the same as the LFM radar case.

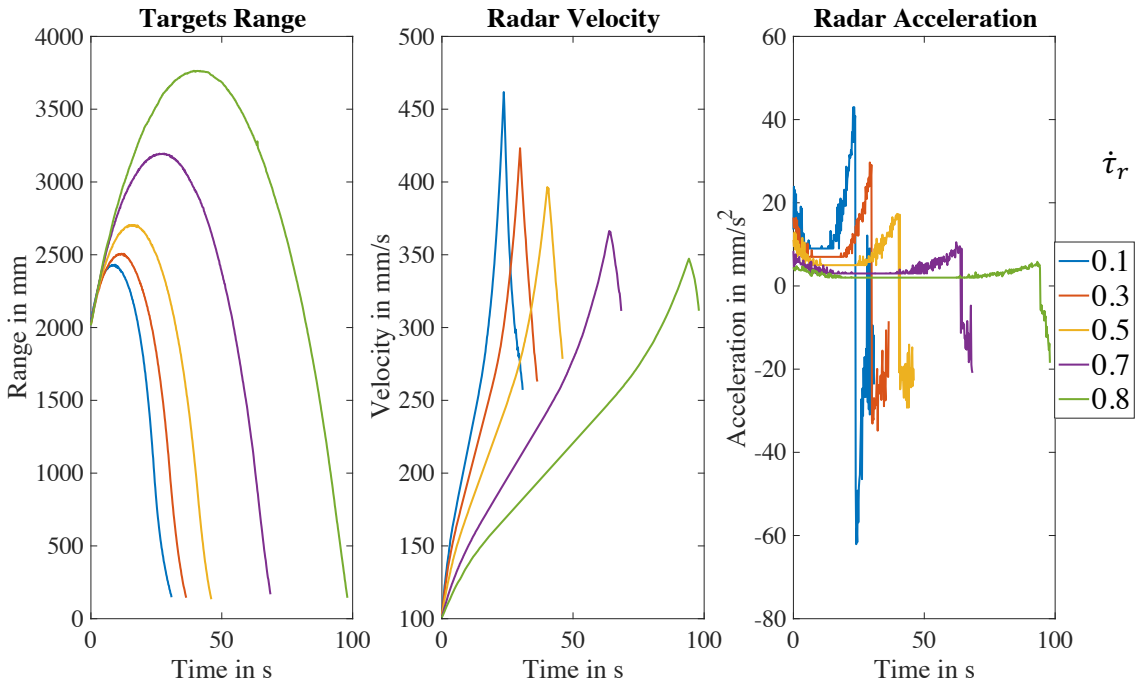

Fig. 6.13: Motion curves of the radar platform approaching a fast moving target.

Given that this case is more challenging since it does consist of both an acceleration, followed by a deceleration, it is clear that output curves in Fig 6.13 differs from Fig. 6.10.

While the two experiments succeeded in performing a gap closer in both range and relative velocity, they differ in measurement accuracy and time consumed executing the experiment. When using a continuous wave two measure both range and Doppler velocity at the same time, and then determine the time to contact τ, all range, velocity and acceleration curves were less variable.

However, using a pulsed wave to measure range showed an execution time that's almost half the time required to finish the continuous wave case. This is due to the large variation in acceleration outputs fed to the robotic platform from the radar shown in Fig 6.10 compared to lower variations in Fig 6.13. The large variations in acceleration outputs increased the robot's maximum velocity in each scenario and helped close the gap sooner than predicted. Regardless of the large variations in acceleration, the echoic flow adapted to each update individually and successfully closed the gap.

While, when comparing the experiment output of using FMCW to simulation. Fig. 6.14 shows simulation and experiment progressions of range, velocity, and acceleration presented in one figure. Where, blue colored curves are simulation, and red colored curves are experiment.

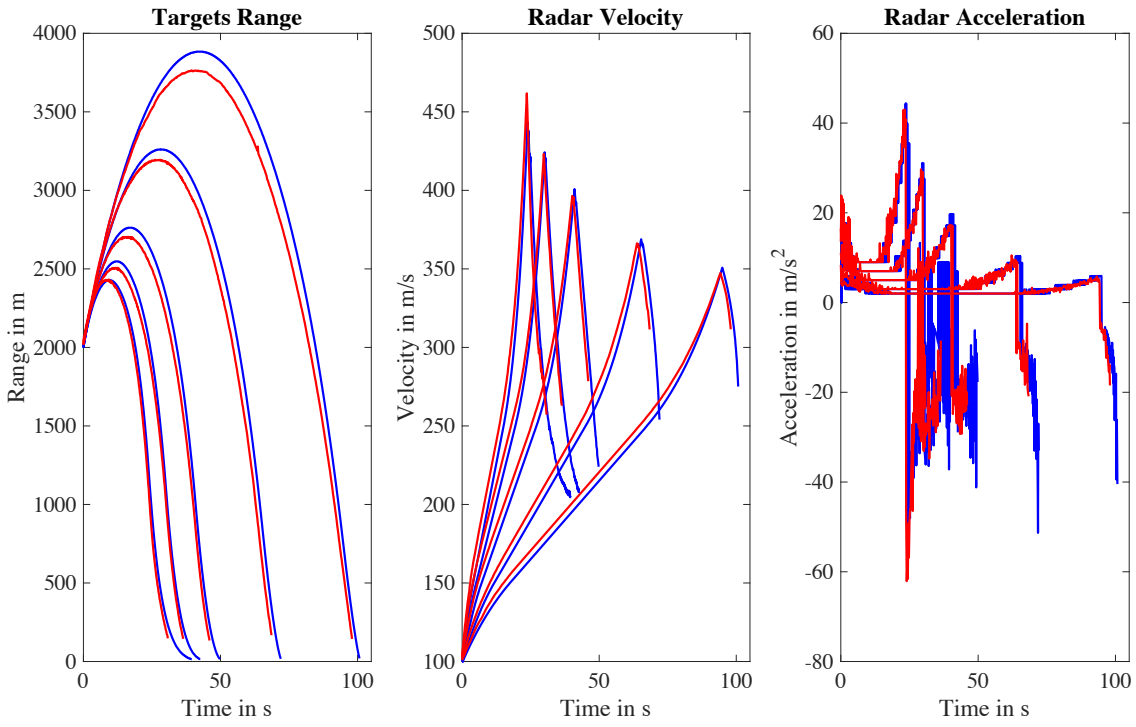

Fig. 6.14: Simulation and experimental motion curves of the radar platform approaching a fast moving target.

The progression of range, velocity, and acceleration curves are similar in nature and follow the same curve. While, the similarities between simulation and experiment is obvious, a small variation can be seen in the range curves, where in simulation, the gap between the radar platform and the target slightly increased before being closed, compared to experiment. This is also apparent with simulated velocity curves taking slightly more time to converge.

The convergence of the experimental curves being marginally faster compared to simulation agrees with the hypothesis that the variation of acceleration curves help speed

up the gap closing approach. However, since the variations of acceleration curves are minimal, the simulation and experiment outcomes were very close.

6.3 Conclusions

A series of simulations and actual experimental work with three braking scenarios were presented for an acoustic radar testbed that used both LFM and FMCW waveforms to approach and follow stationary and moving targets. It was shown that successful closing of both range and relative velocity were possible in each trial. While, a novel approach is presented when the target is moving away from the radar platform.

Chapter 7: Echoic Flow for Guidance and Aperture Traversal

In this chapter we demonstrate the effect of echoic flow aided sensors on bio-inspired guidance and navigation. Then using the same principles, robotic aperture traversal is applied and tested.

The first set of experiments regarding navigating through corridors; of varying shapes, including obstacles. The echoic flow measurements obtained from both, the robot's ultrasound sensors and the fully developed acoustic radar will be presented. Then, the second set of experiments involving traversing an aperture is shown. Starting with the simple case of square rooms with single aperture and the robot with a forward direction start position. Then moving to situations where the robot starts by facing other directions. Finally, the case where multiple apertures are crossed is demonstrated and discussed.

7.1 Echoic Flow for Guidance

We seek to develop a guidance approach that will enable an autonomous vehicle to avoid collision while navigating through enclosed environments. In [1], [2] the concept of using echoic flow for guidance was demonstrated using a simulation. Here an experimental validation of the autonomous guidance approach was performed.

7.1.1 Experimental Setup

For the autonomous guidance experiments, three environments were built; straight corridor, square corridor, and square corridor with obstacles. For each environment two methods of building the environment are applied. Rectangular plywood walls, and individual evenly spaced PVC poles. For the environment that was made from plywood walls, it also was lined with corrugated wrap to increase reflectivity. Each section of wall was 1 m long and 0.5 m tall, with bases on the rear to allow it to stand. By arranging the wall segments, different corridors are created.

7.1.1.1 Using Robot's Internal Sensors

Here, the robotic platform, the Adept MobileRobots Inc. Pioneer 3-DX, as described in section 4.1, was used with its internal sensors. For this set of experiments, only two of the robot's eight internal sensors were used to measure echoic flow, those with $\pm 50°$ angle to be consistent with the simulation of [2]. In addition to measuring the ranges to obstacles, the platform knows its speed. The platforms forward velocity is then projected onto the beam directions.

$$\dot{r}_{beam\ direction}(t) = \dot{r}_{robot}(t) \times \cos(\theta) \tag{7.1}$$

where θ is the angle of the sensors to the direction of the robot's forward travel, while $\dot{r}_{robot}$ is the robot's forward velocity.

From range and speed, echoic flow values are determined in both beams based on (4.2), where $\tau_r(t)$ is the echoic flow measurement at time t. In other words, the echoic flow is

determined for each range measurement obtained from the sensors, and divided by the platform's projected velocity (7.1).

By obtaining both echoic flow measurements from the left and right sensors, a decision is made to steer away from the closest time to collision, which is the highest echoic flow value. Fig. 7.1, shows the robotic platform moving with a predetermined forward velocity v, and turning to the right since the left sensor has a smaller time to collision compared to the right sensor.

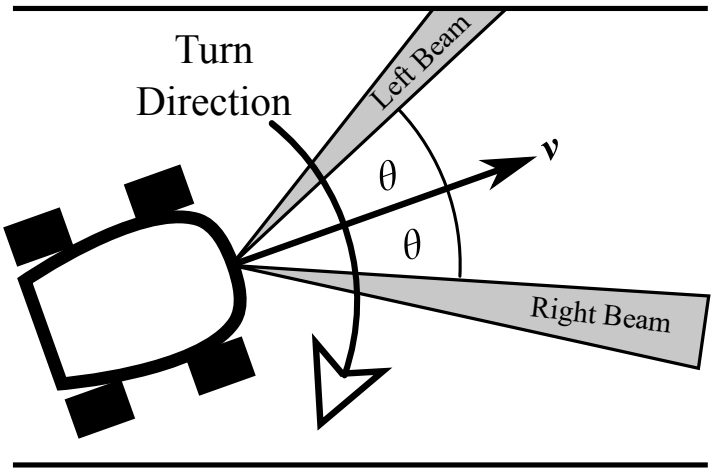

Fig. 7.1: Schematic robot platform with left and right 50^{o} beams.

The perception-action cycle used to guide the robot is shown schematically in Fig. 7.2 with the parameters for echoic flow listed. This cycle represents a modification of the simple algorithm used in [1], [2] providing the robot with a detailed sensing architecture. The inputs to the cycle are the parameters measured by the robot platform's sensors and the outputs are turning instructions that set the rate of turning and the duration of turn. After projection of the speed onto the directions of the radar beams, the inputs to the cycle are

the ranges, r_n, and speeds, v_n, for the left and right beam directions, where n is the observation index. The values are stored in the short-term memory and are used to calculate the echoic flow in the left and right directions, τ_{left} and τ_{right} respectively, using (4.2). These two EF estimates are considered the robot's perception of the local environment.

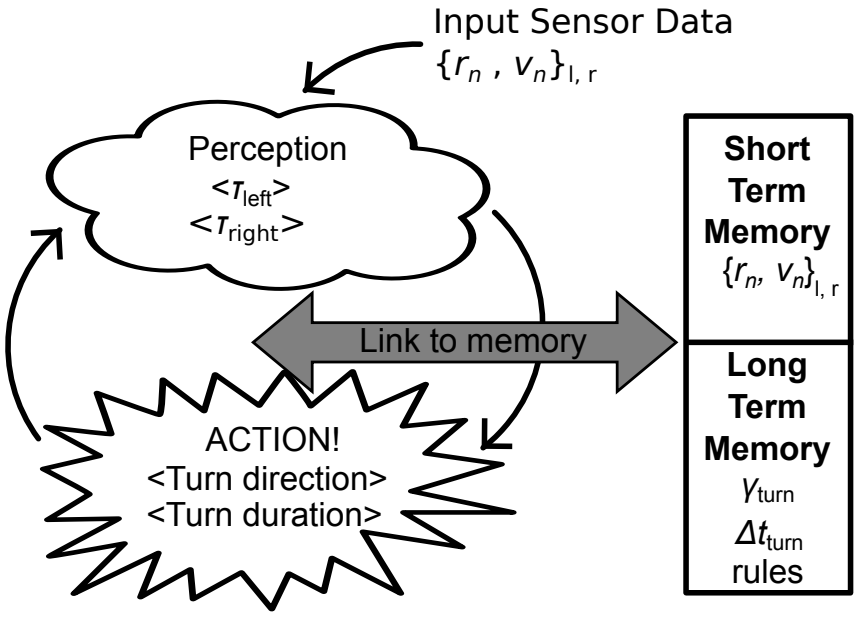

Fig. 7.2: Perception action cycle for Echoic Flow guidance.

The selection of an action, based on the perception, requires a task objective to be known. In this research, the task was collision avoidance, and the strategy to achieve this was chosen to be, "steer away from the direction with shortest time to collision, i.e. minimum EF". As described in [1], [2], if an infinitely long straight corridor were imagined, this strategy would steer onto the centerline, and so achieve the task of not colliding. Based on the desired perception, a set of three rules were identified. They are listed in Table 7.1.

Table 7.1: Rules for cognitive guidance by echoic flow

Rule ID	**Rule**
1	If $\tau_l > \tau_r$ then turn right
2	If $\tau_l < \tau_r$ then turn left
3	If $\tau_l = \tau_r$ then no turning
4	If performing a turn set the duration of the turn to be $\Delta t_{\text{turn}} = f(\lvert\tau_l - \tau_r\rvert)$

For rules, 1, 2 and, 3 it should be noted that the sign convention of $\dot{r}$ is set to being negative while r is positive, produces a negative echoic flow for closing gaps, so $\tau_l > \tau_r$ indicates the shortest time to collision is to the left and a need to turn right.

Furthermore, the duration of the turn is proportional to the absolute difference between the left and right τ values as shown in (7.2).

$$\Delta t_{\text{turn}} = f(x) = \begin{cases} 0.4 & \text{if } x > 4 \\ \dfrac{x}{10} & \text{if } x \leq 4 \\ 0 & \text{if } x = 0 \end{cases} \tag{7.2}$$

Equation (7.2) states that if the absolute difference between the time to collision in the two sensors is greater than $4s$, $\left|\tau_{left} - \tau_{right}\right| > 4s$, then, the robot will rotate 35° per second to the direction of the highest time to collision for $0.4s$. While, if $\left|\tau_{left} - \tau_{right}\right| \leq 4s$, then the rotating duration $= \frac{\left|\tau_{left} - \tau_{right}\right|}{10}$. Otherwise, if the left and right τ values are equal, then no rotation is made, and the robot will go forward. This equation is based on

experimental trials and is affected by the number of measurements the sensors are making per minute. In other words, if the sensors PRF changes, then the constants in (7.2) will be changed to adapt to the new changes is the PRF.

7.1.1.2 Using the Acoustic Radar Testbed

For the second set of experiments, the environment was made from PVC poles that represent a point target. The poles are carried vertically by a metallic base to provide better support and durability. Each pole is one inch in radius $\approx 2.5\ cm$ and two feet in height $\approx 60\ cm$. The poles are set to be $20\ cm$ apart and various environments can be formed using these vertical poles. Note that the distance of the gap between the poles is measured to the center of the pole.

While the robotic platform used for this set of experiments is the same as the previous set, an Adept MobileRobots Inc. Pioneer 3-DX, the robot's internal sensors are not used. Instead, a fully developed acoustic FMCW radar system with two $\pm 45°$ microphones and two $\pm 45°$ loudspeakers were used to be the platform's perception, and an onboard laptop provides the robot with actions based on the radar's perception. Please see section 5.2 and 5.3 for more details on the acoustic radar testbed.

While using the robot's internal forward velocity measurement as a guide to the echoic flow measurement on both internal sensors in the previous set, here the acoustic radar measures both range and Doppler velocity to each individual pole; and hence, using range over Doppler velocity to determine the echoic flow value to each pole. This type of measurement is more consistent with the echoic flow theory and gives a true time to collision towards each pole, Independent of knowledge of the actual robot's forward

velocity. Therefore, from equation (4.5), $r[n]$ is the relative measured range to the pole and $\dot{r}[n]$ is the relative measured Doppler velocity from the FMCW radar's microphone and loudspeaker.

Moreover, the same task objective is set to avoid collision by steering away from the direction with shortest time to collision, and the three rules of Table 7.1 were kept the same. However, the duration of the turn is changed to accommodate the new PRF and the improved way of measuring range and range rate to get τ. Therefore, the duration of the turn is proportional to the absolute difference between the left and right τ values as shown in (7.3).

$$\Delta t_{\text{turn}} = f(x) = \begin{cases} 0.2 & \text{if } x > 2 \\ \dfrac{x}{10} & \text{if } x \leq 2 \\ 0 & \text{if } x = 0 \end{cases} \tag{7.3}$$

Equation (7.3) states that if the absolute difference between the time to collision in the two sensors is greater than $2s$, $|\tau_{left} - \tau_{right}| > 2s$, then, the robot will rotate to the direction of the highest time to collision for $0.2s$. While, if $|\tau_{left} - \tau_{right}| \leq 2s$, then the rotating duration $= \frac{|\tau_{left} - \tau_{right}|}{10}$. Otherwise, if the left and right τ values are equal, then no rotation is made, and the robot will go forward. Note, the rotational angle is set to 15° per second.

This equation (7.3) is determined after several experimental trials to find a balance between a smooth guidance through a straight corridor and the ability to turn through corners. By increasing the angle of rotation, the traversal of the corners is more achievable, however, this will increase the oscillation of the robot's movement in a straight corridor.

While decreasing the rotational angle will decrease the oscillation in a straight corridor, it will also increase the difficulty of going through a corner. Furthermore, the number of measurements the sensors are making per minute is fixed to $PRF = 5\,Hz$, which allows $0.2\,s$ before the subsequent measurement is performed, and that sets the upper limit of rotational time to $0.2\,s$.

While performing this experimental set, each left and right sensor used in the acoustic radar experimental testbed measures the echoic flow of all illuminated poles of the environment; however, only the minimum τ from each side, $\min \tau_{left}$ and $\min \tau_{right}$, are used in the bio-inspired guidance rules of Table 7.1, which represents the closest pole to collide with on each side of the acoustic radar testbed.

7.1.2 Experimental Results

7.1.2.1 Using Robot's Internal Sensors

For this experiment, the robot was placed in a straight corridor with a 2 m width. The robot started with a 50° angle from the forward direction as shown with the pointing arrow in Fig. 7.3. Where the black lines show the corridor's left and right walls, and the red line shows the path of the robot, while the circle and triangle indicated the starting and ending points of the path respectively. note that the robot has a 48 cm width and the line indicates only the center of the robot. The speed was fixed to 100 mm/s. At first, the robot turned avoiding the left wall, and then moved towards the center of the corridor by trying to avoid both walls.

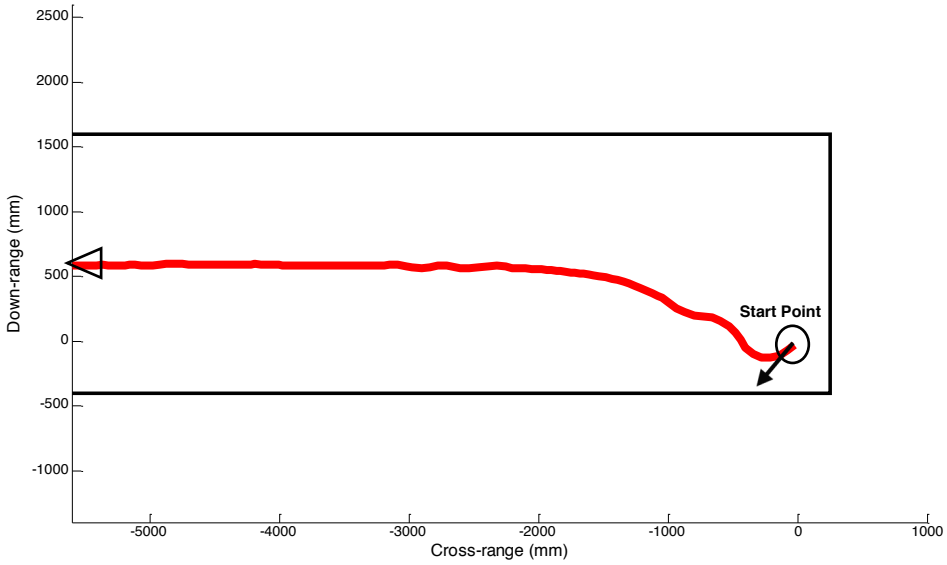

Fig. 7.3: Path of robot in a straight corridor with a 50° starting angle.

The robot's perception of the corridor, the echoic flow in the left and right facing sensors, is shown Fig. 7.4 as a function of time. The blue line is for the left sensor measurement, and the red for the right. The sign convention of (7.1) causes the EF to be negative for each sensor. At times $t < 1$ the EF form the right sensor remained at the maximum time to contact. This was because the right sensor pointed along the length of the corridor and so measured the maximum range of 5 m. The left sensor pointed towards the adjacent wall and measured an EF value close to 0 s. The initial perception caused the robot to turn hard right, as can be seen in Fig. 7.4. Which led the left sensor to point along the length of the corridor and the right sensor towards the right side wall. However, after $t > 9$ the path of the robot was leveled while approaching the center of the corridor.

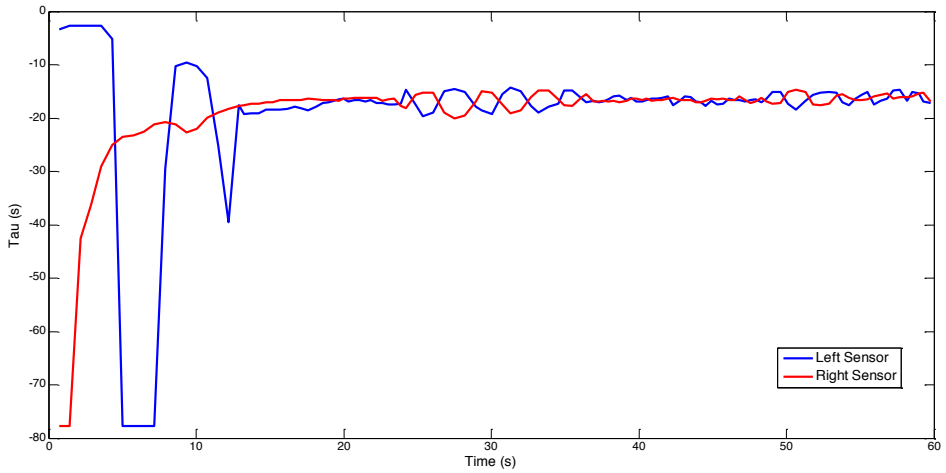

Fig. 7.4: Left and right echoic flow sensor readings for straight corridor.

At the 23rd second, the robotic vehicle started mildly oscillating by turning slightly left and right. This is apparent in both the echoic flow return in Fig. 7.4 and the robot's actual path in Fig. 7.3 after crossing the range of $\approx 2300\,mm$. The oscillation in the robot's movement is thought to be mainly form the imperfections of the corrugated wall which led the ultrasonic sensor to output a slightly deviated echoic flow measurement, resulting in a variation from the centerline path. However, it is important to note that despite this error, the cognitive guidance algorithm quickly corrects itself.

For the second set of experiments, the robot was placed in a square corridor of 1m width, that was built from two squares, a 3×3 m and a 5×5 m, and covered with corrugated wrap as shown in Fig. 7.5.

Fig. 7.5: Square corridor experimental set.

In this experiment the robot was placed on the center of the corridor, facing forward. The speed was increased to 250 mm/s and started at the initial point (0, 0) and navigated clockwise through the corridor while trying to keep itself in the center of the corridor. It also turns through corners with different turning angles based on the position where it started turning. The robot's path is shown in Fig. 7.6.

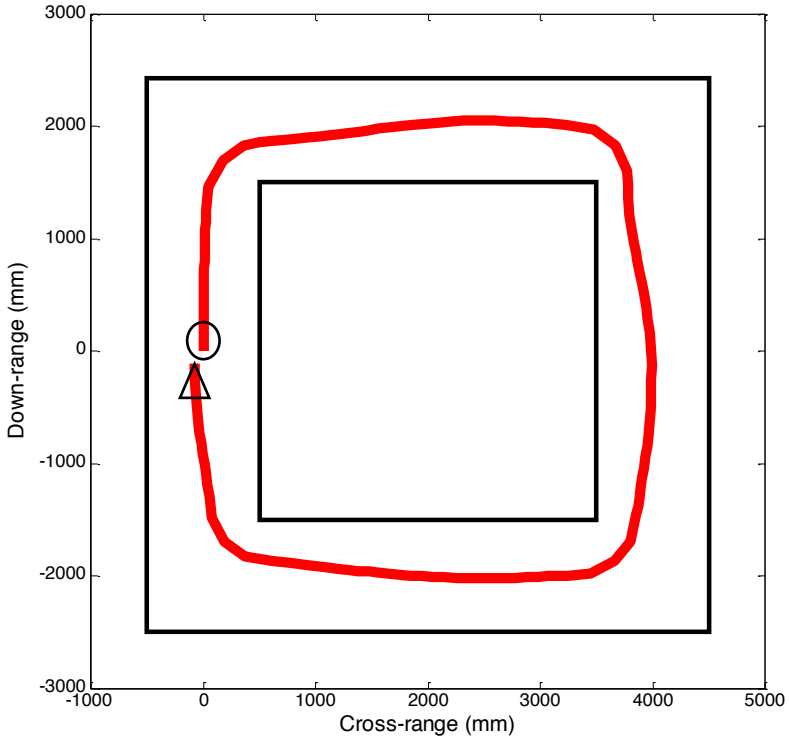

Fig. 7.6: Path of the robot in a square corridor.

The perception of the environment, the echoic flow measurements from the left and right sensors, is shown in Fig. 7.7. At the start of the path, it is apparent that the robot is getting almost equal measurements from both sensors and follows a straight path until it reaches a corner at $t = 7\ s$, where the right sensor shows a sudden increase in time to collision guiding the robot to turn right pending the time to collision in both sensors to balance. The corner was perceived in two stages, the first when the left sensor illuminates the forward wall resulting in a 10 s tau measurement, then while rotating to the left, the second stage of illuminating the end of the corridor results in an EF measurement of 26 s. perceiving a corner is shown at $t = 7{,}21{,}38\ and,\ 51s$ respectively.

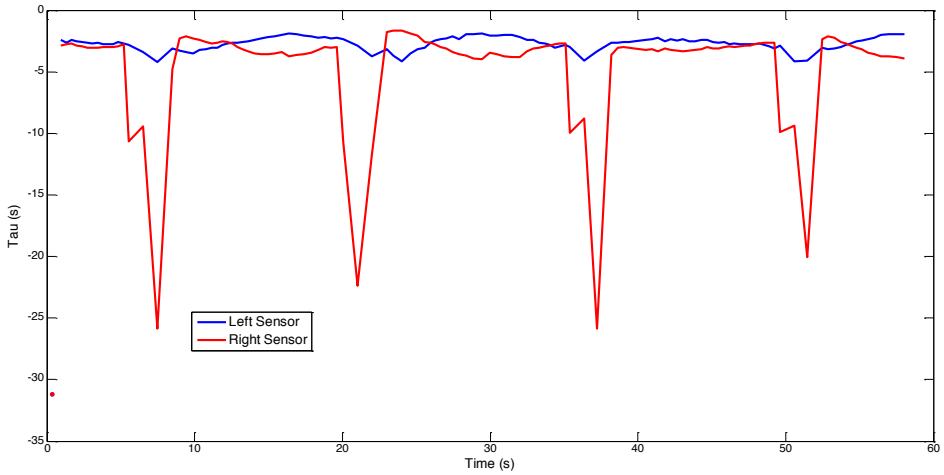

Fig. 7.7: Left and right echoic flow sensor readings for square corridor.

To show that the bio-inspired approach used with echoic flow is dependent on the relationship between the robot and the environment and that it is not a deterministic approach, the robot completed five rounds through the square corridor. It can be seen in Fig. 7.8 that the robot traveled a slightly different path while executing each round. And turns through corners with different turning angles based on the position where it started turning.

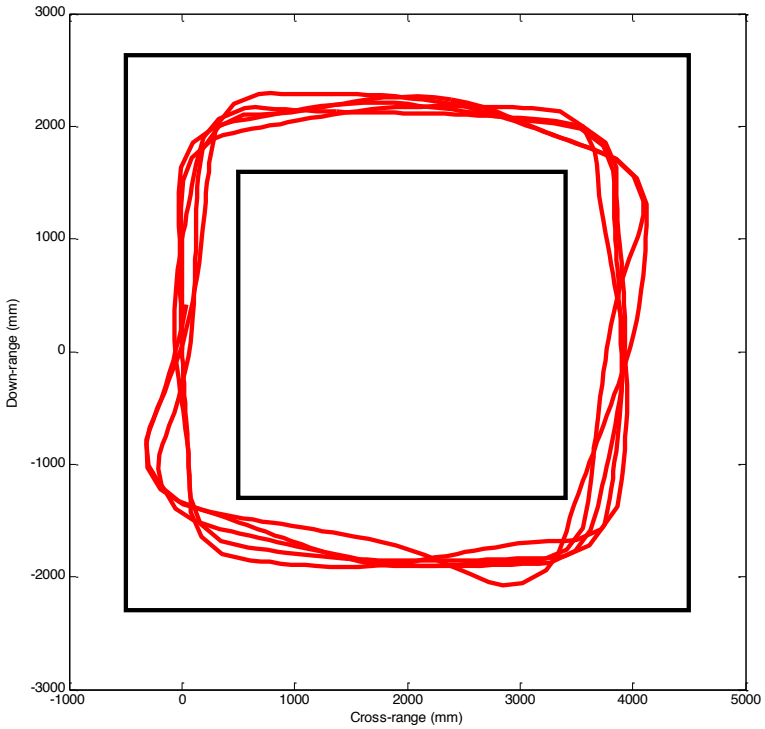

Fig. 7.8: Path of the robot in a square corridor for 5 rounds.

For the final experiment, three 0.5 m width obstacles were added to the right side of the square corridor, and robot's starting direction was 65° to the left of the forward direction, Fig. 7.9. Because of the ultrasonic sensor's low PRF, the robot must wait 0.3 s for an update in the range measurement. Therefore, the speed of the robot was set to 100 mm/s to have sufficient update rate measurement while navigating through obstacles. If the sensors provided a faster update rate, it is proposed that the robot would be able to guide through this corridor with higher speed. Fig. 7.9 shows the robot's clockwise path navigating through the square corridor with obstacles.

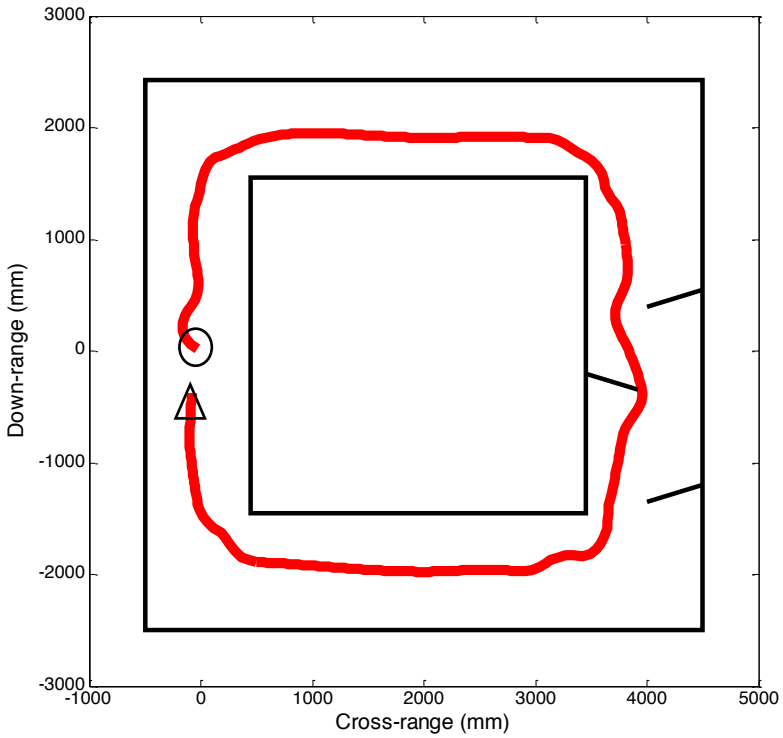

Fig. 7.9: Path of the robot in a square corridor with obstacles.

Fig. 7.10 shows the robot's echoic flow perception as a function of time for the square corridor with obstacles. When starting, the left sensor had a smaller time to collision, τ value, that made the robot turn right to avoid colliding with the left wall, and thus briefly equalizing τ readings in both sensors by centering itself in the corridor. It is apparent that the robot slightly oscillates until it reaches the first corner, where the right sensor perceives a sudden increase in time to collision guiding the robot to turn right through the corner. The perception when traversing the first corner is more extreme compared to traversing the corner with the regular square corridor case. The increased fluctuation here is due to the robot failing to reach an optimal center point before entering the first corner. However, after navigating the first corner, the time to collision in both sensors balance before

reaching the second corner and a steady center position is reached long before reaching the second corner. Hence, the perception is comparable to the square corridor case. Furthermore, as soon as the robot exited the second corner at $t = 55s$ it perceived the first obstacle, and the echoic flow between $t = 55s - 85s$ varied rapidly as the robot successfully navigates through the obstacles.

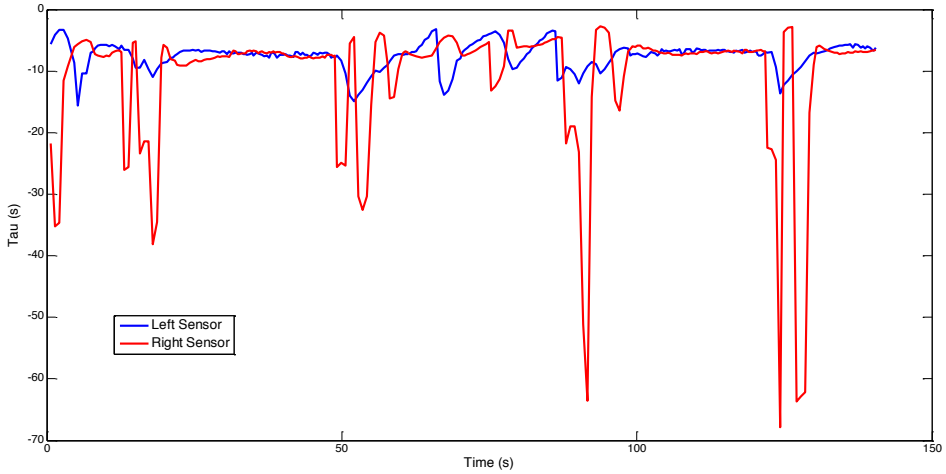

Fig. 7.10: Left and right echoic flow sensor readings for square corridor with obstacles.

From this set of experiments, it is apparent that by using two onboard range transducers, and projecting the robot's internal velocity on each beam, we were able to measure echoic flow. Yet, the simple rule of moving away from the minimum time to contact was sufficient in guiding the platform through complex enclosed environments. However, the transducers frequency, PRF, waveform and power were fixed, along with the inability to measure velocity from the sensors led to developing an acoustic radar, which was used in the section below.

7.1.2.2 Using the Acoustic Radar Testbed

For this set of experiments, the acoustic radar testbed, which consists of the acoustic radar system and the robot, was placed in a square corridor built with a sequence of evenly spaced PVC poles. The distance between each two individual poles are set to 20 cm measured from the center of the pole. The square corridor is set by building two squares, a 4×4 m and a 2×2 m, which allows a one meter width corridor. Fig 7.11 shows how the corridor was set in the lab prior to conducting the experiment.

Fig. 7.11: Square corridor with poles experimental set.

The robot was positioned in the middle of the right side corridor facing forward. The speed of the robot was set to 100 mm/s, and had both left and right sensors look $\pm 45°$ to the left and right parallel pole walls. This will allow the testbed to travel anticlockwise while moving through the corridor. Fig 7.12 expresses the path followed by the robot.

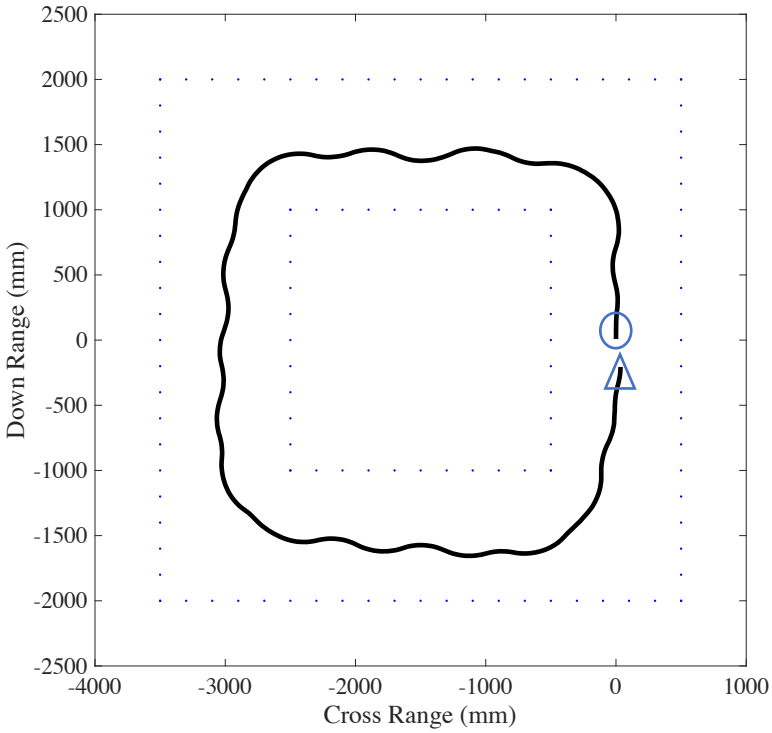

Fig. 7.12: Path of the robot in a square pole corridor.

The black solid line represents the path of the robot moving around the corridor, while the blue dotted lines are the poles forming the walls of the two inner and outer rooms. The testbed started the movement from the point (0,0) and moved forward before reaching the first corner, where it sharply turned left and continued moving in the center of the corridor with a small oscillation in the movement. The oscillation is generally caused by two factors, the discontinuity of the reflections from the poles and the small variation in the returning echoic flow measurement caused by minimal variations in both range and Doppler measurements. Regardless of the slight oscillation when moving through the corridor, the testbed kept guiding through the corridor until reaching the second corner. The same

behavior of the testbed continues throughout the experiment, and successfully completes a full loop around the square corridor by using range and doppler returns from the acoustic radar system to calculate the echoic flow as a perception, and then pass on actions to the robot using the predetermined rules of Table 7.1.

The perception of the square pole corridor is shown in Fig 7.13, where the x axis shows the time during the experiment in seconds and the y axis represent both left and right τ readings in seconds, with red and blue color lines respectively.

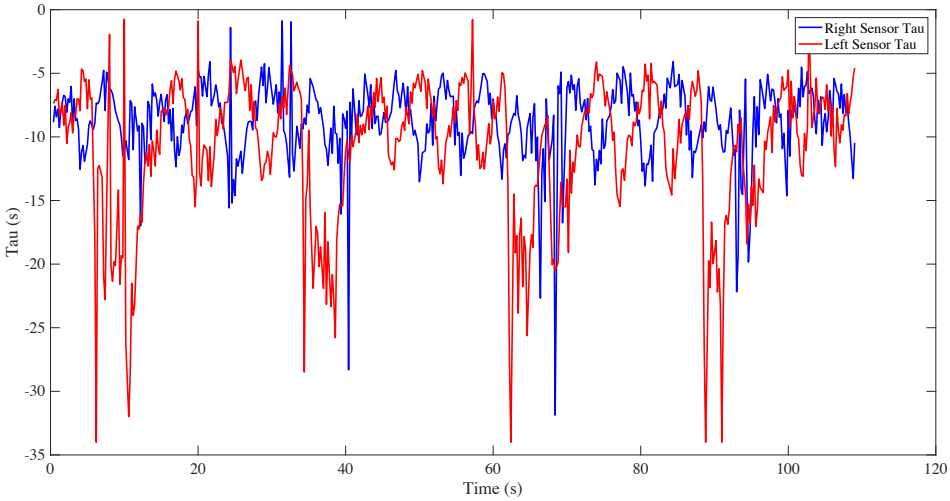

Fig. 7.13: Left and right echoic flow sensor readings for square pole corridor.

For the first five seconds of the experiment, the perception on both sensors had a τ value that is less than 10 seconds, with a small variation between the left and right τ's. At $t = 6\ s$, the first corner was perceived by the left sensor resulting in a left turn action by the robotic testbed. By the 11^{th} second, the corner was traversed, and the testbed is repositioning itself around the center of the corridor from $t = 12\ s\ to\ 34\ s$. The oscillation of both the left and right sensor measurements of tau is visible between the two time frames,

and hence a constant correction of any deviation from the centerline is present. This is very similar to the oscillation of τ presented in Fig. 7.3 and Fig. 7.4 which was caused by imperfections in the continuous corrugated environment. Here the constant oscillation through the pole environment is caused by the discontinuities of the environment and the small variations of both range and Doppler velocity measurements to obtain τ. However, the testbed still maintains a center positions between the poles and navigates the three remaining corners at $t = 34, 62, \text{and } 88$ s respectively.

The same experiment was repeated with the acoustic radar testbed performing two consecutive loops around the track. This is done to explore the stability of the guidance approach through multiple runs, and to show that regardless of successfully guiding through the corridor multiple times, the path of each round is slightly different than the others, due to the independence of each environment perception. Fig 7.14 shows the radar testbed executing two loops around the corridor.

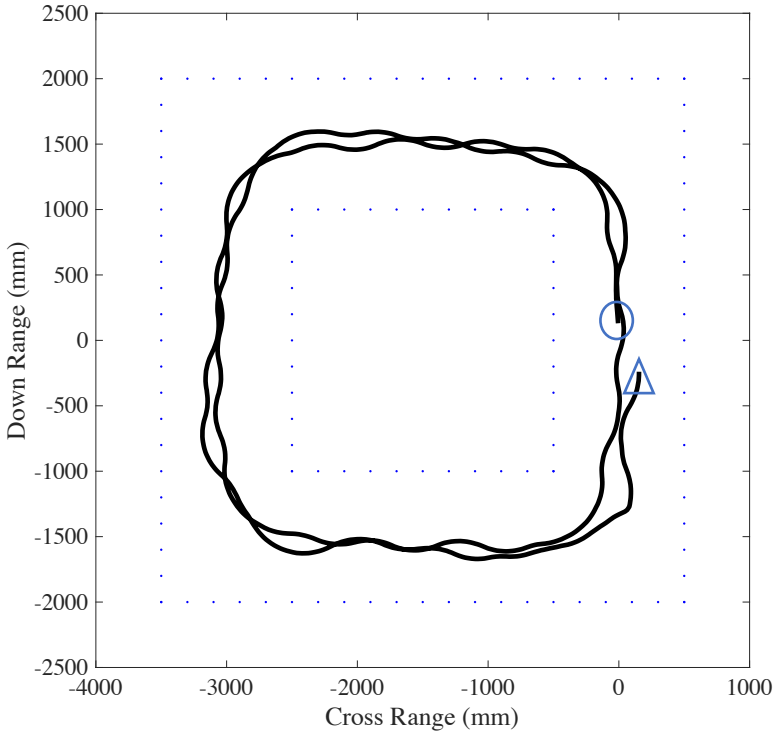

Fig. 7.14: Path of the robot in a square corridor for 2 rounds.

For the remaining experiments, two side obstacles were added to one side of the square corridor. Each obstacle is 40 cm in width and tilted 45^{o} to the side. For a more reliable experiment, two ways of building the obstacles were used, plywood panels and three evenly spaced poles as shown in Fig 7.15.

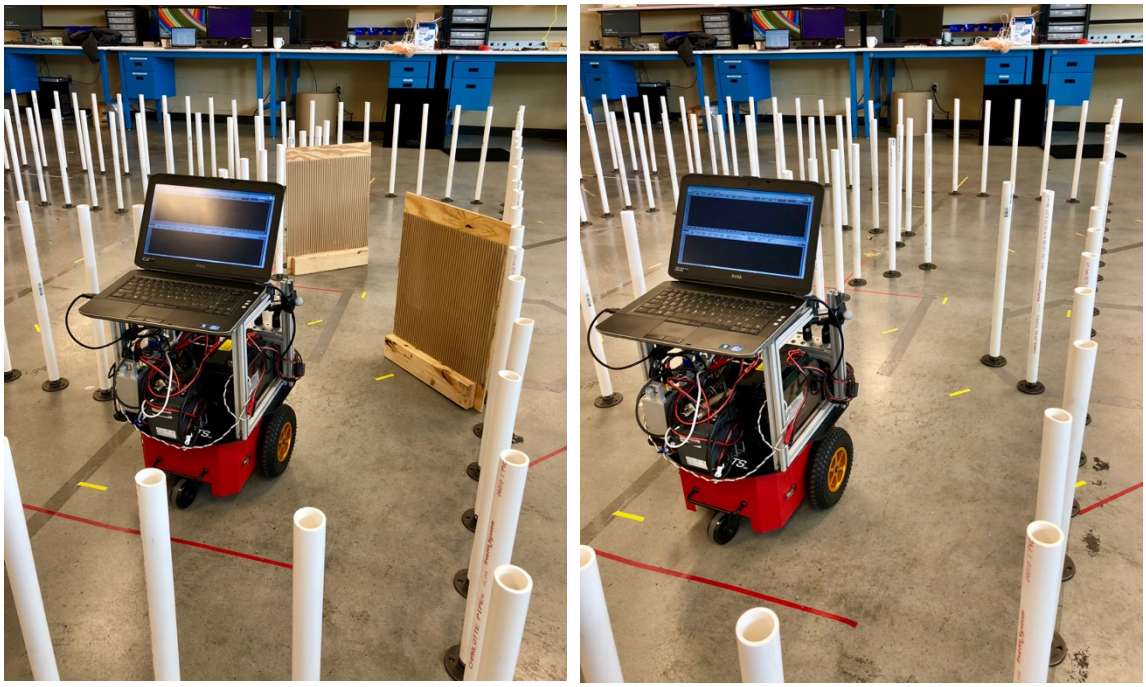

Fig. 7.15: Square corridor with obstacles experimental set.

For the square corridor with two panel obstacles, the radar testbed was placed in the same forward position as the previous experiment. The testbed moved forward with very minimal deviation from the centerline, and then passed through the first corner. It then moved along the vertical corridor and through the second corner successfully. After passing through the second corner, Fig 7.16, the testbed perceives the first obstacle using the right sensor, this allows it so swerve to the left and take a center position between the right side obstacle and the left wall. Immediately after guiding through the first obstacle the testbed reaches back to the centerline before noticing the second obstacle on the left sensor. This allows it to move further to the right avoiding colliding with the obstacle. As soon as the

testbed exits the second obstacle, it perceives the third corner, and turns towards it. The rest of the path is similar to the previous square corridor case.

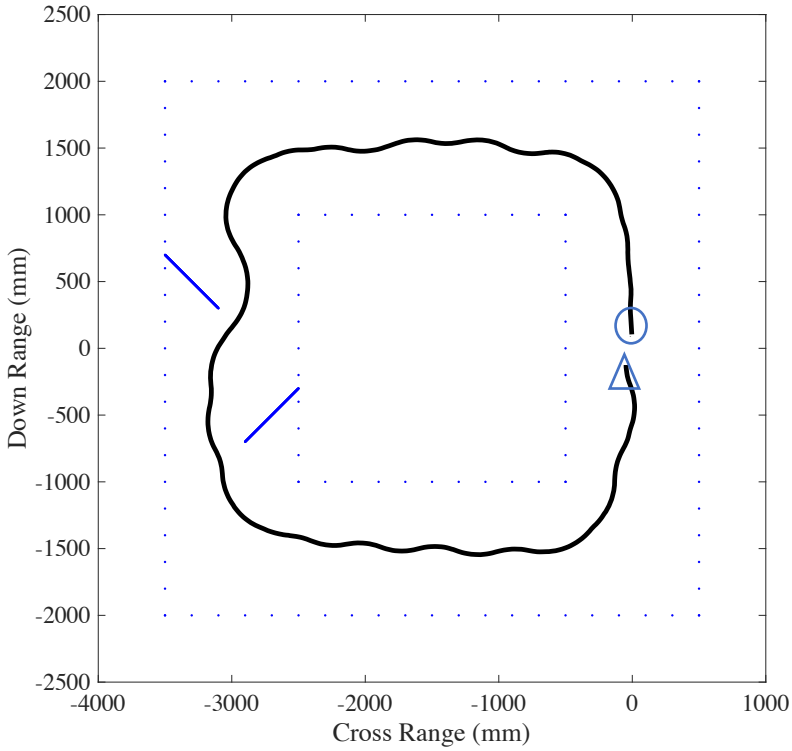

Fig. 7.16: Path of the robot in a square pole corridor with panel obstacles.

The echoic flow output of the left and right sensors is shown in Fig 7.17. After about 40 seconds into the experiment, the testbed perceives the first obstacle. This is shown in Fig 7.17 where right sensor τ, in blue, is smaller than the left sensor τ, in red. From $t = 40\ s\ to\ 45\ s$ the gap between the left and right sensor τ values is closing which indicates the robot reaching for the center position between the right obstacle and the left wall. Furthermore, between $t = 45\ s\ to\ 51\ s$ the left sensor τ becomes smaller compared to the right sensor τ, allowing the robot to exit the first obstacle and return to the center of the

corridor. The testbed then continues to slightly move to the right and passes through the second obstacle before perceiving the third corner at $t = 64\ s$.

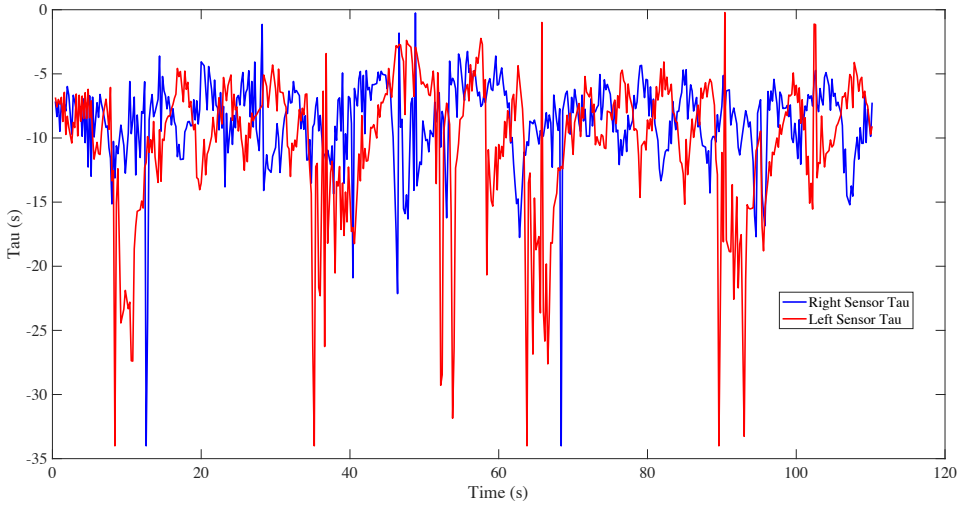

Fig. 7.17: Left and right echoic flow sensor readings for square pole corridor with panel obstacle.

Finally, the last experiment was conducted by replacing the obstacle panels with three evenly spaced poles. The space between poles is consistent with the 20 cm gap environment. Regardless of having a point target like obstacles, the testbed was able to detect, perceive and act to avoid colliding with obstacles and environment walls. Hence, completed a full successful loop around the corridor. Fig 7.18.

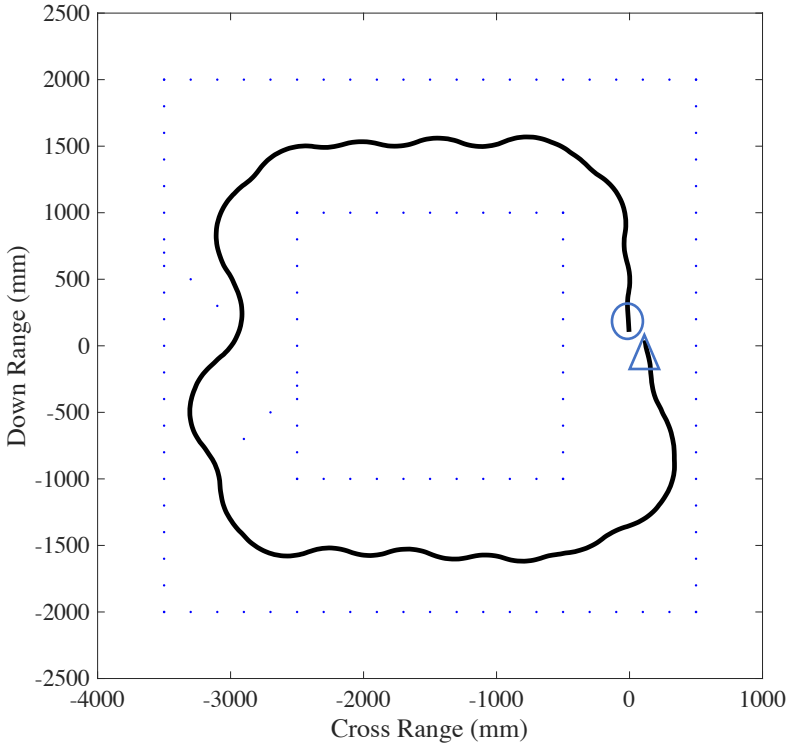

Fig. 7.18: Path of the robot in a square pole corridor with pole obstacles.

For the previous set of experiments, the testbed used an acoustic FMCW radar system that measures both range and Doppler velocity to the target. From the two measurements, echoic flow can be determined independent of robot's internal measurement system. Using the acoustic radar system provided the freedom of varying radar parameters and the ability of perceiving multiple targets from each individual beam.

Comparing the first set of experiments using the robot's internal range finders, to the second set of experiments using the developed acoustic radar testbed yielded an essential outcome. The first set showed that for a continuous wall environment, a single range outcome is sufficient in determining whether a target is present and hence moving away

from it. However, with an environment that consists of multiple targets as shown in the second set of experiments, it is not possible to use the robot's internal range sensor to find multiple targets and to distinguish the closest echoic flow measurement, along with the lack of measuring the relative velocity to each target. However, when using the acoustic FMCW radar, multiple echoic flow measurements form multiple targets were possible to acquire, and a decision to use the lowest time to contact from each beam was possible, resulting in the ability to guide through a complex environment that consists of multiple targets.

7.2 Aperture Traversal

Another way of using echoic flow for autonomous guidance was performed when guiding the robotic platform towards and through apertures. A set of experiments were conducted in [37] to show a robotic platform steering through apertures using a deterministic control approach as described in section 2.4. Here, the same experiment set is used to achieve aperture traversal through the use of echoic flow as a bio-inspired guidance approach.

7.2.1 Experimental Setup

For the aperture traversal experiments, multiple environments were built. This includes a square room with a single aperture in the middle, a square room with aperture to the side, and a square room with sloped walls leading to the aperture. Also, multiple apertures in a multiroom environment were built.

For each environment two methods of building the environment is applied. Rectangular plywood walls, and individual evenly spaced PVC poles. For the rectangular plywood walls, the robot's internal sensors are used for perception; while for the PVC poles environment, the acoustic radar testbed is used.

The perception action rules to guide the robot towards an opening in the room and move through the aperture is the same as the action rules performed when navigating through corridors in the previous section. While the task objective for this section was to steer between obstacles, and the strategy to achieve this was chosen to be "steer away from the direction with shortest time to collision". This task objective should lead the robot to always travel between objects and tend to center itself between them, eventually leading the robot to traverse the wall opening, i.e. aperture traversal.

7.2.2 Experimental Results

7.2.2.1 Using Robot's Internal Sensors

First, A 3×3 m room with a 1m aperture in the middle of the lower wall is set as shown in Fig 7.19. The green panels are absorbent foam to minimize reflections from objects beyond the aperture.

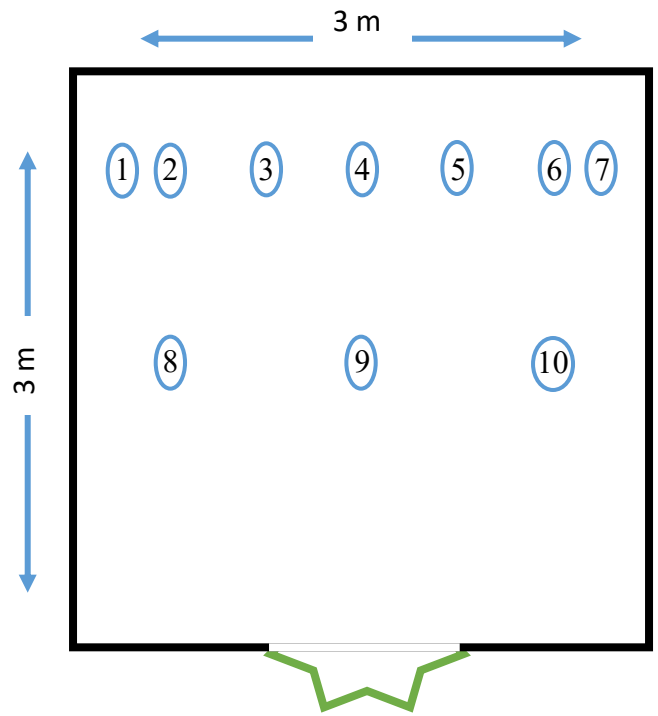

Fig. 7.19: Square room with aperture experimental set.

The robot was placed in 10 different starting positions all facing the lower wall, Fig. 7.19, where it starts from the upper left at position 1, all the way to the lower right at position 10. The path traveled by the robot in these 10 trails is shown in Fig. 7.20. The robot steers to the center of the room to balance the two echoic flow values gained from the two sensors. Then when the robot perceives the aperture it navigates towards it with an angle relative to its current location. For the far left and right starting points, the robot turns sharply to reach the center of the room, whereas the steering duration is minimal for the close to the middle starting positions.

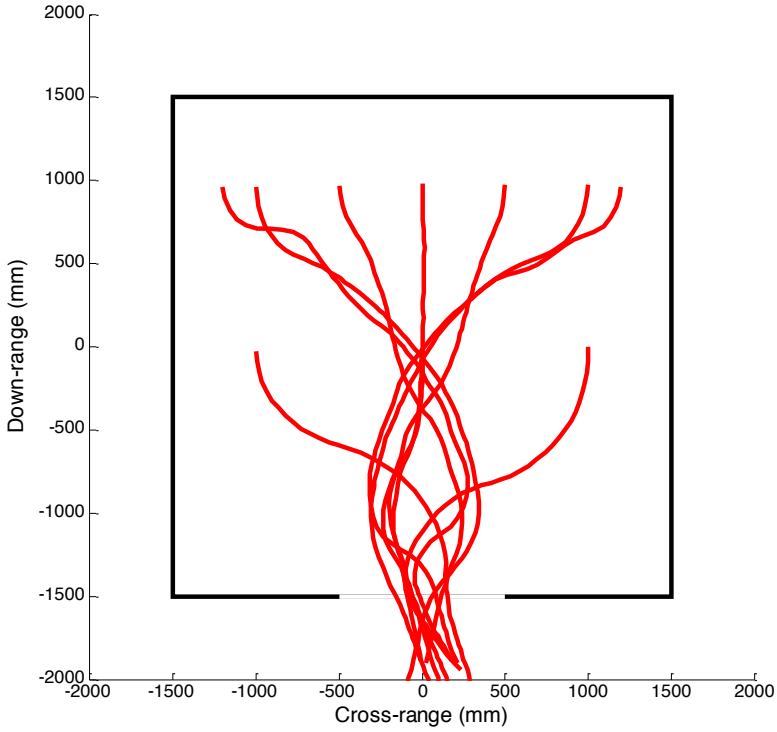

Fig. 7.20: Path of the robot in a square room with aperture in the center.

Fig. 7.21 shows the echoic flow measurements in the two sensors for the case where the robot started in the most left upper corner at 1 in Fig. 7.19. When starting, the echoic flow value of the right sensor is smaller compared to the left sensor. This guided the robot to steer sharply to the left to avoid colliding with the left wall. At $t = 7s$ the right sensor perceives the aperture for the first time, and the robot turns to the right. At $t = 11{,}17{,}24\ s$ the robot keeps perceiving the aperture and navigates towards it until it starts passing through the aperture at $t = 30\ s$ with the two sensor measurements reaching the highest time to collision.

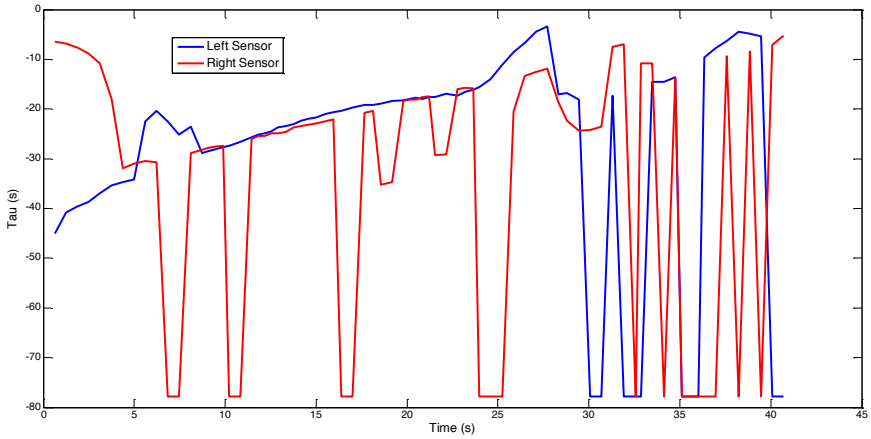

Fig. 7.21: Left and right echoic flow sensor readings for square room with aperture.

The second experiment is done by changing the location of the aperture to be in the left corner. The robot was placed in 5 different starting positions all facing the lower wall. As it shown in Fig 7.22, the robot starts steering to the center of the room, until it perceives the aperture, and navigates towards it.

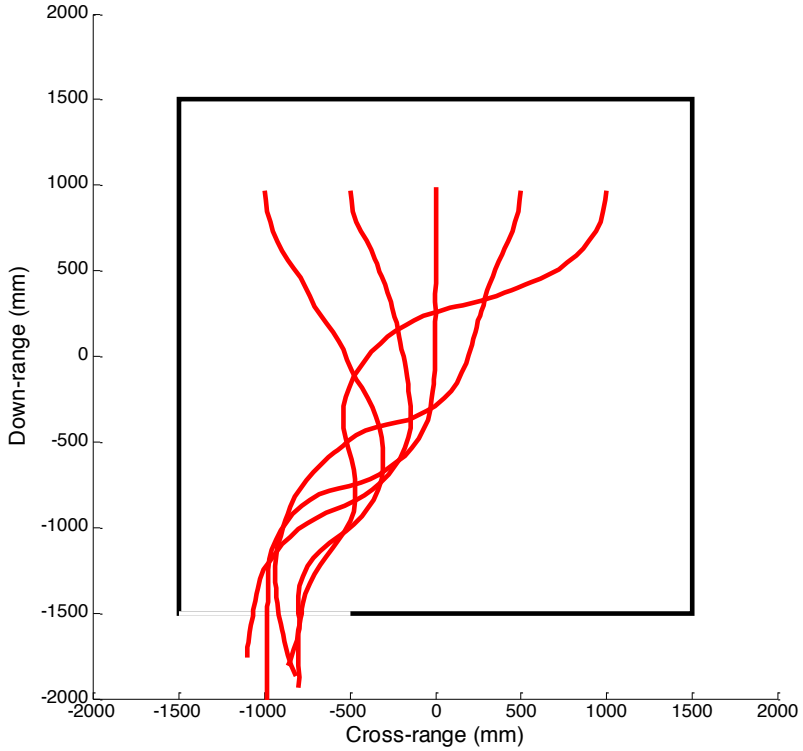

Fig. 7.22: Path of the robot in a square room with aperture in the left.

Finally, the third experiment is done by sloping the walls 45° towards the aperture. 7 different starting positions all facing the lower wall were conducted, and the robot also starts to navigate to the center of the room before perceiving the 45° sloped walls. Which causes the robot to turn slightly before returning back to the center of the room and eventually navigating through the aperture. The robots 7 paths are shown in Fig. 7.23.

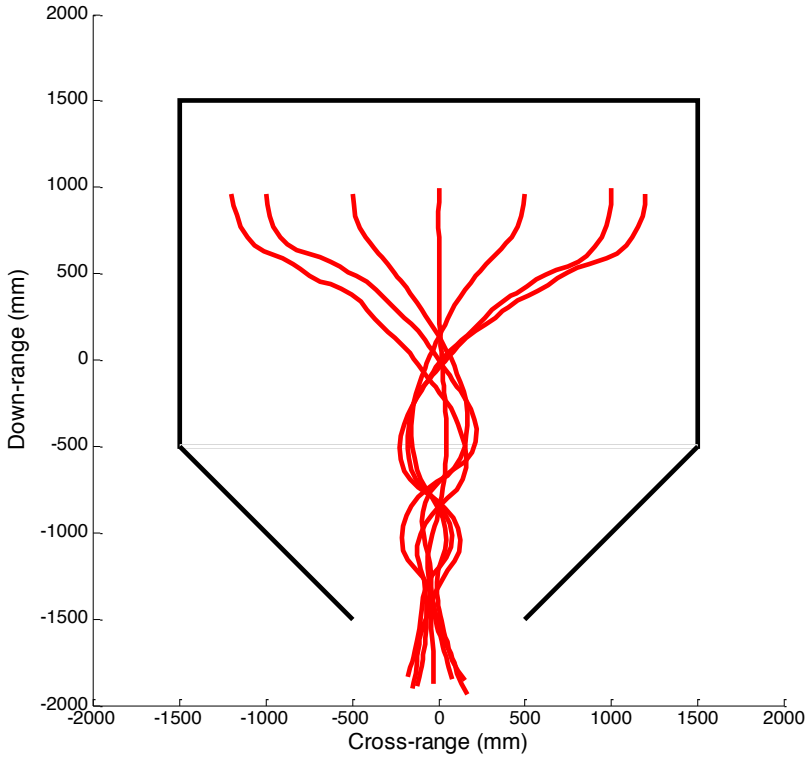

Fig. 7.23: Path of the robot in a square room with 45° walls towards aperture.

In this set of experiments, the robot was placed in the same square room with aperture in Fig. 7.20, but with a starting position that is not towards the aperture wall. In Fig. 7.24, the robot was placed in the center of the room with 3 starting angles. Facing the right, left and the aperture wall respectively. In the left and right starting angles, the robot had to rotate to avoid colliding with the wall and then it returned back to the center of the room before perceiving the aperture and then crossing through it.

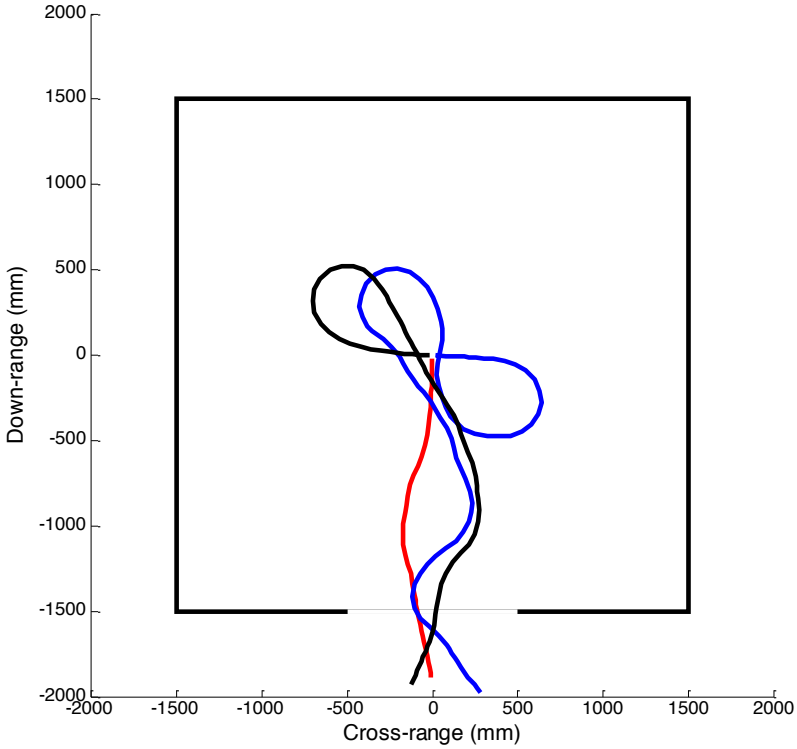

Fig. 7.24: Path of the robot in a square room with aperture and different starting angles.

The echoic flow measurements in the two sensors for the case where the robot started facing the right wall is shown in Fig 7.25. The robot starts by steering to the right since the right sensor has a slightly higher tau value compared to the left sensor. Then at $t = 18s$ the left sensor starts having a higher TTC compared to the right sensor, which steers the robot to the left until it perceives the aperture at $t = 30s$ with the right sensor. This guided the robot towards the aperture and starts navigating through it at $t = 50s$.

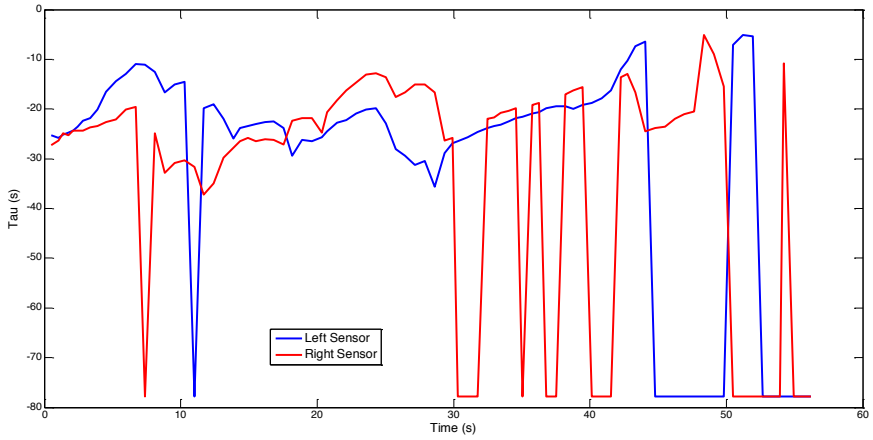

Fig. 7.25: Left and right echoic flow sensor readings for square room with aperture and robot facing the right wall.

For the second experiment, the robot was placed in the two lower corners with a 45° starting angle as shown in Fig. 7.26. When placing the robot in the right corner, it started navigating towards the center of the room, then rotated clockwise prior to perceiving the aperture. While when placed in the left corner, the robot rotated to the right to avoid the left wall and immediately perceived the aperture and navigated through it. This shows that even though both corners had the same starting angle and position, the robot navigated a different path.

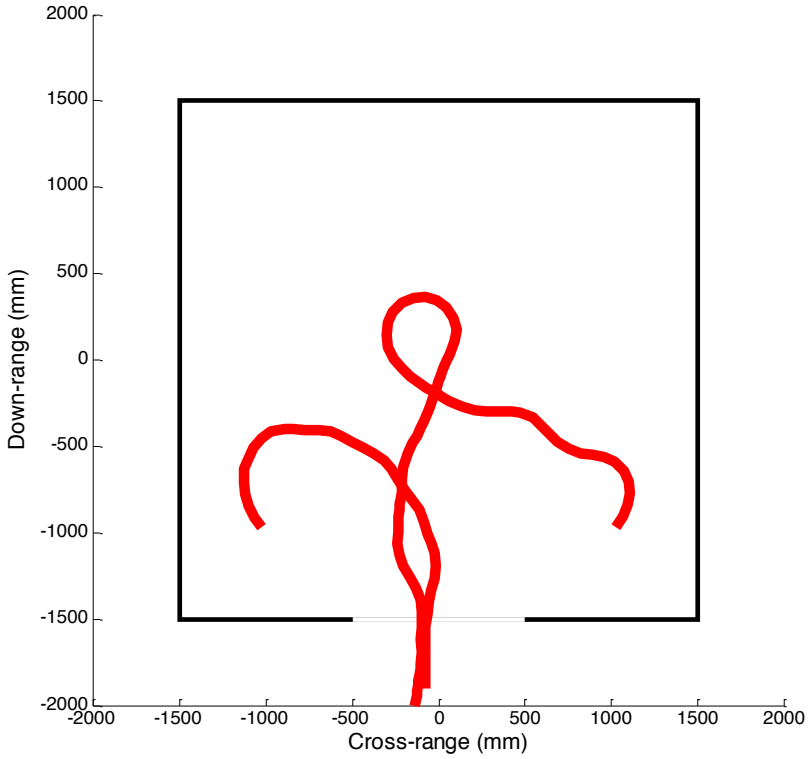

Fig. 7.26: Path of the robot in a square room with aperture and different starting angles and positions.

For a more complex scenario, two adjacent 2 × 3 m rooms were built to form a multiple aperture set. The first room opens to the second room through an aperture in the middle of the wall. While the second room has two apertures located in the left and the right of the lower wall. This is done to test the robot's ability to traverse more than one aperture by using echoic flow as a guidance method. Fig. 7.27 shows the 100 rounds of the robot's path in 5 different positions, every position is repeated 20 times. The robot started traversing the first aperture the same way as in Fig. 7.20, and then moving in the middle of the second

room before one of the two apertures is perceived, which then sets as a guide for the robot towards traversing it. Fig. 7.27 shows the one hundred runs trajectories.

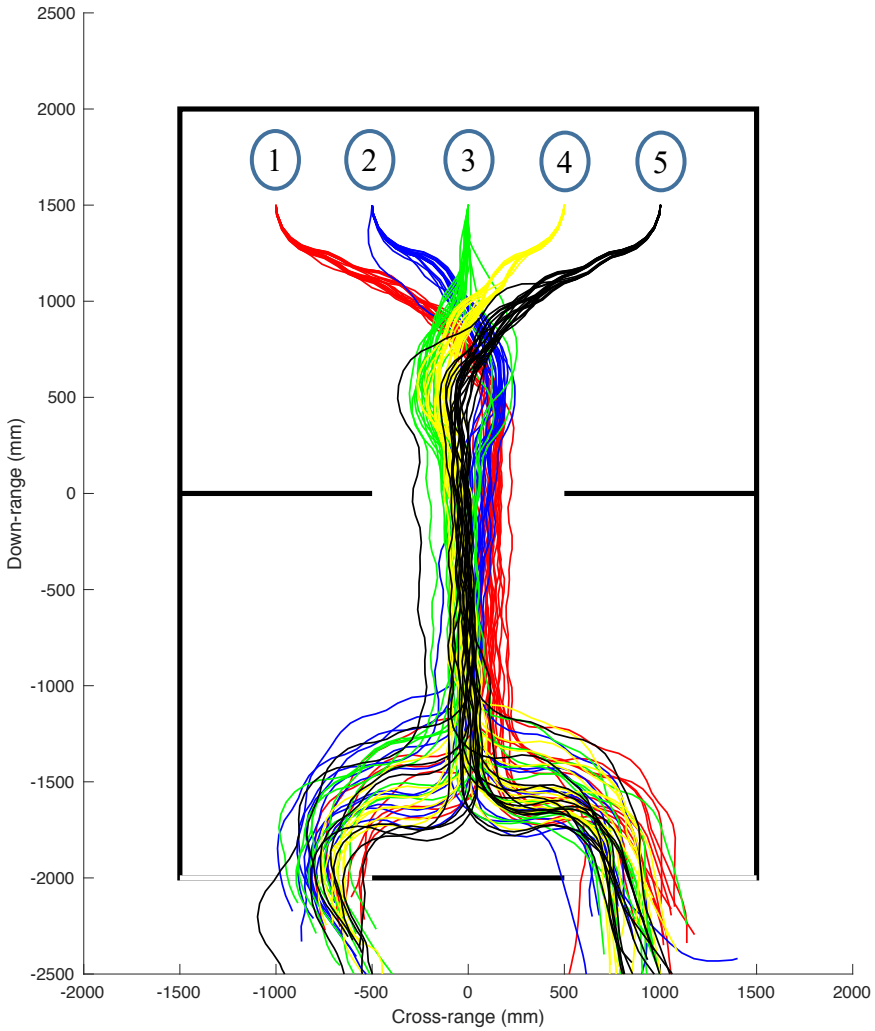

Fig. 7.27: Path of the robot in a multiple aperture room (100 runs).

A detailed calculation of the number of trials that successfully passed through the left and right apertures of the second room based on their starting position is presented in Table. 7.2, and based on the number of runs presented in Table. 7.3.

Table 7.2: Number of traverses for each aperture based on the starting position

Starting position	**Left Aperture**	**Right Aperture**
(1) Far Left	7	13
(2) Left	11	9
(3) Middle	9	11
(4) Right	7	13
(5) Far Right	8	12
Total	42	58

Table 7.3: Number of traverses for each aperture based on the number of runs

Number of Runs	**Left Aperture**	**Right Aperture**
First 25 runs	8	17
Second 25 runs	11	14
Third 25 runs	11	14
Fourth 25 runs	12	13
Total	42	58

By taking the first 25 runs, the first five runs from each starting position, from Table 7.3, the robot passed eight times to the left compared to the 17 times going through the right aperture. While if we take the First 50 runs, shown in Table 7.4, the robot passed through the left aperture 19 times compared to 31 times to the right.

Table 7.4: Number and percentage of traverses for each aperture based on the number of runs

Number of Runs	Left Aperture	% Left	Right Aperture	% Right
25 runs	8	% 32	17	% 68
50 runs	19	% 38	31	% 62
75 runs	30	% 40	45	% 60
100 runs	42	% 42	58	%58

From Table 7.4, when the number of runs increase, the percentage of traversing the left aperture increases, while the percentage of traversing the right aperture decreases. Given that traversing the left and right aperture is considered a two state problem with only two possible outcomes, it can be linked to the Bernoulli distribution of tossing a coin. Therefore, we can use the Estimator of True Probability to analyze the probability of passing the left and right apertures with a certain level of confidence.

$$p = \frac{h}{h + L} \tag{7.4}$$

From equation (7.4), the probability of obtaining heads (h), where in our case is traversing the left aperture, is equal to the number of times the robot traversed the left aperture over the number of experiments ($h + L$).

Besides, to determine the level of confidence interval of the left and right gaps, we have to set the percentage of confidence required, and calculate the standard error shown in (7.5).

$$E = Z\sqrt{\frac{p\,(1-p)}{n}} \tag{7.5}$$

where Z is the standard normal distribution corresponding to the confidence level, and p is the calculated probability of obtaining heads, and n is the number of trials.

To obtain a % 90 level of confidence, Z=1.6449. And by applying (7.4) and (7.5) to the outputs of Table 7.4, we can determine the confidence interval of each number of experiments as shown in Table 7.5.

Table 7.5: %90 Confidence Interval for each aperture based on the number of runs

Number of Runs	**Left Aperture Confidence Interval**	**Right Aperture Confidence Interval**
25 runs	$0.1665 < p_L < 0.4735$	$0.5265 < p_R < 0.8335$
50 runs	$0.2671 < p_L < 0.4929$	$0.5071 < p_R < 0.7329$
75 runs	$0.3070 < p_L < 0.4930$	$0.5070 < p_R < 0.6930$
100 runs	$0.3389 < p_L < 0.5011$	$0.4989 < p_R < 0.6611$

From Table 7.5, it is apparent that the %90 confidence interval of the robotic platform passing through the left aperture increase towards 0.5 by increasing the number of runs, while the %90 confidence interval of the robotic platform passing through the right aperture decreases towards 0.5 by increasing the number of runs. Also, the standard error in both

cases narrows with the increased runs. This provides an indication that by increasing the number of trials, the probability of passing the left and right apertures move towards half.

These outcomes from this experiment have a strong indication regarding the hypothesis that the starting position did not influence the exit aperture. Furthermore, it also shows that even when the robot tends to favor the right aperture since the outcome of the whole experiment shows that %42 of the hundred trials exit through the left aperture, compared to %58 exiting through the right aperture, the shift towards a %50 aperture traversal shown by increasing the number of trials suggests that the robot does not favor a specific aperture, and that small variations in the environment may have caused more trials passing through the right aperture.

To give a better understanding of the effect of the starting position on the path the robot takes, and how it affects the exit aperture, the middle starting position is singled out in Fig. 7.28, where the paths that exited though the left side aperture is colored in magenta, while the paths that exited through the right side aperture is colored in cyan. Note that nine paths traversed the left aperture compared to eleven traversing the right aperture.

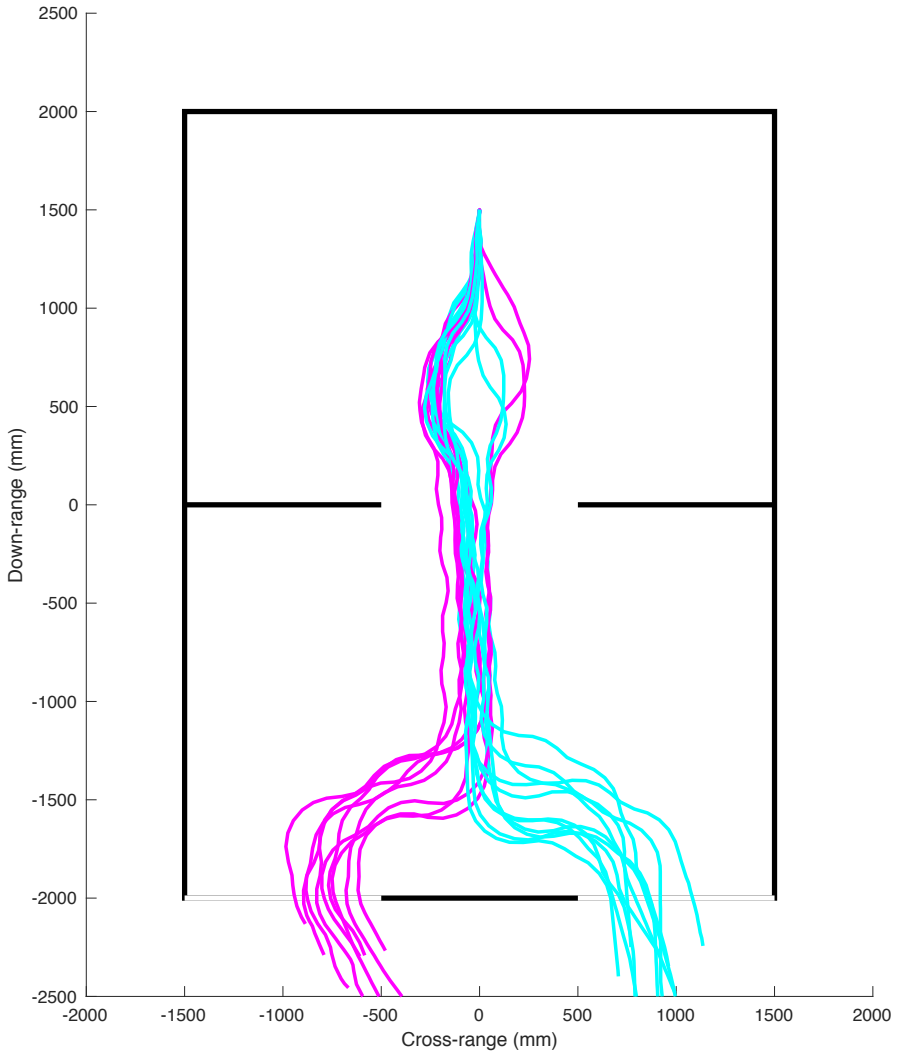

Fig. 7.28: Path of the robot in a multiple aperture room with a middle starting position.

In all twenty trials, before the robot perceives the first aperture, it turns away from the minimum time to contact, in other words, from the closest wall. Given that the starting position is in the middle of the room, theoretically, the two outer robot sensors have the same echoic flow value towards the first room's side walls. However, due to the lack of high accuracy when placing the robot in its starting position, one sensor has a marginally

smaller time to collision compared to the other sensor. This small variation leads the robot to slightly turn towards the other side before perceiving the first aperture, which allows it to turn back to the center of the room and, hence, traverse the first aperture. This action can be visible in Fig 7.28 regardless of whether the robot turned right or left at the starting position. By entering the second room, all robot paths have a steady movement by centering itself in between the second room's side walls. However, after the one meter mark, traversing half of the room's size, the paths of the robot starts to deviate from the centerline towards the left or the right aperture. It is believed to be that at this particular point, the choice to traverse either the right or the left aperture is possible based solely on which gap the robot perceives first, which is based on the slight variation in the robots' path entering this point, hence, first gap to be perceived will be traversed.

Furthermore, an advantage has been made to one side aperture in the following experiment to allow the test of whether the size of the aperture has any effect on the robot's path when traversing multiple apertures. Fig 7.29 shows the path output of an experiment where the right side aperture of the second room has been narrowed to $0.6\,m$, while the left side aperture is kept at one meter in width. Twenty trials where conducted from the center position.

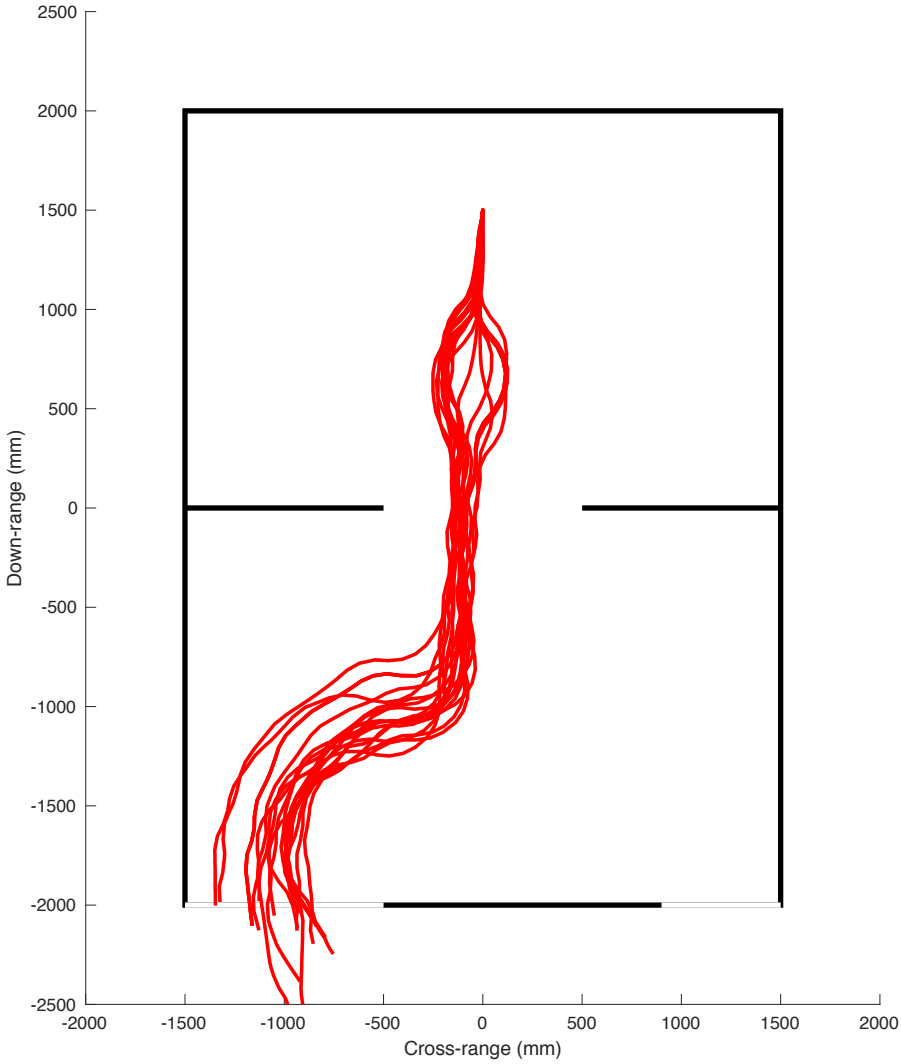

Fig. 7.29: Path of the robot in a multiple aperture room with a middle starting position and half size right aperture.

From Fig 7.29 it is seen that exiting the first room is similar to the previous experiment in Fig 7.28. However, after going through the first aperture the robot's behavior is different than previous experiment. The robot early on and around the first meter mark turns towards the wider gap and course itself through the aperture. This differs from Fig 7.28 by

perceiving the left gap earlier since the right gap is smaller and the forward wall is increased in length from the right gap's side. This led to a %100 traversal of the wider aperture.

7.2.2.2 Using the Acoustic Radar Testbed

For this section, the same experimental sets were conducted using the acoustic radar testbed instead of the robot's internal sensors. The system constants and guidance rules are consistent with section 7.1.1.2. Also, the experimental environment was built using the 20 cm spaced poles as room walls.

For the first set of experiments, a 3 by 3 m room were built, and the aperture was set to be on the center of the wall. Fig. 7.30 shows three trials of the testbed starting from the same position and moving towards the aperture. Because the bio-inspired control rule is an adaptive cycle, rather than a deterministic algorithm, the behavior of the robot differs on successive runs. In each case of the three trials, the broad behavior of the robot is the same, move away from the room walls, perceive the aperture and then traverse through the aperture, but it is clear that the path is slightly different each time. This variation arises from small differences in the starting conditions and from noise in the range and Doppler measurement leading to minor differences in the perception for each test run.

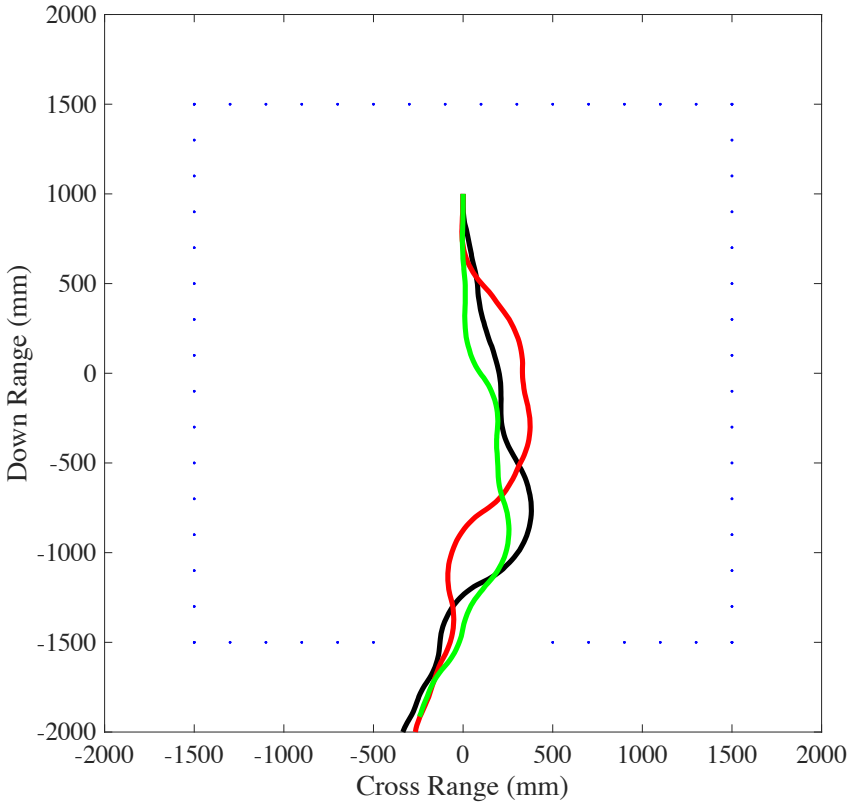

Fig. 7.30: Path of the robot in a pole square room with aperture in the center

The same experiment was repeated for 10 different starting positions. Each position had an initial condition of the testbed facing the aperture wall. Fig 7.31 shows the 10 different instances and indicates a successful guidance through the center aperture. Here, the general path followed is always the same: the radar steers he testbed towards the center of the room, perceives the aperture and then successfully traverses it.

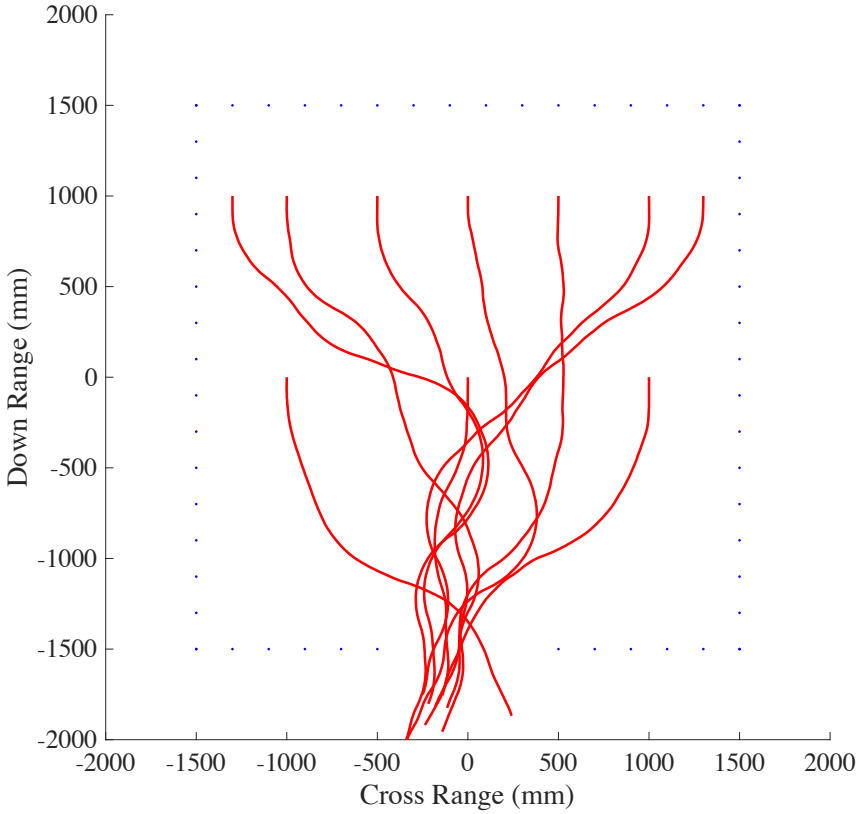

Fig. 7.31: Path of the robot in a pole square room with aperture in the center (10 trials).

The environment was made more complex by having the aperture to be on the side of the wall, and five different starting positions all facing the aperture wall. Also, the second environment was made by including slanted walls leading to the aperture. Both example results are shown in Fig. 7.32. From changing the apertures location and from introducing the slanted walls, the paths taken by the testbed has changed. Needless to say, the testbed perceives the environment and guides through the apertures successfully.

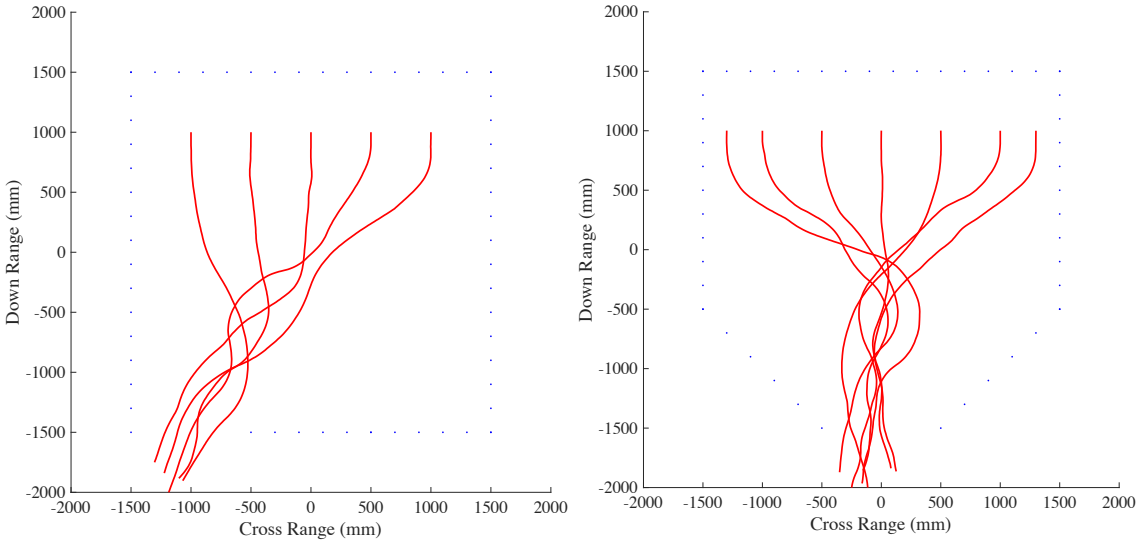

(a) (b)

Fig. 7.32: Path of the robot in a (a) square room with aperture in the left, and a (b) square room with 45º walls.

Following, the room is reverted back to the basic square room with aperture in the middle; yet, the testbed's starting position and location is changed to mark more realistic scenarios. Fig. 7.33 represent these scenarios, with the testbed completing the guidance through aperture task successfully.

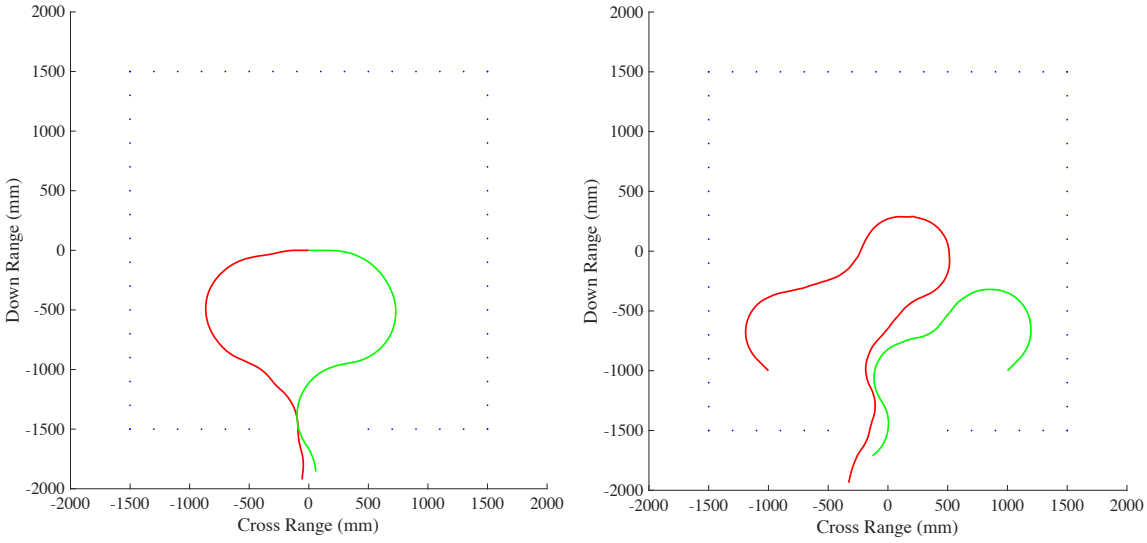

(a) (b)

Fig. 7.33: Path of the robot in a square room with aperture and different starting (a) angles and (b) positions.

Finally, a multiple room multiple aperture experiment is conducted using poles as the environment and the acoustic radar testbed to navigate that environment. The actual experimental set is shown in Fig 7.34.

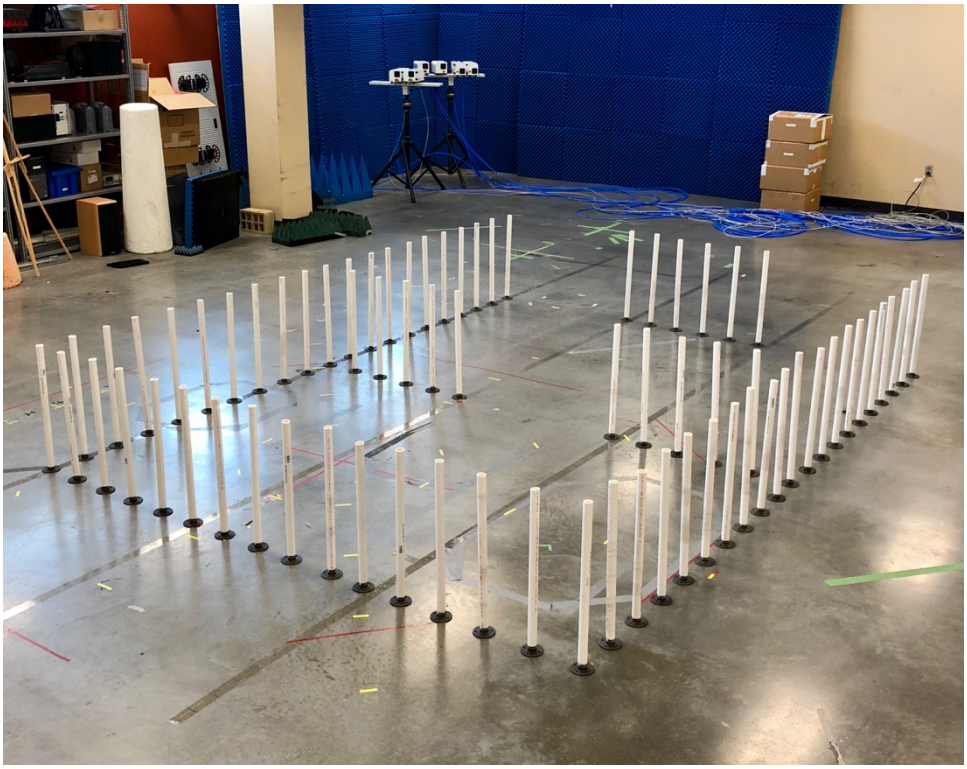

Fig. 7.34: Multiple aperture room experimental set.

Results for the final experiment is shown if Fig. 7.35. it is clear that regardless of the starting position, the acoustic radar testbed, while using echoic flow for guidance, was able to successfully guide through multiple apertures. By comparing the results of Fig 7.35 to Fig 7.27, when the robot's internal sensors were used, it is apparent that the main variance between the paths taken was the point where the testbed deviates from the center of the second room and moves to the side and towards either aperture. Here, after only moving half a meter into the second room, the testbed starts to tilt to a side and continue the movement before passing through the chosen gap. The minute differences in the echoic flow measurements extracted from range over Doppler velocity between the left and right

sensors allows for an earlier deviation towards the second aperture set. Also, out of the fifteen runs, six traversed the left aperture, while nine traversed the right aperture.

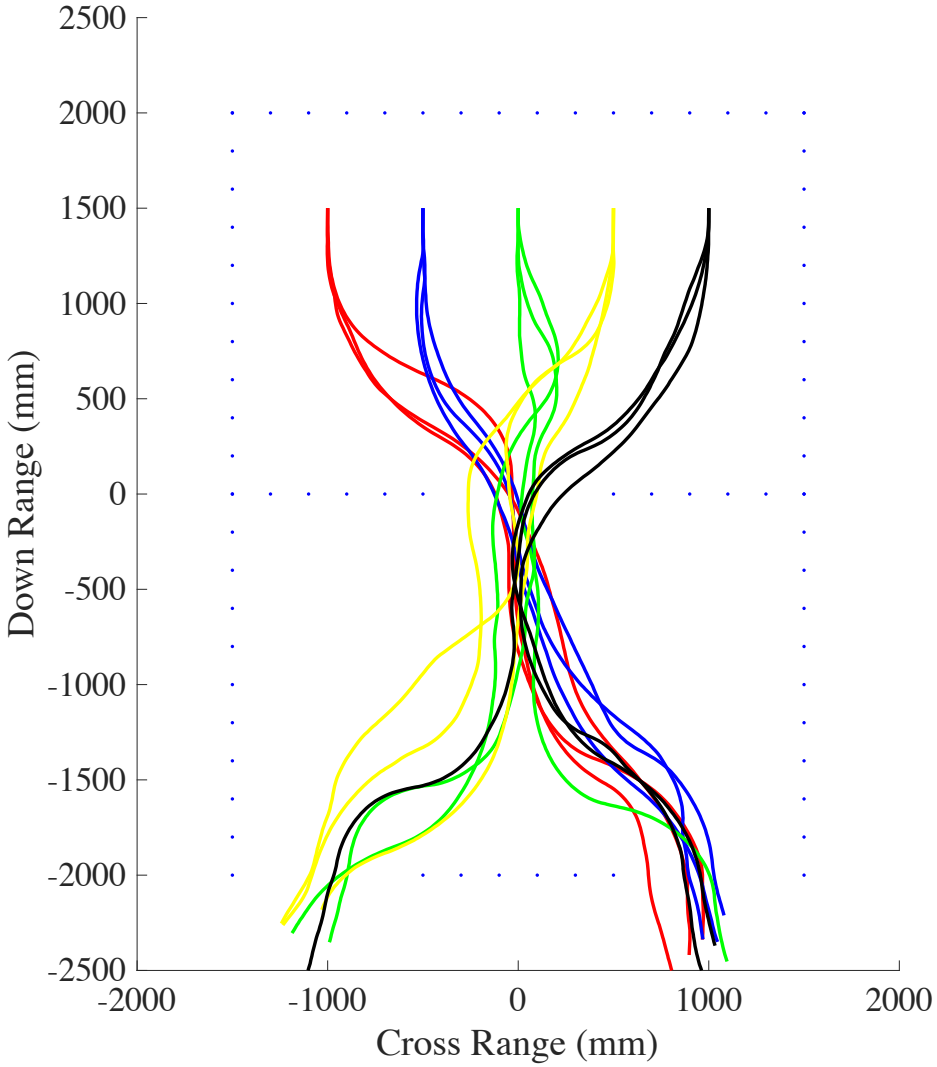

Fig. 7.35: Path of the robot in a multiple aperture room built with poles.

7.3 Conclusions

In this chapter, echoic flow has been demonstrated in a real-world scenario using synthetic echoic sensors. The robotic platform was shown capable of moving through a

straight corridor, traversing corners and avoiding obstacles. This was all achieved using very simple set of decision rules that were independent of the environment the system was placed in. In addition, the same set of rules were shown capable of enabling the robotic platform to traverse apertures regardless of the complexity of the environment and the number of apertures present. The proposed bio-inspired guidance process is computationally very simple despite the sophistication of the final robot behavior.

Chapter 8: Bat Behavior Emulation

The flight behaviors of a big brown bat flying through a corridor that is made from a series of individually spaced poles were examined in [42]. The bat has a flying speed between 2 to 6 m/s [43], and emits a frequency modulated waveform between 25 kHz and 65 kHz [44]. It can also vary its call rate, duration of call and, bandwidth to adapt to cluttered environment [45].

The experimental environment in [42] was set to two different scenarios. First, the pole spacing for the two side walls of the corridor were the same. Second, the spacings were different on each side. The conclusions from the experiment were that the bat flew along the centerline of the corridor when both sides of the corridor had the same spacing between poles, and that it shifted towards the side with sparser poles when spacings were different.

In this chapter, we replicate the set of experiments conducted in [42], first in simulation, then experimentally. A robotic platform with two FMCW acoustic radar sensors angled at 45^{o} from direction of travel are used to perceive the environment. Based on the measured echoic flow, the robot turns left and right. The outcome of both simulation and experimental work along with the methodology will be presented.

8.1 Experimental Test Setup

For the set of experiments presented in this chapter, and simulation results, a series of individually spaced poles were set as an environment. The poles are made from PVC pipes that are one inch in diameter $\approx 2.5\ cm$ and two feet in height $\approx 60\ cm$. The poles are held vertically with the help of an 8.5 cm diameter metal base. While for simulation, each pole was simulated as a point reflector.

For both simulation and experiment, six different environments were built as shown in Fig. 8.1 The environments are solely based on varying the gap between the individual spaced poles that make the left and right walls of the corridor. Furthermore, the corridor width was set to 2 m and length was set to 5 m for the entire setup.

Table 8.1: Simulation and experiment environment setup

Environment	**Left Wall Gap**	**Right wall Gap**
(1)	20 cm	20 cm
(2)	20 cm	40 cm
(3)	40 cm	20 cm
(4)	20 cm	60 cm
(5)	60 cm	20 cm
(6)	60 cm	60 cm

From Fig 8.1 and Table 8.1, the six environments were shown to be, dense left - dense right case, with the dense side having the spacing between poles set to 20 cm. sparse left -

sparse right case, with the sparse side having a gap between the poles set to 60 cm, which is three times the size of the dense case. The four other cases are 20 cm left - 40 cm right, 40 cm left - 20 cm right, with the sparse side being twice the size of the dense side, and 20 cm left - 60 cm right, 60 cm left - 20 cm right, with the gap at the sparse side three times wider than the gap at the dense side. Note that the distance of the gap between the poles is measured to the center of the pole.

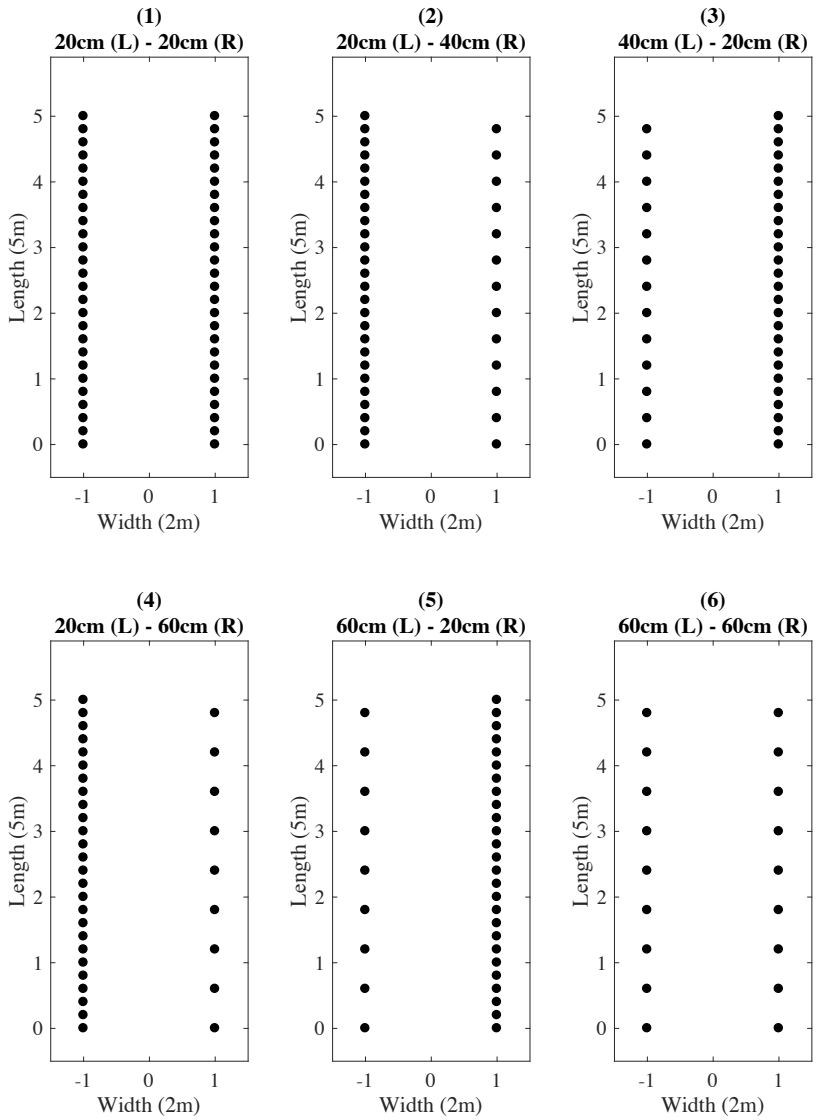

Fig. 8.1: Simulation and experimental setup for six different pole corridor environments.

To get a high accuracy measurement of the path followed by the acoustic radar testbed when moving along the corridor, the experiments were conducted in the Motion Lab located at the Advanced computing Canter for the Arts and Design, The Ohio State University. The lab is built for motion related research, and it includes 12 Vicon T40s motion capture cameras that have a positioning error of less than 2 mm [55] and can reach an optimum positioning performance of 0.3 mm. The T40s has a resolution of 4 Megapixels while capturing 2000 frames per second at full resolution [56]. The captured data is then exported using Blade 2.6. software resulting in x and y Cartesian coordinates that can be exported to MATLAB for post processing.A figure of the Motion Lab with the environment setup and the acoustic radar testbed can be shown in Fig. 8.2.

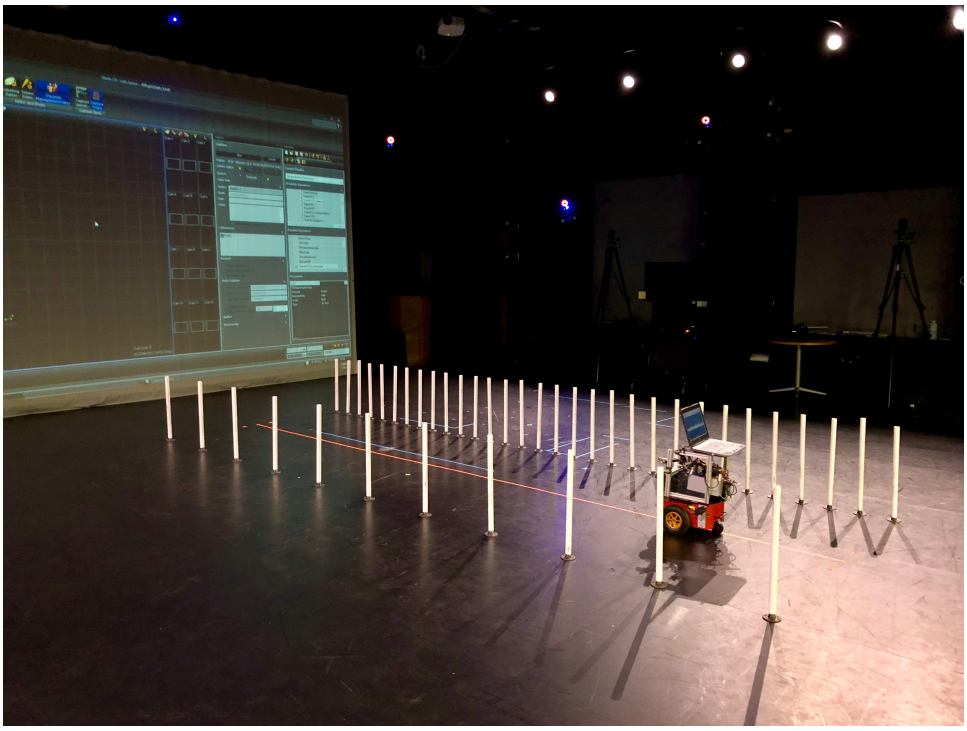

Fig. 8.2: Sparse left – dense right pole corridor experimental set at the Motion Lab.

The acoustic radar testbed consists of two microphones and two loudspeakers at $\pm 45°$ from the testbed's forward direction. Both were used to be the platform's perception when moving along the straight corridor.

For each simulation and experimental trial, the acoustic radar testbed will start at (0,0) position, and move forward towards the end of the corridor. The location of the robot will be precisely captured with the Vicon motion cameras, and then logged for post processing.

The FMCW radar parameters were matched in both simulation and experiment, Table 8.2, with the bandwidth set to 23 kHz (25 kHz – 48 kHz), and a modulation period of 0.2 s, which results in five updates per second (PRF of 5 Hz).

Table 8.2: Acoustic Triangular FMCW Radar Parameters

Parameter	**Value**
Modulation Bandwidth (ΔF)	23 kHz
Modulation Period (T_m)	0.2 s
modulation frequency (f_m)	5 Hz
Center Frequency (f_o)	36.5 kHz
Minimum Signal Overlap	%80

The range and Doppler output of each individual update is used to measure echoic flow for each individual pole illuminated by the sensor's 20 degree beam, and the minimum

time to contact from the illuminated poles is used in each beam to steer the radar testbed away from the side of smallest time to collision by using the same action rules presented in Table 7.1, and the duration turn of (7.3). Please see section 5.2 and 5.3 for more details on the acoustic radar testbed, and the use of the minimum time to collision as a perception method in section 5.4.

8.2 Simulation Results

Six simulation trials were conducted to mimic the environment setup shown in Fig 8.1. The simulation consists of a simulated robotic device that has both forward and rotational movement. The simulated robotic movement is set to simulate the actual Adept MobileRobots Inc. Pioneer 3-DX robot described in section 5.1 and used in the experiment, section 8.3.

For the simulation, the robotic forward movement is set to $0.1\ m/s$ and the rotational velocity is set to 15^{o} per second when the robot is turning, the same setting as the experimental trials.

The first simulation path is shown in Fig 8.3, where both sides of the corridor wall were set to have a dense gap of 20 cm between the poles. The simulated FMCW radar platform started from the original point (0,0) and moved forward with $0.1\ m/s$ velocity. The red cross indicates the starting point, while the blue circle represents the end point.

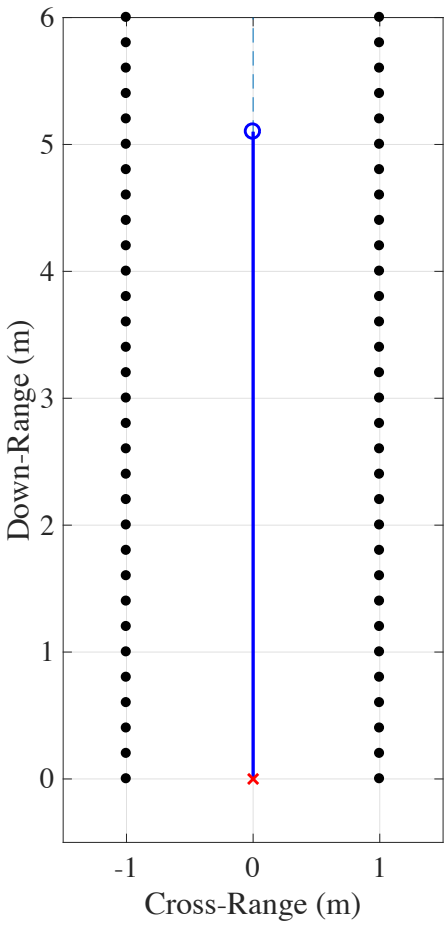

Fig. 8.3: Path followed by robotic platform in a 20 cm dense – dense case.

The path traveled by the platform had a very minimal deviation from the dashed centerline, while having a mean of -0.48 mm and a standard deviation of 0.82 mm. Table 8.3 shows mean and standard deviation of the six simulation sets.

For the second set, the right side wall increased in gap size to reach twice the size of the left wall at 40 cm. The path output is shown in Fig. 8.4.a. The robotic platform started by shifting to the right side, where the gap between poles is larger compared to the left side.

The movement of the platform is zoomed in, Fig. 8.5.b, where it is shown to be slightly oscillatory. This is due at first when the robotic platform's right side sensor returning a greater time to collision compared to the left side, which steer's it towards the right side. However, moving forward the two left and right beams perceive the two horizontally aligned poles, which requires the platform to shift back to the centerline since the tau output in the left side is now greater than the tau output of the right side. While the platform is shifting back to the left side, it then perceives the second pole in the right side, and hence, return beck to shift to the right side.

The consistent shift to the right side causes a deviation to the right of the centerline that is oscillatory in nature. The mean of the shift from the centerline is equal to 18.20 mm, while the standard deviation is calculated at 2.45 mm. This behavior can be seen in repetition along the entire experimental set.

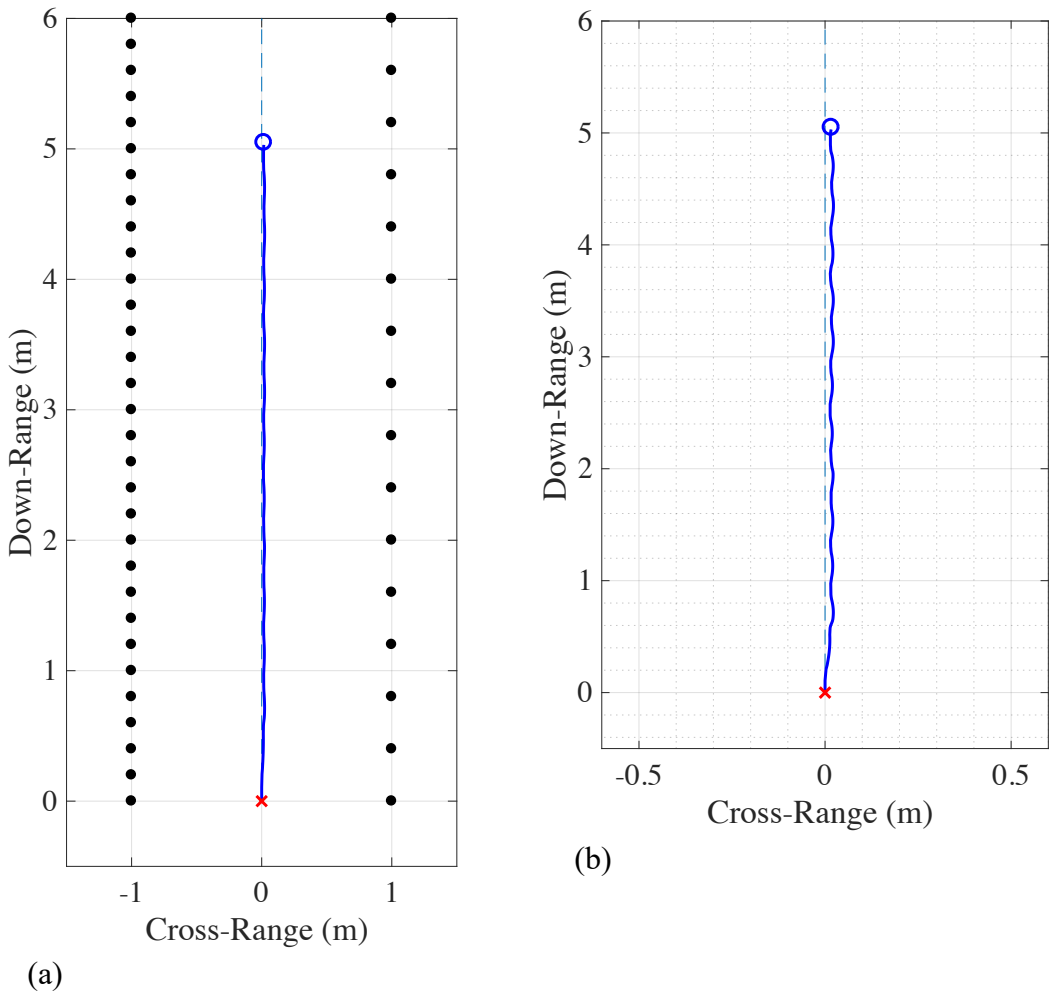

Fig. 8.4: (a) Path followed by robotic platform in a 40 cm sparse right – 20 cm left dense case. (b) Zoomed in path.

When the left side wall pole gap is increased compared to the right side. The same behavior shown in Fig 8.4 is presented, except that the shift was towards the left side since it has the increased pole gap. The mean of the shift was calculated -19.26 mm, and a standard deviation of 2.46 mm

For the third simulation set, the sparse side pole gap is set to be three times the dense side at 60 cm. Two simulations were conducted, when the right side wall of the corridor is

sparse, and when the left side wall is sparse. The path followed by the platform when the right side wall of the corridor is sparse is shown in Fig 8.5. It is observed that the robotic platform had a greater shift towards the sparse side when its gap size is three times the dense side gap size compared to the case of Fig 8.4 when the sparse side gap size is only twice the dense side gap size.

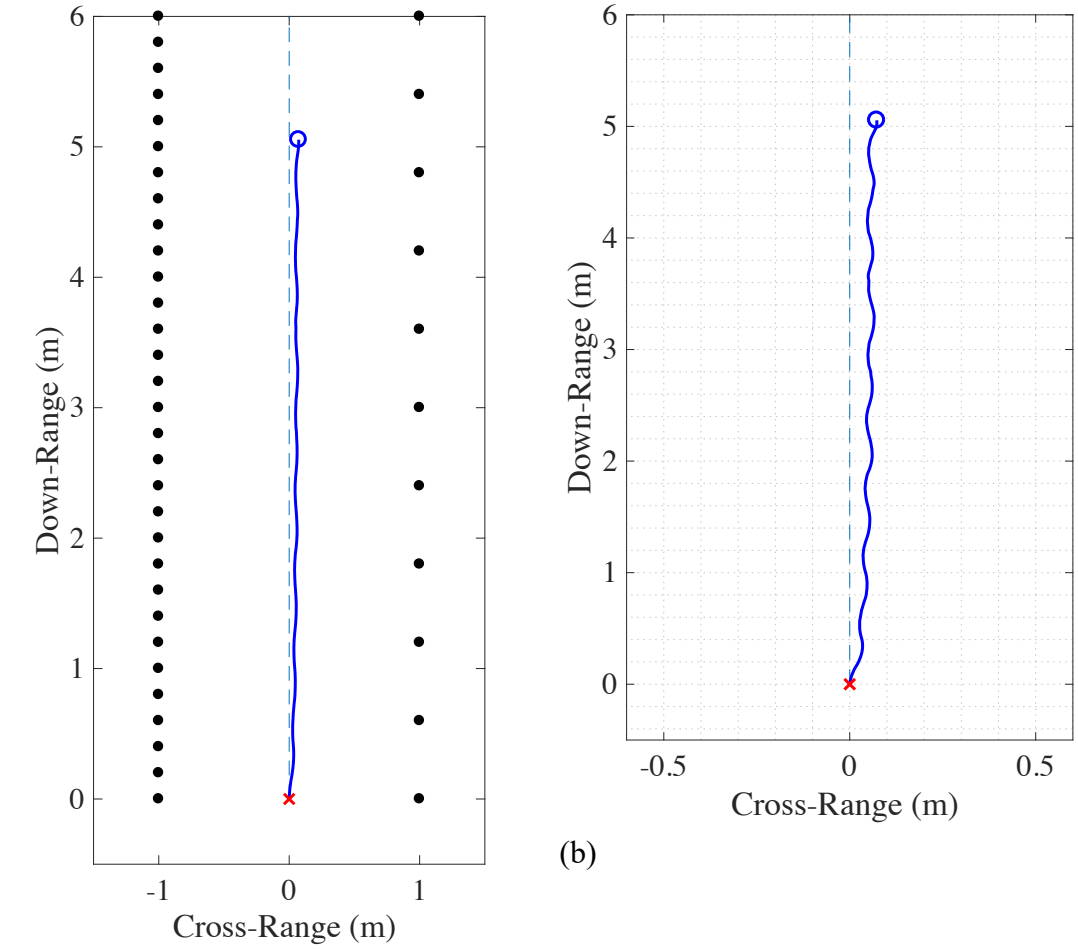

Fig. 8.5: (a) Path followed by robotic platform in a 60 cm sparse right – 20 cm left dense case. (b) Zoomed in Path.

For a better understanding of the robotic platform's movement across the simulation environment, a section of Fig 8.5 is enlarged and shown in Fig 8.6, where the down-range between 3m and 4.2m is shown. The section shows seven poles in the left side wall, and only three poles on the right side with a 60 cm gap between the three poles. The path of the platform in blue is shown moving to the right of the dashed centerline, and it is apparent that the path deviates from the center by 3.5 cm – 7.5 cm to the right. The curvy movement is presented to be based on the variation of the closest time to collision perceived from both sides of the robotic platform's sensors through the simulation.

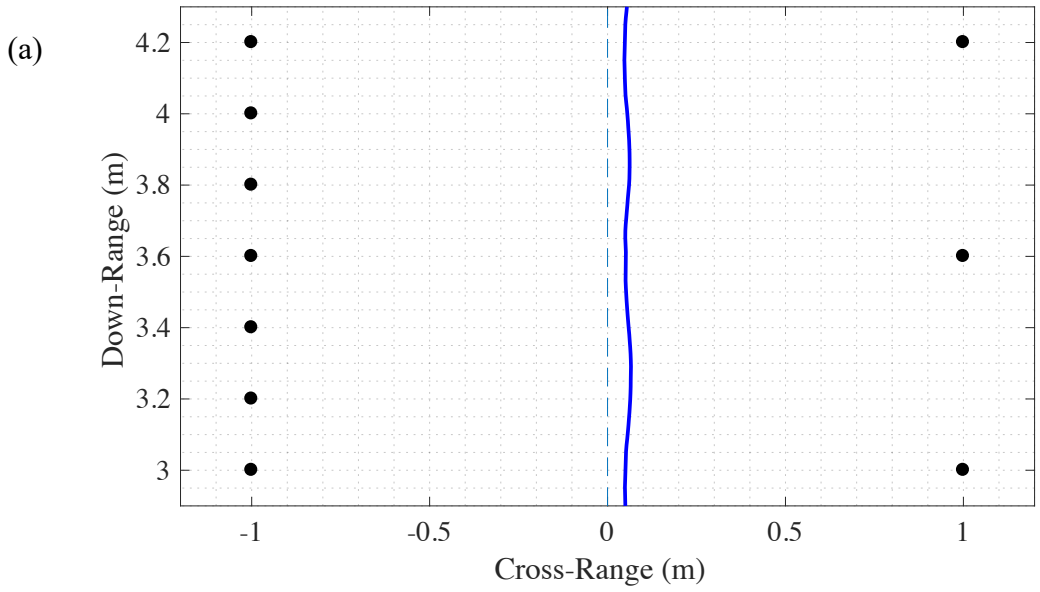

Fig. 8.6: Zoomed in path followed by robotic platform in 60 cm sparse right – 20 cm left dense case.

For instance, when the platform is located at 3 m down-range, Fig 8.7.a, blue circle, the acoustic radar sensors are perceiving both left and right poles, colored in solid red, where the left side sensor is perceiving the four poles located at 3.8 m, 4 m, 4.2 m and, 4.4

m, while the right sensor only perceiving the pole at 4.2 m resulting in smaller time to collision in the left sensor compared to the right sensor. Therefore, Fig 8.7.b, the robotic platform starts shifting to the right side until reaching the location 3.2 m, in Fig 8.7.c. Here, both poles located at 4.2 m are set to be the minimum echoic flow return. Therefore, the platform turns to the left to return to the centerline.

Fig 8.7d and Fig 8.7.e show the location of the platform at 3.3 m and 3.4 m respectively. The platform moves to the left and this causes the right sensor to perceive the pole located at 4.8 m, while the left sensor perceives the poles at 4 m, 4.2 m, 4.4m and 4.6 m. The difference in the echoic flow output from the two sensors at Fig. 8.7.e forces the platform to turn back to the right where it then perceives both left and right poles located at 4.2 as the closest targets, Fig. 8.7.f. By reaching the location 3.6 m, the platform will repeat the same cycle. Therefore, the general path movement is mainly governed by the pole location on each side.

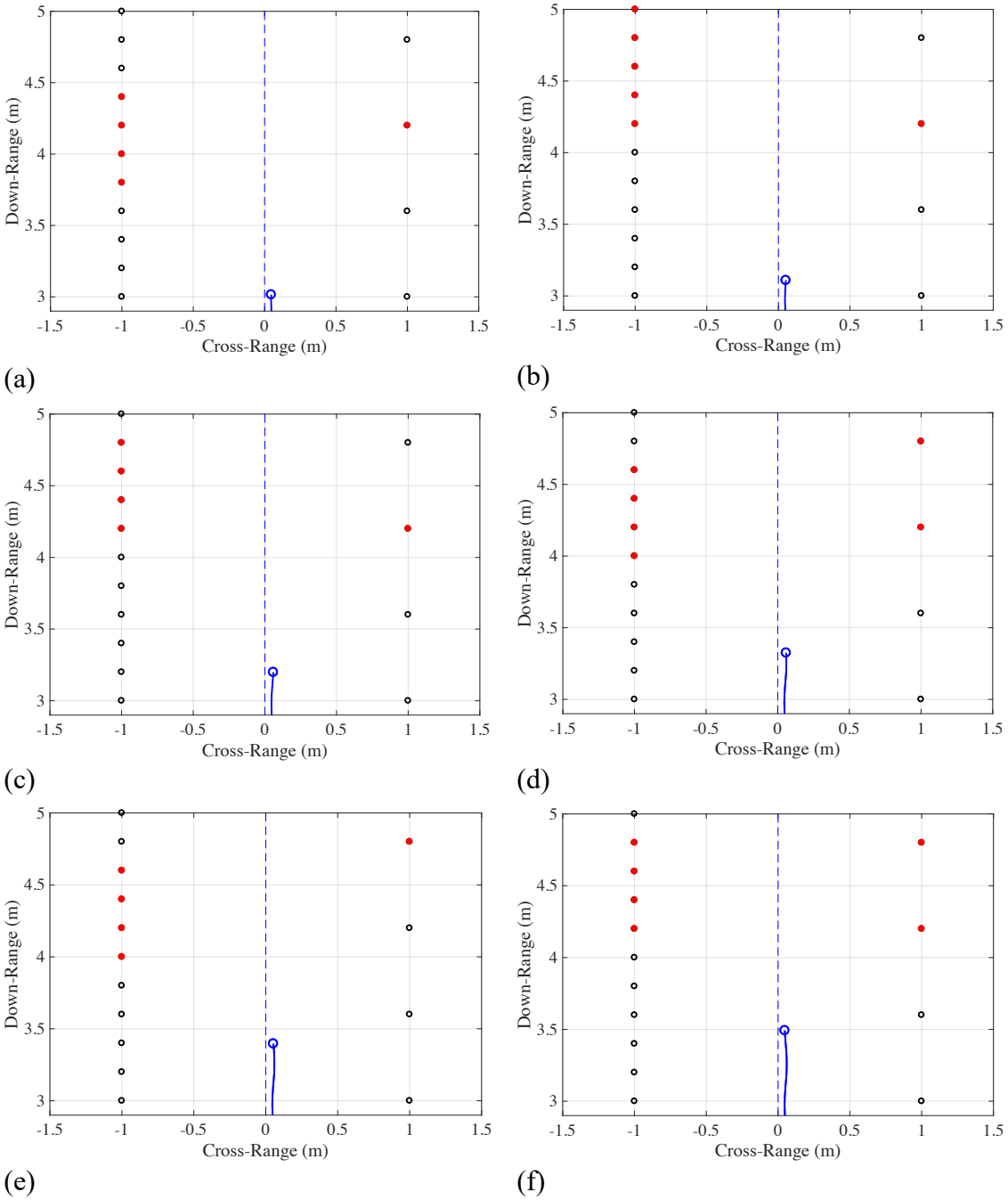

Fig. 8.7: Position of the platform in the corridor with illuminated poles at (a) 3 m, (b) 3.1 m, (c) 3.2 m, (d) 3.3 m, (e) 3.4 m and, (f) 3.5 m.

The shift of the robotic platform when traveling along the corridor is ranging from 35 mm to 75 mm along the right side of the centerline. The mean of the path is calculated at 53.58 mm, while the standard deviation is equal to 7.66 mm.

Finally, the last simulation set was accomplished by having both left and right wall gap sizes set to be 60 cm – 60 cm, representing sparse – sparse case. In this case, Fig. 8.8, the robotic platform moved across the centerline with a very minimal deviation to the left and right. However, the path's mean was calculated at 0.84 mm, while the standard deviation is calculated at 10.1 mm.

The standard deviation is larger compared to the dense – dense case of Fig. 8.3, that had a standard deviation of less than one millimeter. The increase in the standard deviation when the gap in both sides increased is caused by the increased difference in left and right tau measurements when moving through the corridor, which results in a larger oscillation around the centerline.

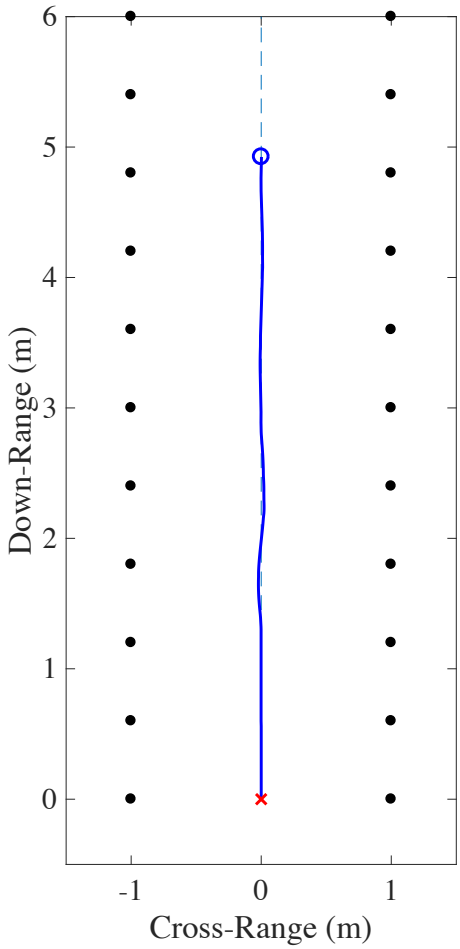

Fig. 8.8: Path followed by robotic platform in a 60 cm sparse – sparse case.

Table 8.3: Mean and standard deviation of simulation set

Environment	**Mean**	**Standard Deviation**
(1) 20 cm Left – 20 cm Right	-0.48 mm	0.82 mm
(2) 20 cm Left – 40 cm Right	18.2 mm	2.45 mm
(3) 40 cm Left – 20 cm Right	-19.26 mm	2.46 mm
(4) 20 cm Left – 60 cm Right	53.58 mm	7.66 mm

(5) 60 cm Left – 20 cm Right	-54.73 mm	8.58 mm
(6) 60 cm Left – 60 cm Right	0.84 mm	10.1 mm

It has been shown, in this section, that a deviation from the centerline when having a robotic platform equipped with an acoustic FMCW radar to guide through a straight corridor is present when the two side walls are mismatched in gap size. While a movement along the centerline in present when both wall sides have the same gap size between structuring poles.

Furthermore, when the difference between the wall gap size increases, the deviation amount increases towards the sparse side. And when both sides have the same gap size, the increase in gap size will increase the oscillation around the centerline, resulting in a larger standard deviation from the centerline. The simulation output agrees with the flight of a bat when moving through the same environment set [42].

8.3 Experimental Results

For the set of experiments presented in this section, the previous six environment scenarios shown in Fig. 8.1 and simulated in section 8.2 will be experimentally presented. Each scenario is repeated five times, resulting in thirty individual experimental paths. Each five paths from every single scenario is then post processed using interpolation to determine the mean path and show the mean and standard deviation of the deviation from the centerline.

For the first experimental set, the radar testbed was placed at the center of a 20 cm dense – dense corridor with a constant forward velocity of 0.1 m/s and a rotational angle of 15^{o} per second. This is the same parameter constants as the simulation parameters.

Fig 8.9.a shows the five independent paths colored in blue and the mean path colored in red. The red cross represents the path's starting point, while the blue circle represents the end point.

Fig 8.9.b is a zoomed in version of the five paths followed by the platform along with the mean path. The five different runs can be shown having independent paths, due to the independence of the perception of the environment and the indeterministic nature of the guidance rule, while the mean path is shown wavering around the centerline.

To quantify the mean path, Fig 8.9.c represents the histogram of the mean path's deviation from the zero centerline, along with the calculation of the mean and standard deviation. The mean path is fluctuating between -30 and 30 mm from the centerline, resulting in a very small mean of 0.004 mm from the centerline, and a standard deviation of 15.44 mm. Table 8.4 shows mean and standard deviation of the six experimental sets.

Comparing the experimental results presented in Fig 8.9 to the simulated results shown in Fig 8.4, the mean of the path followed by the robot stayed under 1 mm deviation from the centerline for both cases, while the standard deviation of the experimental trial increased to 15.44 mm compared to the 0.82 mm shown in simulation. The increase in the variation of the experimental path is due to the nature of the factors present in experimental applications like imperfections in the environment and the small variation in the returning echoic flow measurement caused by minimal variations in both range and Doppler

measurements. However, both simulation and experimental work had shown consistency in having the acoustic radar testbed move around the centerline in the 20 cm dense – dense case.

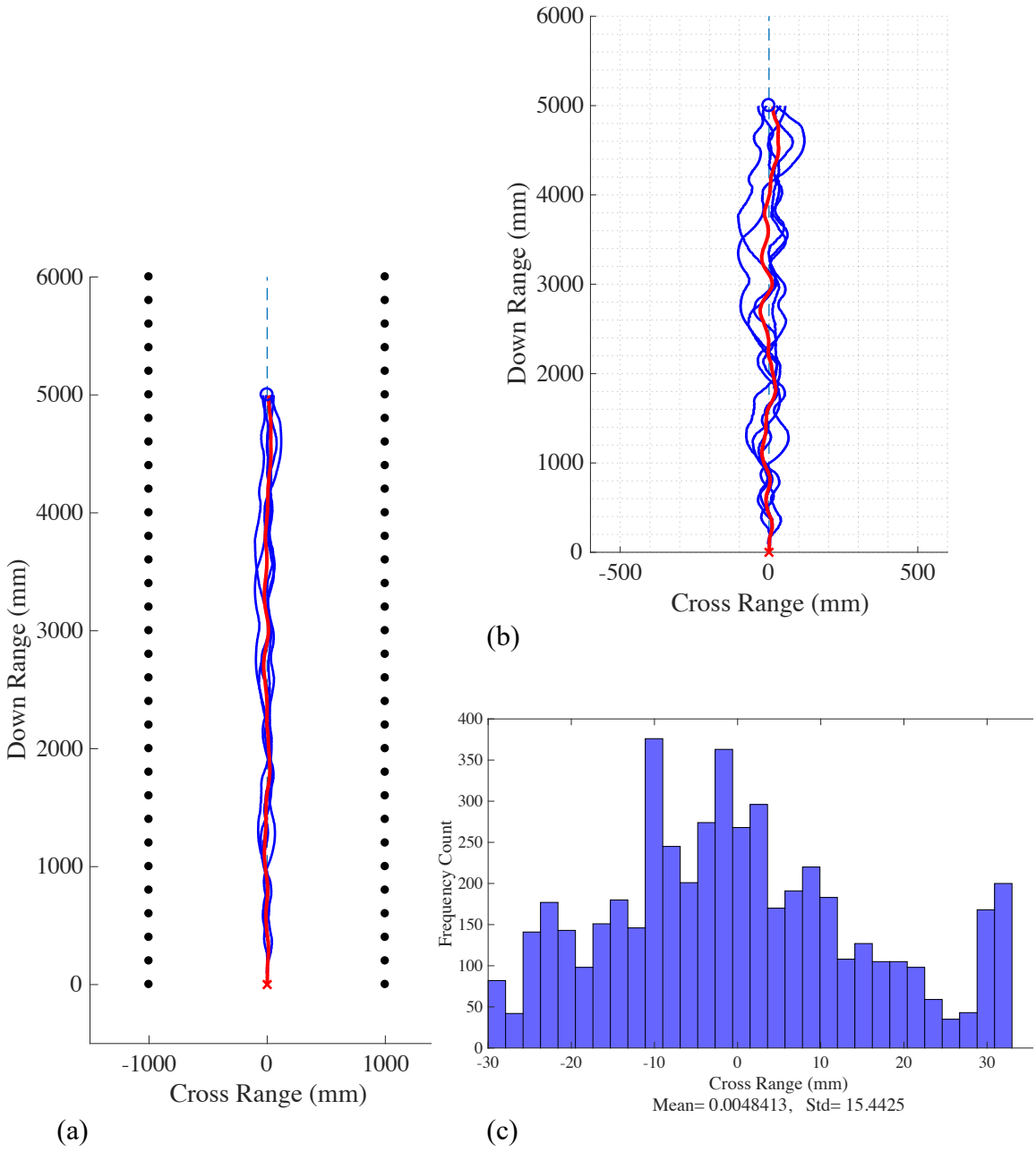

Fig. 8.9: (a) Path followed by robotic platform in a 20 cm dense – 20 cm dense case.

(b) Zoomed in path. (c) Histogram of the shift of the mean path.

For the second experimental set, the left and right side wall gaps were increased to be twice the dense side respectively. The acoustic radar testbed's constant parameters are kept the same, along with the starting position. Fig 8.10.a shows the five independent paths followed by the testbed when moving in a 20 cm left – 40 cm right case. The mean path collected from the five followed paths is also presented and colored in red. The zoomed in version of the experimental set, Fig 8.10.b, shows the paths and the mean path deviating towards the right side wall, where the gaps between the poles are twice the size compared to the left side. The deviation is quantified using a histogram Fig 8.10.c, and a clear mean deviation of 41.4 mm is calculated along with a standard deviation of 20.8 mm.

When having the left right side wall gap twice the size of the right side wall gap, a shift to the left side of the centerline across the mean path was observed, with a mean of -31.3 mm from the centerline, and a standard deviation of 21.8 mm.

While the standard deviation of the two cases presented here have almost similar results, the mean of the left side sparse case is one cm closer to the centerline compared to the mean of the right side sparse case.

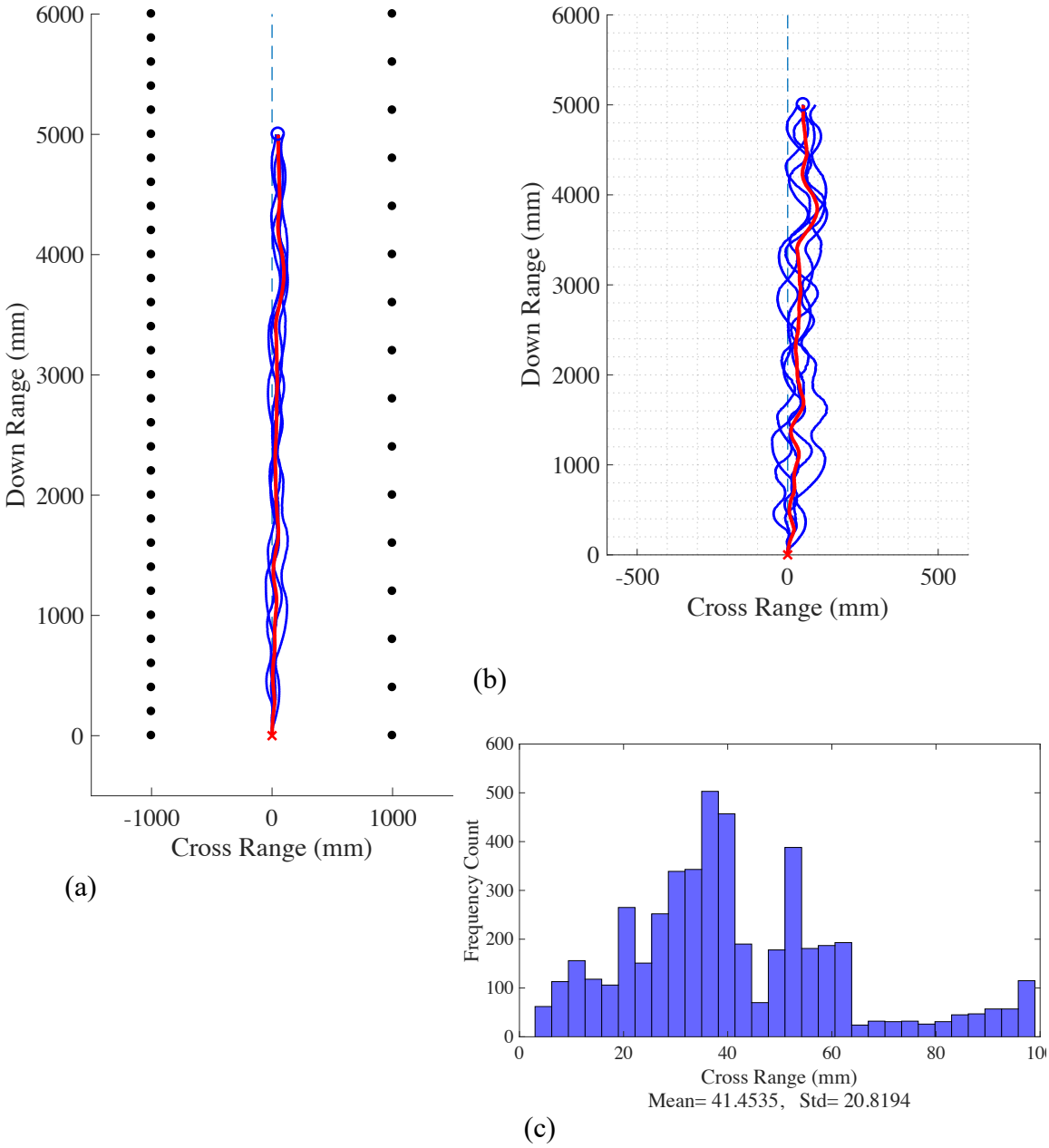

Fig. 8.10:(a) Path followed by robotic platform in a 20 cm dense – 40 cm sparse case. (b) Zoomed in path. (c) Histogram of the shift of the mean path.

For the third set of experiments, the sparse side wall gap was set to be three times the 20 cm dense side. This is consistent with the mismatch in gap size when the big brown bat was going through a sparse/dense case [42] since the sparse side was set to be three times the dense side.

Fig. 8.11 represents the case of 20 cm left – 60 cm right gap size. The five followed paths and the post processed mean path is presented along with the start and end points represented by a cross and a circle respectively.

A zoomed in version of Fig. 8.11.a is shown in 8.11.b to clearly indicate the five independent paths and the mean path's shift towards the 60 cm sparse right side. It is apparent that the four out of the five blue colored paths traveled by the acoustic radar testbed shifted immediately to the right of the centerline and stayed in that region of the corridor throughout the entire experiment, while one path slightly oscillated around the centerline for about 1.4 m before crossing to the right of the centerline and continuing a right side shift to the end of the corridor.

The mean path, in red, demonstrates a steady right side shift, and the histogram in Fig. 8.11.c quantifies the shift of the mean path between 5 and 90 mm to the right of the centerline. This resulted in a mean of 56.4 mm and a standard deviation of 21.5 mm.

Furthermore, when conducting the experiment while having the 60 cm sparse side to the left of the corridor and the 20 cm dense side to the right of the corridor, the shift to the left of the centerline is persistent along the entire corridor resulting in a mean shift to the left of the centerline equaling to -67.1 mm, and a wider standard deviation of 33.9 mm compared to 21.5 mm for the case of 20 cm left – 60 cm right shown in Fig. 8.11.

However, both experiments show an increase in the shift towards the sparse side when comparing it to the case of having a sparse side twice the size of the dense side in Fig. 8.10, which indicates a proportional relationship between the size of the gap and the shift from the centerline.

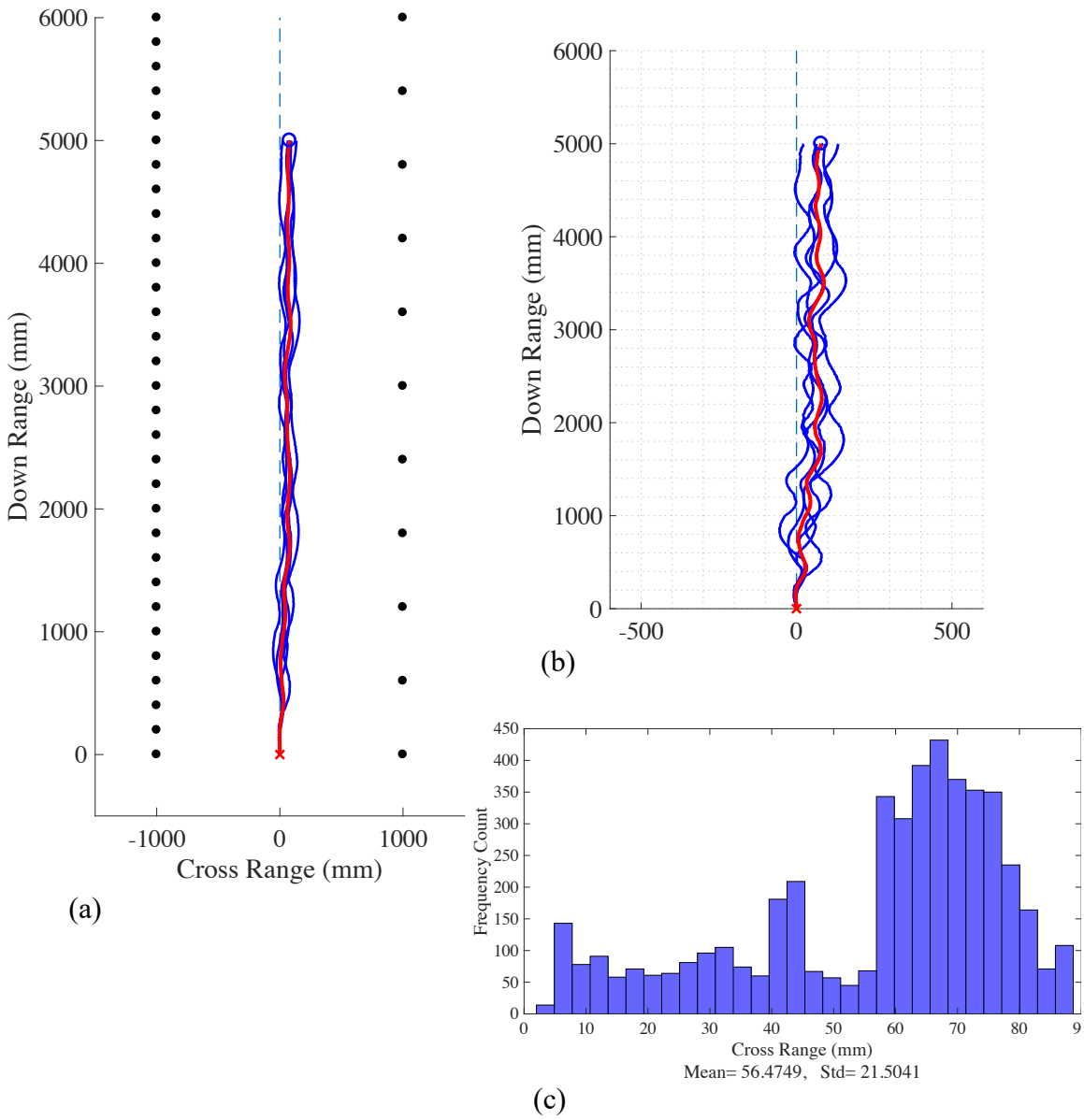

Fig. 8.11: (a) Path followed by robotic platform in a 20 cm dense – 60 cm sparse case. (b) Zoomed in path. (c) Histogram of the shift of the mean path.

Finally, the last experimental set was undertaken by having both left and right side wall gaps set to 60 left – 60 right, resulting in a sparse – sparse case. The trajectories of the five independent paths resulted in a mean path variation between -20 mm to 20 mm from the

zero centerline, with a mean slightly shifted -2.5 mm to the left side. The standard deviation , however, is only 9.9 mm. Comparing the dense – dense case to the sparse – sparse case, it is apparent that dense -dense case had a smaller deviation of the mean at 0.0048 mm compared to -2.57 mm for the sparse – sparse case, while it had a slightly larger standard deviation of 15.44 mm compared to only 9.9 mm for the sparse – sparse case.

Table 8.4: Mean and standard deviation of experimental set

Environment	**Mean**	**Standard Deviation**
(1) 20 cm Left – 20 cm Right	0.004 mm	15.44 mm
(2) 20 cm Left – 40 cm Right	41.45 mm	20.81 mm
(3) 40 cm Left – 20 cm Right	-31.34 mm	21.84 mm
(4) 20 cm Left – 60 cm Right	56.47 mm	21.5 mm
(5) 60 cm Left – 20 cm Right	-67.17 mm	33.94 mm
(6) 60 cm Left – 60 cm Right	-2.57 mm	9.93 mm

8.4 Conclusions

An acoustic FMCW radar testbed has been shown capable of guiding through a straight corridor built using evenly spaced vertical poles. Both results from using a simulated acoustic radar testbed, and an actual testbed system were presented. The simulations and the actual experimental runs yielded outputs that agrees with the flight of a big brown bat going through an environment that is created with the same vertical evenly spaced poles

[42]. The findings agree with the hypothesis that when the spacings between the individual poles in the left and right walls of the straight corridor have the same size, the acoustic radar platform will move in the middle of the corridor, which is the centerline of the corridor. Whilst, if one side has a greater gap size compared to the other side, the acoustic radar testbed will shift towards the sparse side, in other words, to the side with greater gap between the poles. It is also shown through simulation and experiment that when the gap of the sparse side increases with respect to the dense side, the shift towards the sparse side also increase. These findings can be strongly linked to the bat's behavior when traveling through the same experimental set shown in [42] and suggesting that an echoic flow aided collision avoidance guidance rule yields the same outcome as an echolocating bat. Hence, an echolocating bat may be simply doing a calculation of collision avoidance.

Chapter 9: Summary and Conclusions

This dissertation has proposed advances in the development of the echoic flow theory and its guidance and control engineering applications. Dissertation conclusions and proposed future work are presented below.

9.1 Conclusions

From chapter 3, I have presented that acoustic FMCW radar has a very fine range resolution and accuracy resulted from the low speed of propagation. However, and also due to the low speed of propagation, acoustic FMCW radars could only detect close range targets unambiguously. Furthermore, the effect of a widening in the beat frequency mainlobe bandwidth is studied when measuring far range target's that are less than the maximum detectable range, where a degradation in range resolution is noticeable due to the overlap between the transmitted and received waveforms. Therefore, I conclude that acoustic FMCW is only suitable for high accuracy short range applications.

It is also shown that acoustic FMCW radars, compared to electromagnetic radars, are more likely to have high fractional bandwidth, due to the low frequency. Therefore, it was concluded that for acoustic FMCW radars with high fractional bandwidths, the response of the target is no longer the response of only the center frequency, and therefore, the narrowband assumption is not possible to maintain.

Furthermore, development of the echoic flow theory has been presented in chapter 4 and linked to the use of the output of a radar system, like range, relative velocity and Doppler velocity for coherent radars. The theory focused on the novel approach of relative range and Doppler velocity sign as a differentiator between a gap that is opening and a gap that is closing, and how it can be applied to help with the use of the time derivative of echoic flow $\dot{\tau}$ as a control parameter. Motion equations that resulted from solving the $\dot{\tau}$ second order differential equation were simulated and the cases of both stationary and moving targets were presented. While, restrictions to the novel case of target velocity greater than radar velocity were established to ensure gap closer when the target is moving away.

Also, in chapter 4, the precision of the echoic flow output τ was calculated by establishing a relationship between the precision of range and velocity measurements in a radar system, and a confirmation through simulation of the theoretical tau precision equation when using a triangular FMCW radar was presented. It is concluded that for the same signal to noise ratio, when the range measurement to a target increases, the echoic flow measurement becomes less precise, whereas if the target's velocity increases, the echoic flow measurement becomes more precise.

While in chapter 6, and by using a monostatic acoustic radar testbed that utilizes both LFM and FMCW waveforms, a series of simulations and actual experimental work with three braking scenarios were presented to approach and follow stationary and moving targets. Both simulation and real time experiments were successful in closing range and

relative velocity gaps for each trial. The novel approach of a target moving away from the radar platform is presented and results in successful gap closer.

A robotic platform, in chapter 7, using very simple set of decision rules for echoic flow guidance was shown capable of moving through a straight corridor, traversing corners and avoiding obstacles. The robotic platform was equipped with a dual monostatic acoustic FMCW radar to use for perception of the environment. The same set of rules were also shown capable of enabling the robotic platform to traverse apertures regardless of the complexity of the environment and the number of apertures present. The proposed bio inspired guidance process is computationally very simple despite the sophistication of the final robot behavior.

In chapter 8, the dual monostatic acoustic FMCW radar testbed was put to the test when moving between two evenly spaced pole walls. The straight corridor was set to have the two walls with the same gap size, and when the gap size in the two walls differ. Simulation and real time experiment concluded that when the left and right wall gaps have the same size, the platform follows a path around the centerline. While if one wall is sparse and the other wall is dense, the platform shifts towards the sparse wall, with a sift that is proportional to the difference between the dense and sparse wall gap size. These findings can be strongly linked to the bat's behavior when traveling through the same experimental set shown in [42] and suggesting that an echoic flow aided collision avoidance guidance rule yields the same outcome as an echolocating bat. Hence, an echolocating bat may be simply doing a calculation of collision avoidance.

9.2 Future Work

The development of the echoic flow theory along with simulations and real time experiments presented in this dissertation offered avenues for continuing research in the echoic flow field. Suggested future work can be motivated towards more sophisticated strategies in applying echoic flow.

For instance, flow fields can be coupled linearly, such that action based on one field can be directly linked with another. Hence, multidimensional space can be defined. By coupling flow fields, they close their gaps at the same time with a relative closing speed governed by the coupling constant. For radar systems, both range and azimuth angle are measured to form a 2D environment. Other sensory parameters, like the received signal power can be used. By coupling the echoic flow of two of the radar's output parameters, guidance towards an object in a 2D environment is possible. Therefore, future research can push towards developing the echoic flow coupling theory with respect to radar sensory perception.

Additionally, the guidance approach presented in chapter 7 can be improved to accommodate more complex guidance scenarios. This can include, moving through a series of corridors while guiding through apertures at the same time. The execution of such application will be helpful when moving through environments that are impossible for a human operator to reach.

Given that, the derivate of the echoic flow has been tested in approaching and following a moving target, other forms of controlled braking applications can be investigated when using radar systems, like car parking, flight landing on a stationary or moving object and,

ship docking. While the combination of both the derivative of the echoic flow and coupling flow fields can yield the execution of controlled braking applications in a 2D and 3D environments.

Bibliography

[1] G.E. Smith and C.J. Baker, "Echoic flow for Radar and Sonar", *Electronics letters*, vol. 48, no. 18, pp. 1160-1161, 2012

[2] G. E. Smith and C. J. Baker, "Echoic Flow for Autonomous Navigation," in *Proceedings of Radar 2012, The International Conference On Radar*, 2012.

[3] G. E. Smith, C. J. Baker, and G. Li, "Coupled Echoic Flow for Cognitive Radar Sensing," in *Proceedings of the IEEE Radar Conference 2013*, 2013, pp. 1 – 6.

[4] G. E. Smith, C. J. Baker, and G. Li, "Echoic flow for radar target interception," in *Radar (Radar), 2013 International Conference on*, 2013, pp. 520–525.

[5] D. N. Lee, van der Weel, F. R., Hitchcock, T., Matejowsky, E., & Pettigrew, J. D. "Common principle of guidance by echolocation and vision," *Journal of Comparative Physiology A*, vol. 171no. 5, pp. 563-571. 1992.

[6] D. N. Lee, J. a Simmons, P. a Saillant, and F. Bouffard, "Steering by echolocation: a paradigm of ecological acoustics," *Journal of comparative physiology. A, Sensory, neural, and behavioral physiology,* vol. 176, no. 3, pp. 347–54, Mar. 1995.

[7] D. N. Lee, B. Shaw, J. Farber, and J. Kennedy, "General Tau Theory: evolution to date," *Perception*, vol. 38, pp. 837–859, 2009.

[8] D. N. Lee, “The optical flow field: The foundation of vision,”. *Philosophical transactions of the Royal Society of London: Series B. Biological Sciences,* vol. 290 no. 1038, pp.169-178, 1980.

[9] D. N. Lee, Young, D. S., & Rewt, D. “How do somersaulters land on their feet?,” *Journal of Experimental Psychology: Human Perception and Performance*, vol. 18 no. 4, pp. 1195. 1992

[10] M. Vespe, G. Jones, and C. J. Baker, “Diversity Strategies: Lessons from Natural Systems,” in *Principles of Waveform Diversity and Design*, M. C. Wicks, E. L. Mokole, S. D. Blunt, R. S. Schneible, and V. J. Amuso, Eds. SciTech, 2010, pp. 25 – 50.

[11] M. Vespe, G. Jones, and C. J. Baker, “Lessons for Radar: Waveform diversity in echolocating mammals,” *IEEE Signal Process. Mag.*, vol. 26, no. January 2009, pp. 65–75, 2009.

[12] G.W. Stimson, “Introduction to Airborne Radar”, *SciTech Publishing Inc*., 1998.

[13] M. A. Richards et al, “Principles of Modern radar: Basic principles,” *SciTech Publishing Inc*., 2010.

[14] G. E. Smith, S. Alsaif, and C. J. Baker, “Echoic flow for cognitive radar guidance”, in *Proceedings of the 2014 IEEE Radar Conference,* pp. 490 – 495. 2014.

[15] D.K. Barton, “Radar System Analysis”, *Artech House*, Dedham MA, 1976.

[16] M.I. Skolnik, “Introduction to Radar Systems,” *McGraw Hill*, 2001,

[17] S. Alsaif, G. E. Smith, and C. J. Baker, “Using cognitive radar to traverse apertures”, *IEEE 2014 International Radar Conference,* pp. 1–6. 2014.

[18] S. Alsaif, G. E. Smith, and C. J. Baker, “Echoic flow for target following and approach”, *CIE 2016 International Conference on Radar,* 2016.

[19] M.W. Holderied, G. Jones, and O. von Helversen, “Flight and echolocation behaviour of whiskered bats commuting along a hedgerow: Range- dependent sonar signal design, Doppler tolerance and evidence for ‘acoustic focussing’,” *Journal of Experimental Biology*, vol. 209, pp. 1816-1826, 2006.

[20] J.J. Gibson. “The perception of the visual world”, *Boston: Houghton Mifflin*. 1950.

[21] J.J. Gibson. “The sense considered as perceptual systems”, *Boston: Houghton Mifflin*. 1966.

[22] J.J. Gibson. “The echological approach to visual perception”, *Hillside: Lawrence Erlbaum Associates.* 1979.

[23] M. Srinivasan, M. Lehrer, W. Kirchner and S. Zhang, “Range perception through apparent image speed in freely flying honeybees”, *Visual Neuroscience*, vol. 6, no. 05, pp. 519-535, 1991.

[24] M. Srinivasan, S. Zhang, M. Lehrer and T. Collett, "Honeybee navigation en route to the goal: visual flight control and odometry”, *Journal of Experimental Biology*, 199, pp. 237-244, 1996.

[25] E. Baird, M. Srinivasan, S. Zhang and A. Cowling, "Visual control of flight speed in honeybees", *Journal of Experimental Biology*, vol. 208, no. 20, pp. 3895-3905, 2005.

[26] D.N. Lee, A. P. Georgopoulos, M. J. Clark, C. M. Craig, N. L. Port, "Guiding contact by coupling the taus of gaps," *Experimental Brain Research*. vol. 139, pp. 151-159, 2001.

[27] D. Lee, "A Theory of Visual Control of Braking Based on Information about Time-to-Collision", *Perception*, vol. 5, no. 4, pp. 437-459, 1976.

[28] K. Farid and A. Ahmed, "Bio-Inspired TauPilot for Automated Aerial 4D Docking and Landing of Unmanned Aircraft Systems", *2012 IEEE/RSJ International Conference on Intelligent Robots and Systems*. pp. 480-487, 2012.

[29] Z. Zhang, P. Xie, O. Ma. "Bio-inspired trajectory generation for UAS perching," *IEEE/ASME International Conference on Advanced Intelligent Mechatronics,* pp. 997–1002. 2013.

[30] Z. Yang, F. Zhou, and L. Ping, "A bio-inspired collision-free 4D trajectory generation method for unmanned aerial vehicles based on tau theory", in *proceedings of the 34th Chinese Control Conference (CCC)*, pp. 6961-6968, 2015.

[31] M. T. Alkowatly, V. M. Becerra, and W. Holderbaum. "Bioinspired autonomous visual vertical control of a quadrotor unmanned aerial vehicle", *Journal of Guidance, Control, and Dynamics*. vol. 38, no. 2, pp. 249–262, 2015.

[32] G. Dedes and A. Dempster, “Indoor GPS positioning - challenges and opportunities,” in Vehicular Technology Conference, 2005. VTC-2005- Fall. 2005 IEEE 62nd, vol. 1, pp. 412–415, 2005.

[33] S. Park, R. Saegusa, and S. Hashimoto, “Autonomous navigation of a mobile robot based on passive RFID,” *in Robot and Human interactive Communication, 2007. RO-MAN 2007. The 16th IEEE Symposium on*. pp. 218-223, Aug 2007.

[34] S. Fu, Z.-G. Hou, and G. Yang, “An indoor navigation system for autonomous mobile robot using wireless sensor network,” *in Networking, Sensing and Control, 2009. ICNSC'09. International Conference on,* pp. 227–232, 2009.

[35] G. Tuna and K. Gulez, “Aided navigation techniques for indoor and outdoor unmanned vehicles,” *in New Technologies, Mobility and Security (NTMS), 2012 5th International Conference on*, pp. 1 –4, 2012.

[36] M. Mariappan, C. C. Wee, K. Vellian, and C. K. Weng, “A navigation methodology of an holonomic mobile robot using optical tracking device (OTD),” *in TENCON 2009 -2009 IEEE Region 10 Conference*, pp. 1–6, 2009.

[37] B. Gardiner, S. A. Coleman, T. M. McGinnity, and H. He, “Robot control code generation by task demonstration in a dynamic environment,” *Rob. Auton. Syst.*, vol. 60, no. 12, pp. 1508–1519, 2012.

[38] R. Lopez-padilla, R. Murrieta-cid, and S. M. Lavalle, “Optimal Gap Navigation For A Disc Robot,” *Springer Tracts Adv. Robot.*, vol. 86, pp. 123–138, 2013.

[39] M. Mujahed, D. Fischer, and B. Mertsching, “Safe Gap based (SG) reactive navigation for mobile robots,” in *2013 European Conference on Mobile Robots*, pp. 325–330, 2013.

[40] E. Ugur and E. Sahin, “Traversability: A Case Study for Learning and Perceiving Affordances in Robots,” *Adapt. Behav.*, vol. 18, no. 3–4, pp. 258–284, 2010.

[41] "JHU Batlab", *Batlab.johnshopkins.edu*, 2018. [Online]. Available: http://batlab.johnshopkins.edu.

[42] M. Warnecke, W. Lee, A. Krishnan and C. Moss, “Dynamic Echo Information Guides Flight in the Big Brown Bat”, *Frontiers in Behavioral Neuroscience*, vol. 10, 2016.

[43] B. Falk, L. Jakobsen, A. Surlykke and C. Moss, "Bats coordinate sonar and flight behavior as they forage in open and cluttered environments", *Journal of Experimental Biology*, vol. 217, no. 24, pp. 4356-4364, 2014.

[44] A. Surlykke and C. Moss, "Echolocation behavior of big brown bats,Eptesicus fuscus, in the field and the laboratory", *The Journal of the Acoustical Society of America*, vol. 108, no. 5, pp. 2419-2429, 2000.

[45] A. Surlykke, K. Ghose and C. Moss, "Acoustic scanning of natural scenes by echolocation in the big brown bat, Eptesicus fuscus", *Journal of Experimental Biology*, vol. 212, no. 7, pp. 1011-1020, 2009.

[46] D. Barras, F. Ellinger, and H. Jäckel, “A comparison between ultra-wide-band and narrow-band transceivers,” *TRLabs/IEEE Wireless 2002*, pp. 211–214, Jul. 2002.

[47] G. R. Curry, “Radar Measurement and Tracking,” in *Radar System Performance Modeling*, *Second ed*. Artech House, 2001. pp. 165–193.

[48] G.R. Taylor, “An Introduction To Error Analysis”, *University Science Books*., 1997.

[49] “Series 600 Instrument Grade Ultrasonic Sensor”, *SensComp,* Livonia MI, 2014.

[50] “Avisoft Bioacoustics”, *Avisoft.com*, 2018. [Online]. Available: https://www.avisoft.com.

[51] “CompactRIO Systems - National Instruments”, *Ni.com*, 2018. [Online]. Available: http://www.ni.com/en-us/shop/compactrio.html.

[52] Adept MobileRobots, *Pioneer 3 Operations Manual*, 5th ed. Amherst NH: Adept MobileRobots, 2015.

[53] “80/20 Inc. - T-slotted aluminum framing system”, *8020.net*, 2018. [Online]. Available: https://www.8020.net.

[54] B. Mahafza, *Radar systems analysis and design using MATLAB*. Chapman & Hall, 2005.

[55] P. Merriaux, Y. Dupuis, R. Boutteau, P. Vasseur and X. Savatier, “A Study of Vicon System Positioning Performance”, *Sensors*, vol. 17, no. 7, p. 1591, 2017.

[56] “Motion Capture for Object Tracking and Robotics”, *VICON*, 2018. [Online]. Available: https://www.vicon.com/motion-capture/engineering.

[57] O. Akanyeti, I. Ranó, U. Nehmzow, S.A. Billings, “A proposal of a methodology for the analysis of robot-environment interaction through system identification,” *in proceedings of TAROS,* 2008.

[58] W. Meeussen, M. Wise, S. Glaser, S. Chitta, C. McGann, P. Mihelich, and E. Berger, “Autonomous door opening and plugging in with a personal robot,” In *Robotics and Automation (ICRA), 2010 IEEE International Conference,* pp. 729-736, 2010.

[59] W. L. Melvin and J. A. Scheer, Eds., *Principles Of Modern Radar Radar Applications*. Scitech Publishing, 2014.

[60] E. Aude, E. Lopes, C. Aguiar, and M. Martins, “Door Crossing and State Identification Using Robotic Vision,” In *8th International IFAC Symposium on Robot Control,* 2006.

[61] M. O. Franz, and H. A. Mallot, “Biomimetic robot navigation,” *Robotics and autonomous Systems*, vol. *30*, no. 1, pp. 133-153, 2000.

[62] Z. Li, P. Milgram, “An empirical investigation of a dynamic brake light concept for reduction of rear-end collisions through manipulation of optical looming”, *International Journal of Human-Computer Studies 66,* 158–172. 2008.

[63] S. Haykin, “Cognitive Dynamic Systems: Perception-action Cycle, Radar and Radio”, *Cambridge University Press*, 2012.

[64] B. R. Mahafza, “Doppler Processing,” in *Radar Signal Analysis and Processing Using MATLAB*. CRC Press, 2008. pp. 403–427.

[65] J. Wenger, “Automotive radar-status and perspectives,” in *Proc. IEEE Compound Semiconductor Integrated Circuit Symp.*, pp. 21–25, 2005.

[66] I. Gresham *et al*.,“Ultra-wideband radar sensors for short-range vehicular applications,” *IEEE Trans. Microw. Theory Tech*., vol. 52, no. 9, pp. 2105–2122, 2004.

[67] H. G. Griffiths, “New ideas in FM radar”, *Electronics & Communication Engineering Journal*, vol. 2, no. 5, pp. 185 – 194, 1990.

[68] M. Ash, K. Chetty, P. Brennan, J. McElwaine, and C. Keylock, “FMCW radar imaging of avalanche-like snow movements,” in *Radar Conference, 2010 IEEE*, pp. 102 –107, 2010.

[69] M. Musa and S. Salous, “Ambiguity elimination in HF FMCW radar system,” *IEE Proc. Radar and Sonar Navigation*, vol. 147, no. 4, pp. 182–188, 2000.

[70] N. Pohl, T. Jaeschke, and K. Aufinger, “An Ultra-Wideband 80 GHz FMCW Radar System Using a SiGe Bipolar Transceiver Chip Stabilized by a Fractional-N PLL Synthesizer,” *IEEE Trans. Microwave Theory Tech*., vol. 60, no. 3, pp. 757–765, 2012.

[71] A G. Stove, "Linear FMCW Radar Techniques," *IEE Proc F, Radars Signal Process.*, vol. 139 110.5, pp. 343-350, 1992.

[72] F. Kendoul, “Four-dimensional guidance and control of movement using time-to-contact: Application to automated docking and landing of unmanned rotorcraft systems,” *The International Journal of Robotics Research*, pp. 237–267, 2014.

[73] Z. Yang, F. Zhou, and L. Ping, “Bio-inspired collision-free 4D trajectory generation for UAVs using tau strategy,” *Journal of Bionic Engineering 13*, pp. 84–97, 2016.

[74] Z. M. Kassas, A. Arapostathis, and T. E. Humphreys, “Greedy Motion Planning for Simultaneous Signal Landscape Mapping and Receiver Localization,” *IEEE J. Sel. Top. Signal Process.*, vol. 9, no. 2, pp. 247–258, Mar. 2015.

[75] J. Steckel and H. Peremans, "Acoustic Flow-Based Control of a Mobile Platform Using a 3D Sonar Sensor", *IEEE Sensors Journal*, vol. 17, no. 10, pp. 3131-3141, 2017.